DOCTORAL THESIS

Graphitic Carbon Nitride Based Photocatalysts: Design, Synthesis and Properties Investigation

Wei LIU

Materials Chemistry and Engineering Course

Graduated School of Chemical Sciences and Engineering

Hokkaido University

(Doctoral Supervisor : Toshihiro SHIMADA, Professor)

Contents

Chapter 1. General Introduction

1.1 Photocatalysis

Due to the overuse of fossil fuels, the sustainability of the human society is under increasing threats from energy shortage and pollution. With unmatched advantages including environmentally benign and inexhaustibility, solar energy has been viewed as the feasible solution to address the energy dilemma and environmental issues, but its utilization is available only at sunny days. Recently, semiconductor-based photocatalysis, in which the powerful radiation can be utilized as a practicable technology, has attracted numerous attention due to its promising application in the energy and environmental field (i.e., water splitting [1-2], pollutants removal [3-4], CO_2 reduction [5-6], disinfection [7], selective organic synthesis [8-9] and so on).

In 1972, Fujishima and Honda initially carried out photoelectrochemical (PEC) H_2 production from water splitting using TiO_2 photoelectrode [10]. Four years later, Carey et al. explored the photodegradation of organic pollutants using TiO_2 in aqueous solution [11]. Subsequently, considerable development emerged in the synthesis of efficient semiconductor-based photocatalysts, such as TiO_2 [12-13], CdS [14], Bi_2WO_6 [15], $BiVO_4$ [16], Ag_3PO_4 [17], Ta_3N_5 [18], TaON [19]. So far, the search for a high quality semiconductor photocatalyst to alleviating the energy crisis and environmental problems has become a popular research topic.

Generally, photocatalysis occurs in three steps: (i) absorption of photons with energy larger than that of band gap (E_g) to generate electrons and holes, (ii) photoinduced

electron–hole pairs separation and their transportation to the reactive sites on the surface, and (iii) surface oxidation-reduction reaction by the photoinduced holes and electrons [20]. There are several requirements for the semiconductor photocatalyst to achieve a more effective photocatalysis. The photocatalyst should own a suitable band position that matches with the required the redox potential of the reactions and a band gap with entire visible light response. The photocatalyst should be have a fast charge separation and transportation rate and abundant surface active sites to reduce the activation energy [21].

With the merits of cheapness, nontoxicity and chemically inertness, TiO_2 has become the highly explored "golden" photocatalyst. However, its practical application in photocatalysis suffers from its unresponsiveness in the visible solar light because of its large band gap (3.2 eV) [22]. Various strategies, such as doping [23], co-catalyst loading [24], defects control [25] and coupling with other semiconductors [26], have been adopted to improve its photocatalysis under visible light. Other semiconductor photocatalysts shown in Figure 1-1 such as $BiWO_6$ [27], BiOCl [28], BiOBr [28], Ag_2S [29], Ag_3PO_4 [17], AgBr [30] and CdS [14] with suitable bandgaps have also been investigated for photocatalysis. However, the high price, low efficiency, photocorrosion and toxicity limits their wide utilization in photocatalysis. Therefore, development of novel visible-light-active semiconductor materials and construction of effective systems for energy production and environmental pollution remediation is highly advisable.

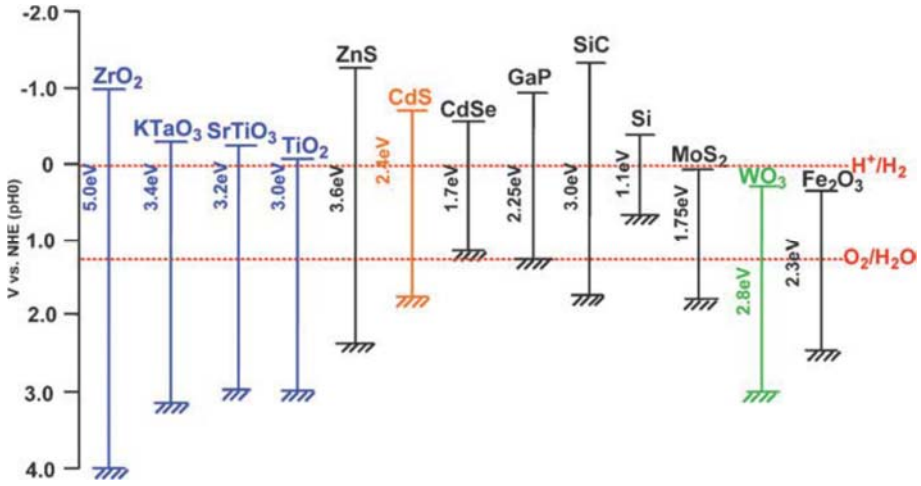

Figure 1-1 Band positions of the common semiconductor photocatalysts. [31]

During the last few years, development of graphitic carbon nitride (g-C_3N_4)-based metal-free photocatalysts have aroused significant attention because of their earth abundance, low price, and environmental benign features. Since Wang et al. initially disclosed the photocatalytic splitting of water over C_3N_4 in 2009, g-C_3N_4-based photocatalysts have been widely used in the photocatalytic CO_2 reduction [32], H_2 evolution [33], degradation of harmful dyes [34], antibiotics [35]. However, its high charge recombination hampers its wide application. It is noteworthy that g-C_3N_4 could be readily used to fabricate heterogenous photocatalysts with tailored composition, morphology, thickness, porosity, optical and electronic properties. Therefore, development of g-C_3N_4-based photocatalysts by appropriate modification have gained much significance. Therefore, several attempts, such as nanostructure modification, elemental doping, copolymerization, formation of heterojunction with other semiconductors, have been made to enhance its photoactivity. In particular, the formation of various nanostructured g-C_3N_4-based photocatalysts, such as 1D tubes, 2D nanoplates and 3D structures, leads to the optimization of chemical stability, optical feature, surface

area and charge diffusion length. Strategies, including elemental doping and copolymerization, result in the narrowed band gap energy so as to utilize the entire solar light [36]. The creation of heterojunction with other semiconductors can speed up the charge separation and transfer to active sites [37].

1.2. General information of g-C_3N_4

There are several allotropes of carbon nitride (C_3N_4), which include α-C_3N_4, β-C_3N_4, graphitic C_3N_4 (g-C_3N_4), cubic and pseudocubic C_3N_4 [20]. Among these phases, g-C_3N_4 is the most stable allotrope at ambient conditions and formed by layers of π-conjugated polymeric structures connected through *s*-triazine or tri-*s*-triazine/heptazine rings. The 2-D layered structure endows g-C_3N_4 unique physical and electronic properties, which favors the photocatalytic performance g-C_3N_4. With respect to TiO_2, g-C_3N_4 possess a proper band gap of 2.7 eV with visible light absorption of around 460 nm. Evidences show that it is thermally stable up to 600 °C in air which is probably associated with the aromatic C-N rings. Additionally, g-C_3N_4 is also chemically stable and resistant to acid and alkali. It can be readily fabricated by thermal pyrolysis of cheap nitrogen-rich precursors such as cyanamide, urea, dicyanamide, thiourea, and melamine. The formation of g-C_3N_4 occurs followed by a range of procedures, e.g., the sublimation and thermal condensation of melamine (297–390 °C), deammonation (545 °C), as revealed by the thermogravimetric-differential scanning calorimetry (TG-DSC) analysis of melamine. Melem transformation into a g-C_3N_4 material is confirmed by temperature-dependent XRD results above 560°C [38]. Similar phenomenon also appears during the creation of

g-C_3N_4 using cyanamide as precursors, apart from the initial melamine formation via condensing the cyanamide (Figure 1-2) [39].

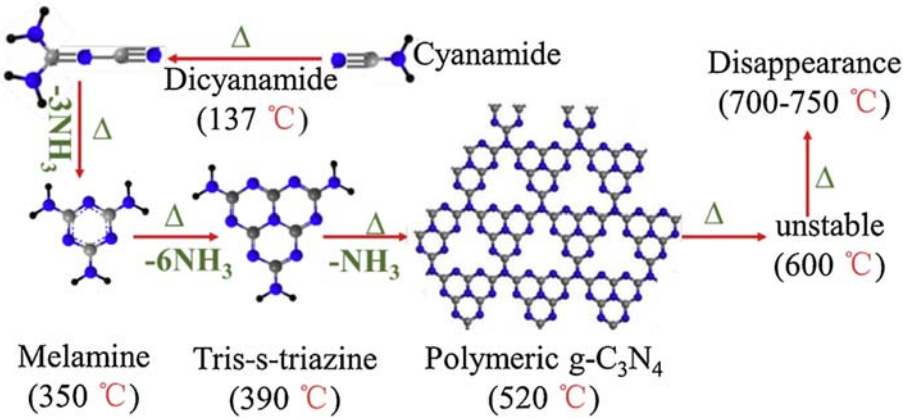

Figure 1-2 Reaction path for the formation of g-C_3N_4 starting from cyanamide [39].

The g-C_3N_4 obtained from thermal treatment of C/N/H-containing species owns low crystallinity because of the existence of defects, which results from the incomplete removal of intermediates. The synthesis of g-C_3N_4 with ideal crystalline exists a kinetic problem. The relatively low crystallinity and plentiful disorder in the g-C_3N_4 lead to its composition indefinable and C/N ratio beyond stoichiometry. Because of the incomplete thermal condensation, there exists hydrogen bonding between melon chains with NH/NH_2 groups. Thus, the photoinduced charge carriers are highly localized within heptazine units, leading to the poor conductivity [20]. Moreover, the existence of defect centers for charge recombination is detrimental to the photoactivity of g-C_3N_4. Hence, the development of g-C_3N_4 with high crystallinity and less defects is desirable for the enhancement of photocatalytic performance in water splitting [40]. Above all, the photocatalytic performance of the pristine g-C_3N_4 remains unfavorable due to its low crystallinity, poor electrical conductivity, high recombination rate, and inefficient visible light absorption.

1.3. Electronic properties of g-C_3N_4

The density-functional-theory (DFT) calculations has been applied to investigate the electronic properties of g-C_3N_4. Results reveal that band gap of melem molecule, polymeric melon and fully condensed g-C_3N_4 were calculated to be 3.5, 2.6 and 2.1 eV, respectively [41]. Obviously, the value of polymeric melon almost approaches the experimentally measured band gap of 2.7 eV. The valence band (VB) and conduction band (CB) of g-C_3N_4 are mainly governed by N 2p orbitals and C 2p orbitals, respectively. Yan et al. calculated the band potentials of the pristine g-C_3N_4 through DFT and the positions of CB and VB were located at −1.12 and + 1.57 eV, respectively [42]. They further measured the VB position of +1.53 eV by valence band X-ray photoelectron spectroscopy (VB-XPS), which is very close to the theoretical calculations. The location of CB minimum (-1.12 eV) in g-C_3N_4 allows the photoinduced electrons to evolve H_2 through water reduction. The VB position (+1.53 eV) also offers a thermodynamical driving force to generate O_2 through water oxidation. It is noteworthy that the surface redox reactions possibly take place only when CB and VB levels are more negative and positive than the reduction and oxidation potentials, respectively. Table 1-1 shows several typical standard redox potentials. Hence, it is rational to modify the electronic band energy of g-C_3N_4 for the enhancement of its redox power to improve its photoactivity.

Table 1-1 Standard redox potentials for some typical species [43,44].

Reaction	E^0(V) vs NHE at pH 0
$2H^+ + 2e^- \rightarrow H_2$ (g)	0
$O_2(g) + e^- \rightarrow O_2^-$ (aq)	−0.33
$O_2(g) + H^+ + e^- \rightarrow HO_2^\bullet$ (aq)	−0.046
$O_2(g) + 2H^+ + 2e^- \rightarrow H_2O_2$ (aq)	0.695
$2H_2O$ (aq) + 4 $h^+ \rightarrow O_2$ (g) + $4H^+$	1.229
$OH^- + h^+ \rightarrow {}^\bullet OH$	2.69
$O_3(g) + 2H^+ + 2e^- \rightarrow O_2$ (g) + H_2O	2.075
$CO_2 + e^- \rightarrow CO_2^-$	−1.9
$2CO_2(g) + 2H^+ + 2e^- \rightarrow$ HOOCCOOH(aq)	−0.481
$CO_2(g) + 2H^+ + 2e^- \rightarrow$ HCOOH(aq)	−0.199
$CO_2(g) + 2H^+ + 2e^- \rightarrow CO(g) + H_2O$	−0.11
$CO_2(g) + 4H^+ + 4e^- \rightarrow C(s) + 2H_2O$	0.206
$CO_2(g) + 4H^+ + 4e^- \rightarrow$ HCHO(aq) + H_2O	−0.07
$CO_2(g) + 6H^+ + 6e^- \rightarrow CH_3OH(aq) + H_2O$	0.03
$CO_2(g) + 8H^+ + 8e^- \rightarrow CH_4$ (g) + $2H_2O$	0.169
$2CO_2(g) + 8H_2O + 12e^- \rightarrow C_2H_4(g) + 12OH^-$	0.07
$2CO_2(g) + 9H_2O + 12e^- \rightarrow C_2H_5OH(aq) + 12OH^-$	0.08
$3CO_2(g) + 13H_2O + 18e^- \rightarrow C_3H_7OH(aq) + 18OH^-$	0.09
$H_2O_2(aq) + H^+ + e^- \rightarrow H_2O + OH^-$	1.14
$HO_2^\bullet + H^+ + e^- \rightarrow H_2O_2(aq)$	1.44
$H_2O_2(aq) + 2H^+ + 2e^- \rightarrow 2H_2O$	1.763

1.4. Design strategies of g-C_3N_4-based photocatalysts

1.4.1. Atomic doping of g-C_3N_4

Generally, doping of exotic elements can enhance the visible light harvesting ability because of the formation of localized or delocalized electronic states. Additionally, the introduction of multiple impurities leads to disorder effects and thus form tail states (Urbach tails) in the electronic structure [45]. In photocatalysis, the band-gap engineering of g-C_3N_4 via the atom-level (metal and non-metal atoms) play an important part in the modification of optical absorption and redox potentials for the enhancement of photocatalytic performance [46].

The metal ions (M^{n+}) can be introduced into the framework of g-C_3N_4 (Figure 1-3a) via an ion coordination route due to the strong interactions between the cations and the negatively charged nitrogen atoms. The incorporation of the transition metal ions, such

as Zn^{2+} [47], Fe^{3+} [48], Co^{3+} [49] and Cu^{2+} [50] into the caves of g-C_3N_4 have been reported by the previous studies to improve the optical absorption, narrow the bandgap, and enhance the carrier mobility, which are beneficial to the photoactivity. Moreover, the coordination of alkali-metal ions such as Li^+, Na^+, and K^+ can enhance charge transfer and separation efficiency to form the spatial charge distribution. Recently, Xiong et al. revealed that K atoms are more likely to be incorporated in the g-C_3N_4 interlayer through bridging the layers (Figure 1-3b), while Na atoms exist in the carbon nitride planes [51]. The K-doped g-C_3N_4 would bring about suppressed charge recombination, increased optical absorption, and enhanced oxidation capability due to the combined effects of positive-shifted valence band position, narrowed band gap and extended π conjugated systems.

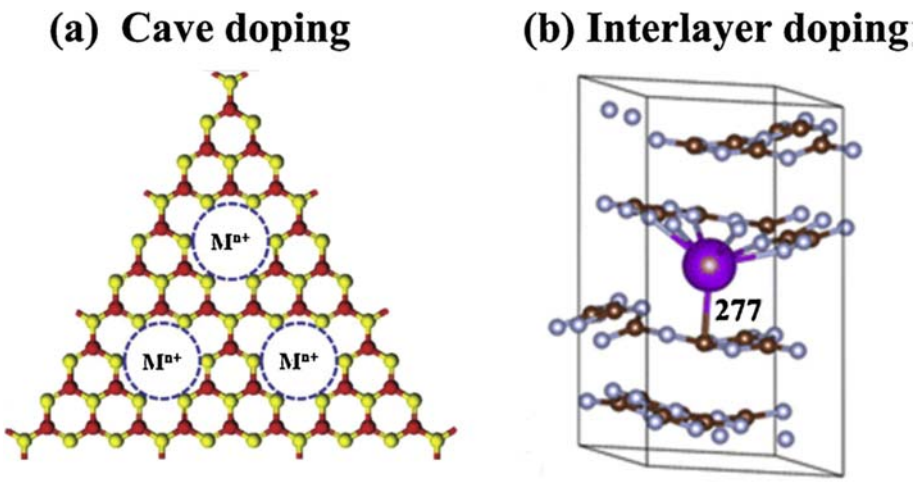

Figure 1-3. Two kinds of metal ion doping of g-C_3N_4 framework: (a) cave doping, the incorporation of metal ions (M^{n+}) through the coordination interactions, Color scheme: C, red; N, yellow [52]; (b) interlayer doping (the interlayer bridging pattern for K) [51].

The non-metals tended to form covalent bond by accepting electrons during the reaction due to its high electro negativity. In most cases, the non-metal doping including

O [53], C [54], B [55], S [56], P [57], and I [58], could lead to the narrowed bandgap and improved optical absorption of g-C_3N_4. Generally, the introduction of I, O and S are preferred to substitute N atoms in the heptazine units, while the C self-doping can replace the bridging N atoms (Figure 1-4). It is noteworthy that introducing these foreign elements can optimize the π-electron delocalization, which is beneficial for enhancing the charge mobility and separation, thus improving the photoactivity significantly. P and B atoms are more favorable to take the place of C atoms, thus leading to the formation of P/B-N bond in g-C_3N_4. Specially, the interstitial incorporation of P into the framework of g-C_3N_4 also appears using $(NH_4)_2HPO_4$ as phosphorus precursor [59]. In situ sulfur and boron doping of g-C_3N_4 also occurred on the C and N atoms in the heptazine units, respectively [60-61]. Additionally, the F doping can lead to forming C-F bonding in g-C_3N_4 when NH_4F served as the fluorine source [62]. However, it is noted that moderately doping of exotic atoms is advocated in photocatalysis, because excessive doping can create more defects centers for the charge recombination.

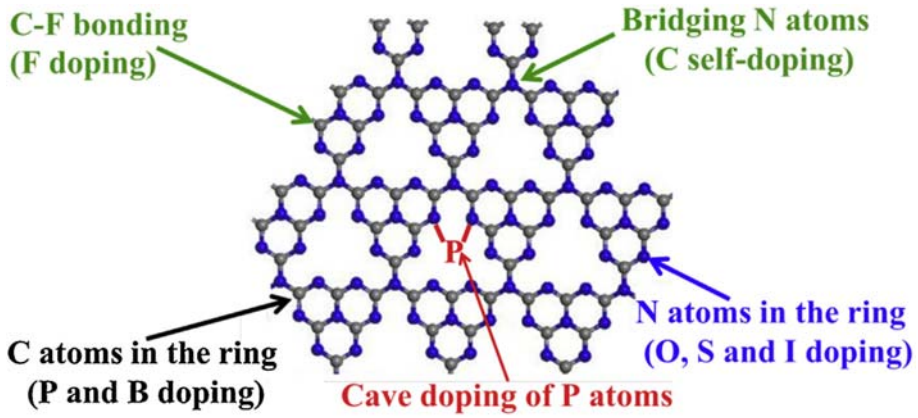

Figure 1-4 Possible substituted sites of non-metal doping in the single layer of g-C_3N_4 [63].

1.4.2. Dimensional control

With respect to the bulk counterparts, nanostructured 2D g-C_3N_4 nanosheets displayed several merits in photocatalysis, such as the high surface area, short charge migration distance, plentiful active sites, and improved redox abilities of photoinduced charge carriers [64]. Thus, controlling the physical dimensions of g-C_3N_4 can serve as a promising candidate to adjust the intriguing surface, optical, electronic features, leading to the enhanced catalytic activity. Generally, the ultrathin g-C_3N_4 nanosheets could be prepared through the top-down delamination of layered bulk g-C_3N_4 and bottom-up strategies [65-66]. The two preparation strategies can be further grouped into ultrasonic exfoliation, thermal oxidation exfoliation, chemical exfoliation and combined routines.

It is known that the enthalpy of mixing will decrease in a liquid with surface energy well-matched to that of g-C_3N_4 (115 mJ m^{-2}), giving rise to the efficient exfoliation of bulk g-C_3N_4 into 2D nanosheets [67]. Thus, the ultrasonic exfoliation of the layered g-C_3N_4 into 2D ultrathin nanosheets have been achieved through ultrasonic treatment in solvents with suitable surface energies, such as NMP, IPA, DMF, methanol, ethanol, acetonitrile and water (102 mJ m^{-2}) and their mixtures [67-69]. However, this approach involved the use of organic solvents, long treatment time with low production, limit their wide application. Fortunately, it was revealed that the amphoteric monolayer g-C_3N_4 nanosheets with ion charged groups can be obtained through chemical exfoliation in acid or alkaline solution with significantly reduced ultrasonication time [70]. Through the thermal oxidation etching approach, the bulk g-C_3N_4 could be peeled off and g-C_3N_4 with 2 nm-thickness can be obtained [71]. However, its drawbacks including low yield (<6%) and plentiful interface defects hampers its further application. Thus, the scalable synthesis

of high-quality g-C_3N_4 nanosheets had been achieved by the dicyandiamide-blowing method using NH_4Cl as the assistance [72]. It is noteworthy that the cost-effective and scalable fabrication of 2D g-C_3N_4 nanosheets can be achieved through the proper combination of liquid, chemical exfoliation and thermal oxidation etching exfoliation.

1.4.3. Heterojunction construction

The construction of semiconductor heterojunctions could result in the band bending and the generation of internal electrical field, which could remarkably speed up the efficient spatial charge separation thus in favor of the photoactivity [1]. Generally, the semiconductor heterojunctions can be separated into Schottky junction, Type I, II and Type III heterojunctions (Figure 1-5). Among these types, only Schottky junction and Type II heterojunctions can remarkably enhance the charge separation, leading to their suppressed recombination and extended lifetime. Up to now, the combination of g-C_3N_4 with several semiconductors, such as TiO_2 [73], CdS [74], Cu_2O [75], WO_3 [76], $BiVO_4$ [77], BiOX [78], Bi_2WO_6 [79], Fe_2O_3 [80], have been achieved for creation for the Type II heterojunctions and fast charge separation.

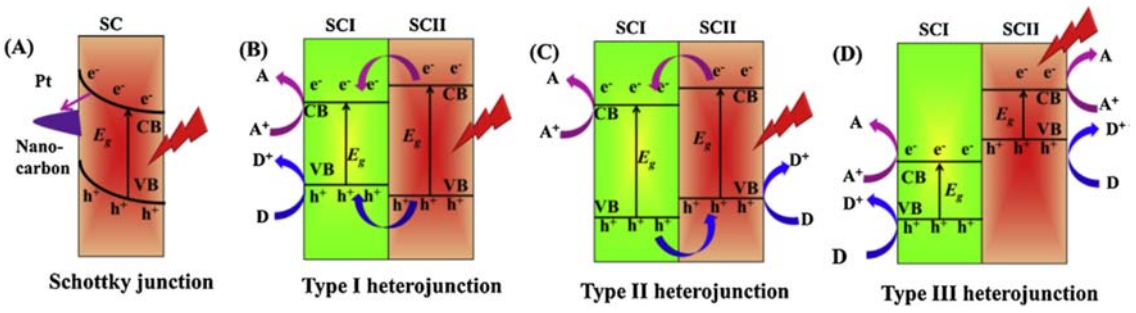

Figure 1-5 Spatial charge-separation mechanisms for four different types of semiconductor heterojunctions: (A) Schottky junction, (B) Type I, (C) Type II, and (D) Type III heterojunctions [63].

In general, for the Type II heterojunction photocatalytic systems, the photoredox reactions largely take place on the surface of semiconductor with lower CB and VB potentials, leading to the smaller driving forces during the photoreaction. In contrast, for the Z-scheme system (Figure 1-6), its photocatalytic performance mainly relies on the surface features of semiconductor with higher CB and VB potentials, thus giving rise to the robust redox ability and improved photoactivity [81]. Inspired by the natural photosynthesis process, the artificial Z-scheme heterojunctions have been created by the combination of two semiconductors in the presence of mediators. In the Z-scheme, the separated responsibility of each semiconductor for one (oxidation or reduction) reaction results in greatly expanded optical absorption, enhanced driving forces, charge separation rate and photoactivity [82]. It seems that the g-C_3N_4-based Z-scheme systems could own many merits and great potential in practical photocatalysis application.

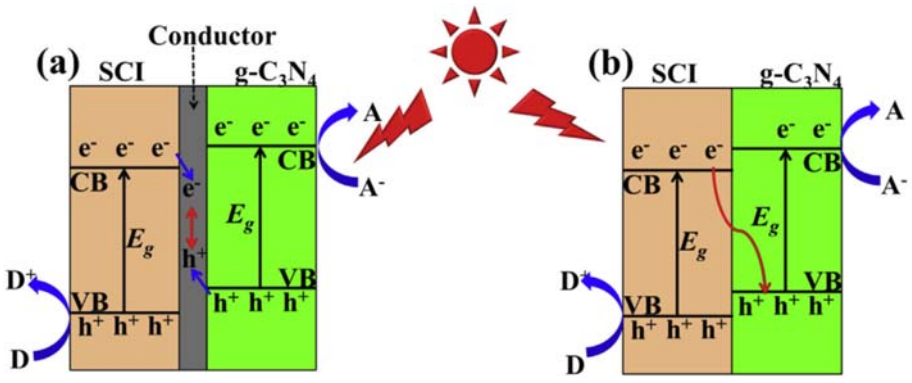

Figure 1-6 Schematic illustration of spatial charge separation in the all-solid-state g-C_3N_4-based Z-scheme photocatalytic systems with (a) and without (b) mediators [63].

1.4.4. Nanocarbon loading

The g-C_3N_4/carbon heterostructures have been synthesized by coupling g-C_3N_4 with several carbonaceous materials such as C_{60} [83], CNTs [84], carbon quantum dots [85], graphene [86] and so on. Due to their excellent electrical conductivity, these carbon

materials can serve as reduction cocatalysts to receive electrons from g-C_3N_4 to retard the charge recombination. Besides, several novel features are presented by the construction of the hybrid materials including increased active sites, electron capacity and improved optical absorption [87].

Among the carbon materials, graphene, a sp^2-hybridized 2D nanosheet, demonstrates exceptional mechanical, electrical and thermal features, such as high optical transmittance, specific surface area, conductivity, and electron mobility [88]. Thus, developing the g-C_3N_4/graphene nanocomposites has been considered as promising approach to speed up the charge migration and retard the charge recombination, thereby giving rise to an improved photocatalytic activity. The 2D/2D interaction in the g-C_3N_4/graphene hybrids is beneficial to increasing the interfacial coupling areas and promoting the charge separation. For instance, cross-linked reduced graphene oxide (rGO)/g-C_3N_4 nanocomposites with tunable band structures could be prepared due to the formation of C-O-C covalent bonding, which demonstrated reduced bandgap with increasing rGO ratio, thus beneficial for the visible-light photoactivity [89].

1.5 Thesis motivations and organization

In this thesis, in order to increase the active sites and to improve charge separation and migration rate in g-C_3N_4, a combined fast thermal etching and gas-driven exfoliation strategy was developed to modify g-C_3N_4. Such treatment endows the of g-C_3N_4 with novel features, such as 2D porous architecture, increased active sites and fast charge mobility. Such few-layered porous g-C_3N_4 photocatalysts demonstrated remarkably

enhanced photocatalytic water splitting and degradation efficiency of RhB under visible-light-driven illumination.

Subsequently, aiming at the preparation of g-C_3N_4 nanoplates in a sustainable and cost-effective approach, a solid-state mechanical milling with sugars method was proposed to fabricate the few-layered g-C_3N_4 nanoplates. As a result, the water-soluble g-C_3N_4 nanoplates demonstrated enlarged surface area and promoted charge separation, thus leading to enhanced visible-light-driven photocatalytic performance regarding the hydrogen production and RhB degradation.

Later on, a defect engineering strategy was adopted to tailor the structural, morphological, optical and electronic properties of the g-C_3N_4. The introduction of nitrogen defects is achieved through the delamination followed by quick thermal etching of the pristine g-C_3N_4. As a result, it was revealed that nitrogen-defective g-C_3N_4 demonstrated enhanced optical absorption, number of active sites and the charge separation and transfer efficiency, thus giving rise to the improvement of the photoreaction. This work provides a practical way to improve photocatalytic efficiency of g-C_3N_4 which shows promising application.

References:

1. X. Li, J. Yu, J. Low, Y. Fang, J. Xiao and X. Chen, *J. Mater. Chem. A*, 2015, **3**, 2485-2534.
2. X. Chen, S. Shen, L. Guo and S. S. Mao, *Chem. Rev.*, 2010, **110**, 6503-6570.
3. C.-C. Wang, J.-R. Li, X.-L. Lv, Y.-Q. Zhang and G. Guo, *Energy Environ. Sci.*, 2014, **7**, 2831-2867.
4. M. N. Chong, B. Jin, C. W. Chow and C. Saint, *Water Res.*, 2010, **44**, 2997-3027.
5. X. Li, J. Wen, J. Low, Y. Fang and J. Yu, *Sci. China Mater.*, 2014, **57**, 70-100.
6. J. Low, J. Yu and W. Ho, *J. Phys. Chem. Lett.*, 2015, **6**, 4244-4251.
7. S. Malato, P. Fernández-Ibáñez, M. I. Maldonado, J. Blanco and W. Gernjak, *Catal. Today*, 2009, **147**, 1-59.
8. H. Kisch, *Angew. Chem. Int. Ed.*, 2013, **52**, 812-847.
9. X. Lang, X. Chen and J. Zhao, *Chem. Soc. Rev.*, 2014, **43**, 473-486.
10. A. Fujishima and K. Honda, *nature*, 1972, **238**, 37-38.
11. J. H. Carey, J. Lawrence and H. M. Tosine, *Bull. Environ. Contam. Toxicol.*, 1976, **16**, 697-701.
12. J. Yu, J. Low, W. Xiao, P. Zhou and M. Jaroniec, *J. Am. Chem. Soc.*, 2014, **136**, 8839-8842.
13. J. Fei and J. Li, *Adv. Mater.*, 2015, **27**, 314-319.
14. J. Yu, J. Jin, B. Cheng and M. Jaroniec, *J. Mater. Chem. A*, 2014, **2**, 3407-3416.
15. C. Li, G. Chen, J. Sun, J. Rao, Z. Han, Y. Hu and Y. Zhou, *ACS Appl. Mater. Interfaces*, 2015, **7**, 25716-25724.

16. H. Li, H. Yu, X. Quan, S. Chen and H. Zhao, *Adv. Funct. Mater.*, 2015, **25**, 3074-3080.

17. Q. Xiang, D. Lang, T. Shen and F. Liu, *Appl. Catal. B: Environ*, 2015, **162**, 196-203.

18. S. Chen, S. Shen, G. Liu, Y. Qi, F. Zhang and C. Li, *Angew. Chem. Int. Ed.*, 2015, **54**, 3047-3051.

19. S. Chen, Y. Qi, T. Hisatomi, Q. Ding, T. Asai, Z. Li, S. S. K. Ma, F. Zhang, K. Domen and C. Li, *Angew. Chem. Int. Ed.*, 2015, **54**, 8498-8501.

20. A. Naseri, M. Samadi, A. Pourjavadi, A. Z. Moshfegh and S. Ramakrishna, *J. Mater. Chem. A*, 2017, **5**, 23406-23433.

21. C. Li, Y. Xu, W. Tu, G. Chen and R. Xu, *Green Chem.*, 2017, **19**, 882-899.

22. H. Dong, G. Zeng, L. Tang, C. Fan, C. Zhang, X. He and Y. He, *Water Res.*, 2015, **79**, 128-146.

23. S. A. Ansari, M. M. Khan, M. O. Ansari and M. H. Cho, *New J. Chem.*, 2016, **40**, 3000-3009.

24. Q. Wang, G. Yun, Y. Bai, N. An, Y. Chen, R. Wang, Z. Lei and W. Shangguan, *Int. J. Hydrogen Energy*, 2014, **39**, 13421-13428.

25. X. Chen, L. Liu, Y. Y. Peter and S. S. Mao, *Science*, 2011, **331**, 746-750.

26. L. Ding, H. Zhou, S. Lou, J. Ding, D. Zhang, H. Zhu and T. Fan, *Int. J. Hydrogen Energy*, 2013, **38**, 8244-8253.

27. H. Cheng, B. Huang, Y. Liu, Z. Wang, X. Qin, X. Zhang and Y. Dai, *Chem. Commun.*, 2012, **48**, 9729-9731.

28. G.-J. Lee, Y.-C. Zheng and J. J. Wu, *Catal. Today*, 2018, **307**, 197-204.

29. X. Yu, J. Liu, A. Genç, M. Ibáñez, Z. Luo, A. Shavel, J. Arbiol, G. Zhang, Y. Zhang and A. Cabot, *Langmuir*, 2015, **31**, 10555-10561.

30. N. Shehzad, M. Tahir, K. Johari, T. Murugesan and M. Hussain, *Appl. Surf. Sci.*, 2019, **463**, 445-455.

31. A. Kudo and Y. Miseki, *Chem. Soc. Rev.*, 2009, **38**, 253-278.

32. W.-J. Ong, L. K. Putri, Y.-C. Tan, L.-L. Tan, N. Li, Y. H. Ng, X. Wen and S.-P. Chai, *Nano Res.*, 2017, **10**, 1673-1696.

33. Y. Zhu, D. Zhang, L. Gong, L. Zhang and Z. Xia, *Front. Mater.*, 2019, **6**, 16.

34. A. Mishra, A. Mehta, S. Kainth and S. Basu, *J. Mater. Sci.*, 2018, **53**, 13126-13142.

35. C. Zhou, C. Lai, P. Xu, G. Zeng, D. Huang, Z. Li, C. Zhang, M. Cheng, L. Hu and J. Wan, *ACS Sustainable Chem. Eng.*, 2018, **6**, 6941-6949.

36. C. Hu, W.-Z. Hung, M.-S. Wang and P.-J. Lu, *Carbon*, 2018, **127**, 374-383.

37. Z. Kong, X. Chen, W.-J. Ong, X. Zhao and N. Li, *Appl. Surf. Sci.*, 2019, **463**, 1148-1153.

38. B. Jürgens, E. Irran, J. Senker, P. Kroll, H. Müller and W. Schnick, *J. Am. Chem. Soc.*, 2003, **125**, 10288-10300.

39. A. Thomas, A. Fischer, F. Goettmann, M. Antonietti, J.-O. Müller, R. Schlögl and J. M. Carlsson, *J. Mater. Chem.*, 2008, **18**, 4893-4908.

40. L. Lin, H. Ou, Y. Zhang and X. Wang, *ACS Catal.*, 2016, **6**, 3921-3931.

41. I. F. Teixeira, E. C. Barbosa, S. C. E. Tsang and P. H. Camargo, *Chem. Soc. Rev.*, 2018, **47**, 7783-7817.

42. S. Yan, S. Lv, Z. Li and Z. Zou, *Dalton Trans.*, 2010, **39**, 1488-1491.

43. X. Li, J. Yu and M. Jaroniec, *Chem. Soc. Rev.*, 2016, **45**, 2603-2636.

44. A. Bard, *Stand. Potentials Aqueous Solution*, Routledge, 2017.

45. H. Yaghoubi, Z. Li, Y. Chen, H. T. Ngo, V. R. Bhethanabotla, B. Joseph, S. Ma, R. Schlaf and A. Takshi, *ACS Catal.*, 2015, **5**, 327-335.

46. Y. Zheng, L. Lin, B. Wang and X. Wang, *Angew. Chem. Int. Ed.*, 2015, **54**, 12868-12884.

47. B. Yue, Q. Li, H. Iwai, T. Kako and J. Ye, *Sci. Technol. Adv. Mater.*, 2011, **12**, 034401.

48. S. Hu, X. Chen, Q. Li, F. Li, Z. Fan, H. Wang, Y. Wang, B. Zheng and G. Wu, *Appl. Catal. B: Environ.*, 2017, **201**, 58-69.

49. P.-W. Chen, K. Li, Y.-X. Yu and W.-D. Zhang, *Appl. Surf. Sci.*, 2017, **392**, 608-615.

50. S. Le, T. Jiang, Q. Zhao, X. Liu, Y. Li, B. Fang and M. Gong, *RSC Adv.*, 2016, **6**, 38811-38819.

51. T. Xiong, W. Cen, Y. Zhang and F. Dong, *ACS Catal.*, 2016, **6**, 2462-2472.

52. S. Cao, J. Low, J. Yu and M. Jaroniec, *Adv. Mater.*, 2015, **27**, 2150-2176.

53. J. Li, B. Shen, Z. Hong, B. Lin, B. Gao and Y. Chen, *Chem. Commun.*, 2012, **48**, 12017-12019.

54. G. Dong, K. Zhao and L. Zhang, *Chem. Commun.*, 2012, **48**, 6178-6180.

55. Y. Wang, H. Li, J. Yao, X. Wang and M. Antonietti, *Chem. Sci.*, 2011, **2**, 446-450.

56. L. Ge, C. Han, X. Xiao, L. Guo and Y. Li, *Mater. Res. Bull.*, 2013, **48**, 3919-3925.

57. S. Guo, Z. Deng, M. Li, B. Jiang, C. Tian, Q. Pan and H. Fu, *Angew. Chem. Int. Ed.*, 2016, **55**, 1830-1834.

58. G. Zhang, M. Zhang, X. Ye, X. Qiu, S. Lin and X. Wang, *Adv. Mater.*, 2014, **26**, 805-

809.

59. J. Ran, T. Y. Ma, G. Gao, X.-W. Du and S. Z. Qiao, *Energy Environ. Sci.* 2015, **8**, 3708-3717.

60. J. Hong, X. Xia, Y. Wang and R. Xu, *J. Mater. Chem.*, 2012, **22**, 15006-15012.

61. S. Yan, Z. Li and Z. Zou, *Langmuir*, 2010, **26**, 3894-3901.

62. Y. Wang, Y. Di, M. Antonietti, H. Li, X. Chen and X. Wang, *Chem. Mater.*, 2010, **22**, 5119-5121.

63. J. Wen, J. Xie, X. Chen and X. Li, *Appl. Surf. Sci.*, 2017, **391**, 72-123.

64. S. Yang, Y. Gong, J. Zhang, L. Zhan, L. Ma, Z. Fang, R. Vajtai, X. Wang and P. M. Ajayan, *Adv. Mater.*, 2013, **25**, 2452-2456.

65. J. Zhang, Y. Chen and X. Wang, *Energy Environ. Sci.*, 2015, **8**, 3092-3108.

66. X. Dong and F. Cheng, *J. Mater. Chem. A*, 2015, **3**, 23642-23652.

67. X. She, H. Xu, Y. Xu, J. Yan, J. Xia, L. Xu, Y. Song, Y. Jiang, Q. Zhang and H. Li, *J. Mater. Chem. A*, 2014, **2**, 2563-2570.

68. X. Zhang, X. Xie, H. Wang, J. Zhang, B. Pan and Y. Xie, *J. Am. Chem. Soc.*, 2013, **135**, 18-21.

69. K. Schwinghammer, M. B. Mesch, V. Duppel, C. Ziegler, J. R. Senker and B. V. Lotsch, *J. Am. Chem. Soc.*, 2014, **136**, 1730-1733.

70. T. Y. Ma, Y. Tang, S. Dai and S. Z. Qiao, *Small*, 2014, **10**, 2382-2389.

71. P. Niu, L. Zhang, G. Liu and H. M. Cheng, *Adv. Funct. Mater.*, 2012, **22**, 4763-4770.

72. X. Lu, K. Xu, P. Chen, K. Jia, S. Liu and C. Wu, *J. Mater. Chem. A*, 2014, **2**, 18924-18928.

73. J. Yu, S. Wang, J. Low and W. Xiao, *Phys. Chem. Chem. Phys.*, 2013, **15**, 16883-16890.

74. Y. Xu and W. D. Zhang, *Eur. J. Inorg. Chem.*, 2015, **2015**, 1744-1751.

75. L. Liu, Y. Qi, J. Hu, W. An, S. Lin, Y. Liang and W. Cui, *Mater. Lett.*, 2015, **158**, 278-281.

76. J. Zhao, Z. Ji, X. Shen, H. Zhou and L. Ma, *Ceram. Int.*, 2015, **41**, 5600-5606.

77. G. Miao, D. Huang, X. Ren, X. Li, Z. Li and J. Xiao, *Appl. Catal. B: Environ.*, 2016, **192**, 72-79.

78. S. Yin, J. Di, M. Li, Y. Sun, J. Xia, H. Xu, W. Fan and H. Li, *J. Mater. Sci.*, 2016, **51**, 4769-4777.

79. S. G. Kumar and K. K. Rao, *Appl. Surf. Sci.*, 2015, **355**, 939-958.

80. K. C. Christoforidis, T. Montini, E. Bontempi, S. Zafeiratos, J. J. D. Jaén and P. Fornasiero, *Appl. Cata. B: Environ.*, 2016, **187**, 171-180.

81. P. Zhou, J. Yu and M. Jaroniec, *Adv. Mater.*, 2014, **26**, 4920-4935.

82. K. Maeda, *ACS Catal.*, 2013, **3**, 1486-1503.

83. X. Bai, L. Wang, Y. Wang, W. Yao and Y. Zhu, *Appl. Catal. B: Environ.*, 2014, **152**, 262-270.

84. R. C. Pawar, S. Kang, S. H. Ahn and C. S. Lee, *RSC Adv.*, 2015, **5**, 24281-24292.

85. Q. Liu, T. Chen, Y. Guo, Z. Zhang and X. Fang, *Appl. Cata. B: Environ.*, 2016, **193**, 248-258.

86. L. Xu, W.-Q. Huang, L.-L. Wang, Z.-A. Tian, W. Hu, Y. Ma, X. Wang, A. Pan and G.-F. Huang, *Chem. Mater.*, 2015, **27**, 1612-1621.

87. Y. Guo, P. Yao, D. Zhu and C. Gu, *J. Mater. Chem. A*, 2015, **3**, 13189-13192.

88. S. Park and R. S. Ruoff, *Nat. Nanotechnol.*, 2009, **4**, 217.

89. S. Hu, L. Yang, Y. Tian, X. Wei, J. Ding, J. Zhong and P. K. Chu, *J. Colloid Interface Sci.*, 2014, **431**, 42-49.

Chapter 2. Porous Graphitic Carbon Nitride Nanoplates Obtained by A Combined Exfoliation Strategy for Enhanced Visible Light Photocatalytic Activity

2.1 Introduction

The increasing global environment pollution and energy crisis have received much concerns and numerous attempts are made to exploit the high-efficiency photocatalysts which can achieve the solar energy conversion by a photoactivity [1-3]. Since Wang et al. firstly exploited the g-C_3N_4 for photocatalytic H_2 evolution [4], much attention has been paid to g-C_3N_4 which demonstrates high physicochemical stability, non-metal constituent and proper optical absorption [5-7]. However, the g-C_3N_4 showed unsatisfactory photoactivity caused by its limited surface area and rapid charge recombination [8-10]. Up to now, several tactics have been employed to improve its photoactivity, such as the nanostructure design, heterojunctions construction, heteroatoms doping, defects engineering, as well as the co-catalysts loading [11-15].

Recently, the 2D g-C_3N_4 nanoplates, a king of nanostructured materials, have become more promising in photocatalysis because of their high surface area, plentiful active sites and rapid electron mobility [16,17]. As a consequence, there have been developed various approaches for the preparation of few-layered nanoplates, including the chemical exfoliation, mechanical exfoliation and thermal etching exfoliation [17-21]. Particularly, thermal etching method have become popular in photocatalysis due to the merits of easy

operation, environmental benign and cost-effectiveness. Very recently, it was reported that a well-developed porous structure could be achieved by a quick thermal treatment [22]. It was noteworthy that g-C_3N_4 nanoplates with porous structures are more preferred for photoactivity because their increased active sites and diffusion channels are favorable for the optical absorption and the charge transfer [23,24]. Therefore, the proposal of the fabrication of porous carbon nitride nanoplates is highly desired.

Here, the synthesis of porous g-C_3N_4 nanoplates was achieved through a facile two-step process. As illustrated in Figure 2-1, the pristine g-C_3N_4 was warmed up to 750°C rapidly in air. Afterwards, the high-temperature sample is instantly added into the liquid nitrogen (l-N_2). Thanks to the thermal treatment and the following gasification of l-N_2, the pristine g-C_3N_4 is subjected to exfoliation. Moreover, porous g-C_3N_4 nanoplates are obtainable during the repeating exfoliation cycles. With respect to the pristine g-C_3N_4, the as-synthesized porous g-C_3N_4 nanoplates demonstrated 9 times higher hydrogen evolution and 6 folds greater RhB degradation rate under visible-light illumination, respectively. This work opens a new horizon to develop innovative nanostructured g-C_3N_4-based catalysts for efficient photoactivity.

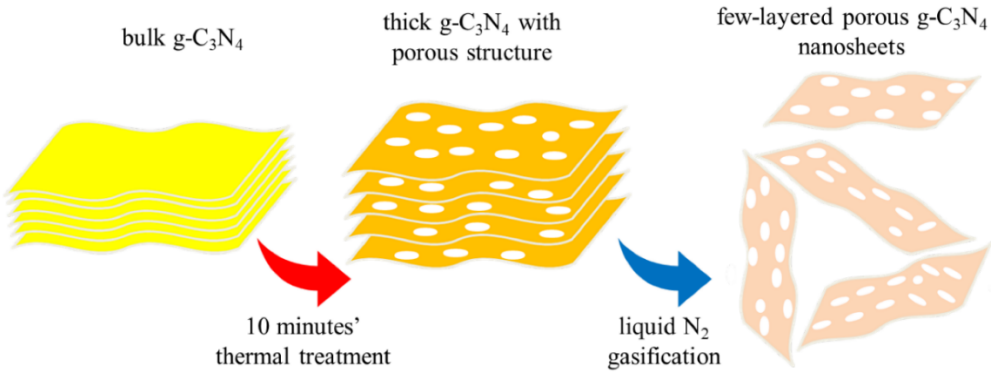

Figure 2-1 An illustration of the process for the fabrication of fl-P-CN.

2.2 Experimental section

2.2.1 Material preparation

The pristine g-C_3N_4 was obtained by heating dicyandiamide to 550 ^oC for 4 h with a ramp rate of 2.3 ^oC min^{-1}. After cooled naturally and ground into powder, the sample was denoted as CN.

To prepare the few-layered porous carbon nitride (fl-P-CN), the pristine CN in a crucible with a lid was put in a muffle furnace which was preheated at 750 ^oC and held at the high temperature for 10 minutes. Then the CN was transferred into a beaker containing 200ml of l-N_2 until the l-N_2 vaporized totally. The above steps were subjected to repeat for 10 times and the final products were obtained with yield around 10%.

2.2.2 Catalyst Characterization

The X-ray diffraction (XRD) patterns were performed on Rigaku Miniflex 600. Raman spectra were carried out on a Horiba Lab RAM HR800 Raman spectrometer. Fourier transform infrared (FTIR) analysis were conducted on JASCO FT/IR-4600. Elemental analysis (EA) results were determined by Elementar vario MACRO cube Elemental Analyzer. Surface chemical analysis was performed on JEOL JPS-9200 X-ray photoelectron spectroscopy (XPS). The morphology results were obtained on a JEOL JSV-6510LA scanning electron microscopy (SEM) and FEI Titan3_G2_60-300 transmission electron microscopy (TEM). A JASCO FP-8000 spectrofluorometer was employed to obtain the photoluminescence (PL) spectra. A Varian Cary 5000 UV-visible spectrophotometer was exploited to record the diffuse reflectance spectra (DRS). N_2 adsorption-desorption tests were performed at 77 K to determine the Brunauer-Emmett-

Teller (BET) surface area (Autosorb-iQ2, Quantachrome). The electron spin resonance (ESR) results were recorded on an JEOL JES-TE 200 ESR spectrometer. A 1260/1287 Solartron Analytical electrochemical workstation was used to measure the electrochemical impedance spectroscopy (EIS). The transient photocurrent results of the samples loaded on an ITO sheet were analyzed on a three-electrode cell with an aqueous electrolyte of a 0.5 M Na_2SO_4 solution vs Ag/AgCl.

2.2.3 Photocatalytic Hydrogen Generation Test

The H_2 generation test was conducted in a sealed glass reactor containing 28 ml of triethanolamine (TEOA) aqueous solution (10 vol%). 30 mg of photocatalyst was exploited for the photoactivity test. 3 wt% Pt was served as the co-catalyst via a *in situ* photo-deposition process. Before the reaction, the N_2 was used to purge the system for 30 minutes. A 150 W xenon lamp with a 400 nm cut-off filter was chosen as the light source. A gas chromatography within a thermal conductivity detector was employed to measure the produced H_2.

2.2.4 Photocatalytic RhB Degradation Test

Photodegradation of RhB was performed in a glass bottle containing 50 mL of RhB aqueous solution (10 mg/L). 25 mg of catalyst was employed for the photocatalysis. To achieve an adsorption-desorption equilibrium, the suspension was stirred for 30 min in the dark. During the reaction, 3 mL of the solution was taken out at every 20 minutes, and then centrifuged. Afterwards, the supernatant was analyzed by a UV-3600 Shimadzu spectroscope at the absorption of 553 nm, which reflected the concentration of RhB.

The addition of isopropanol (IPA), Benzoquinone (BQ), triethanolamine (TEOA) into the RhB solution as the scavengers for hydroxyl radicals (•OH), superoxide radicals ($•O_2^-$), and superoxide holes (h+) was conducted to detect the reactive species in the photoreaction, respectively.

2.3. Results and discussion

2.3.1 Structural characterization

Figure 2-2a illustrated the XRD patterns of the samples. The diffraction peaks of fl-P-CN displayed similar positions to CN, indicating its unchanged structure. The diffraction peaks of fl-P-CN at 27.4° (002) and 13.0° (100) were assigned to the interlayer structural stacking and in-plane packing motif respectively [4,8]. But the (002) peak of fl-P-CN displayed an apparent shift from 27.4° to 27.9°, indicating its interlayer distance reduction from 0.326 nm to 0.320 nm. The decreased interlayer length indicates the exfoliation treatment endows the fl-P-CN a denser stacking structure. Additionally, the much weakened (002) peak intensity of fl-P-CN implying that its layered structure has been delaminated [25]. Figure 2-2b revealed that FTIR spectra of the samples owned several absorption bands, namely, the band at 2900-3500 cm^{-1} for the vibrational absorptions of N-H bonds, the band in the 1200-1700 cm^{-1} range for the aromatic C-N heterocyclic units and the peak at 809 cm^{-1} for heptazine rings [8,26]. With respect to CN, the typical peaks of fl-P-CN appeared more evident, probably due to the elimination of the disordered or amorphous constituents of the sample [27]. Figure 2-2c exhibited the Raman spectra of the samples. As for CN, the two distinct peaks at 970 and 700 cm^{-1} are attributed to the

breathing modes of heptazine rings. The major band in the 1200−1700 cm^{-1} region is ascribed to the C–N stretching vibrations [28,29]. These properties appeared for both samples but more obvious for fl-P-CN. The better-defined fl-P-CN suggested an improved in-plane π-conjugated structure in favor of the photoactivity.

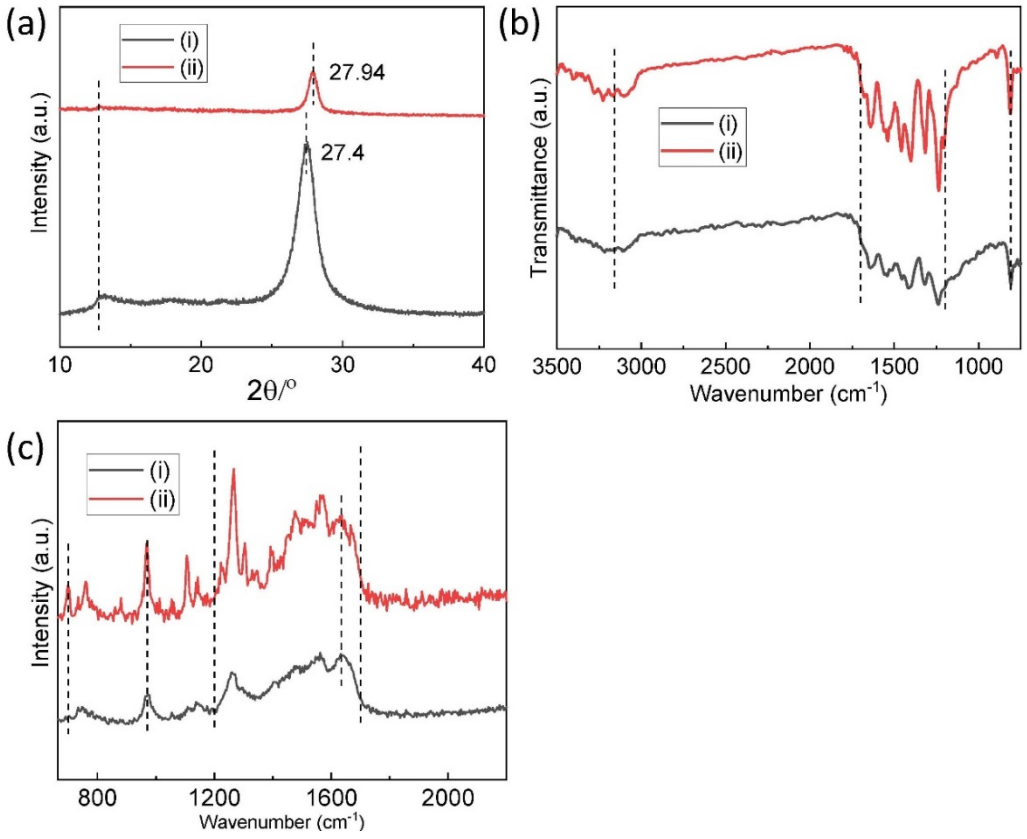

Figure 2-2 The spectra of (a) XRD (b) FT-IR and (c) Raman for the as-prepared (i) CN and (ii) fl-P-CN.

XPS results of the samples are presented in Figure 2-3, which exhibited no apparent chemical shift of C and N elements between the two samples, suggesting their similar bonding states. Figure 2-3a exhibited that there are three main peaks at 285.0, 286.5 and 288.4eV after separating the C 1s spectra of CN, ascribing to the C=C, sp^3 C and N=C-N respectively [8,16,30]. With respect to CN, the peak area ratio of C=C for fl-P-CN

exhibited reduction, revealing the removal of graphitic carbon species. The N 1s spectra (Figure 2-3b) of CN can be divided into four main peaks at 398.6 eV, 399.4 eV, 401.0 eV and 404.6 eV, corresponding to the N=C-N, the tertiary N–$(C)_3$, N–H and π-excitations, respectively [8,16,31]. The weight ratio of N=C–N and N–$(C)_3$ between the two samples exhibited small difference, revealing their similar N bonding states. On the basis of the XPS results, the high temperature rendered the carbon atoms in the CN looser and a portion even oxidized to shape the porous structure. Moreover, more exposed carbon atoms in the CN were formed during the following l-N_2 gasification which produced great gasification energy. As a consequence, during the repeating exfoliation cycles, the novel porous morphology could be created.

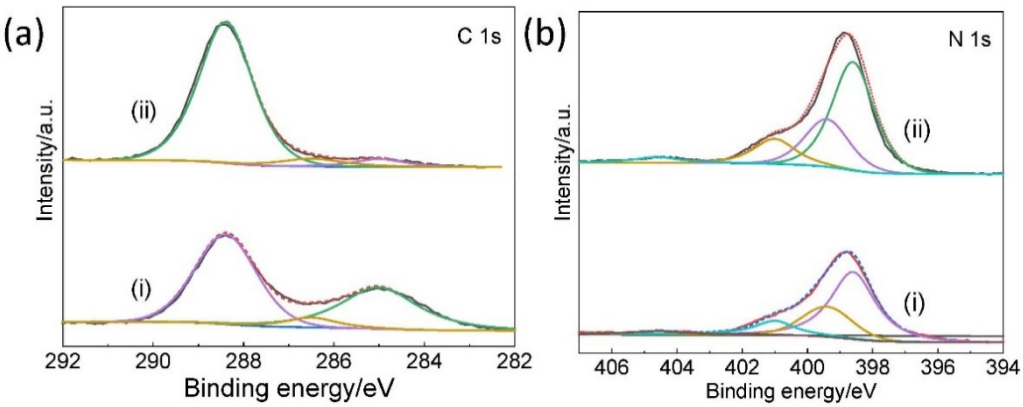

Figure 2-3 High-resolution XPS spectra of the as-fabricated (i) CN and (ii)fl-P-CN: (a) C1s and (b) N1s

The microstructures of the samples were explored by SEM and TEM analysis. Figure 2-4a exhibited that fl-P-CN owned the 2D porous structure with plentiful mesopores in contrast to the stacked lamellar structure of the pristine CN. The pore-size were in ~10–100 nm range revealed by the high-resolution SEM (Figure 2-4b). The TEM images also exhibited that the sheet-like fl-P-CN nanoplates with in-plane pores (Figure 2-4c,d). The

selected-area electron diffraction (SAED) pattern of the fl-P-CN nanoplates exhibited two obvious diffraction rings (inset of Figure 2-4d), corresponding to the (100) and (002) planes [32], further revealing the undestroyed structure. Moreover, the high- resolution TEM picture (Figure 2-5) exhibited nanoholes and disordered lattice edges, indicating the presence of vacancies. The porous 2D structure with carbon vacancies led to the shortened distances for charge transport to the surface active sites, which facilitated the suppression of the charge recombination. AFM images (Figure 2-6) showed that the thickness of the fl-P-CN nanoplates is evaluated to be around 8.5 nm, much thinner than that of CN (~55 nm, Figure 2-7).

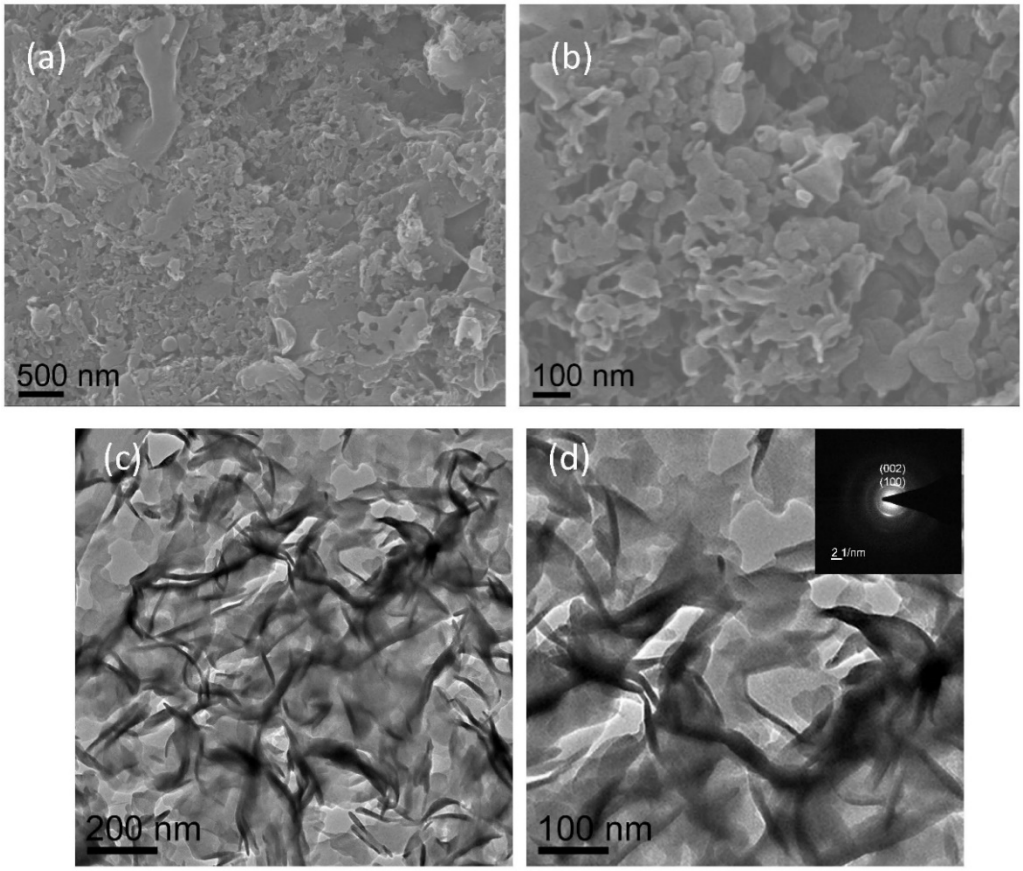

Figure 2-4 Typical SEM graphs of the as-fabricated samples: (a) fl-P-CN and (b) high-resolution SEM of fl-P-CN. TEM graphs of the samples: (c) fl-P-CN and (d) high-resolution TEM of fl-P-CN. Inset shows the SEAD pattern of the fl-P-CN nanoplates.

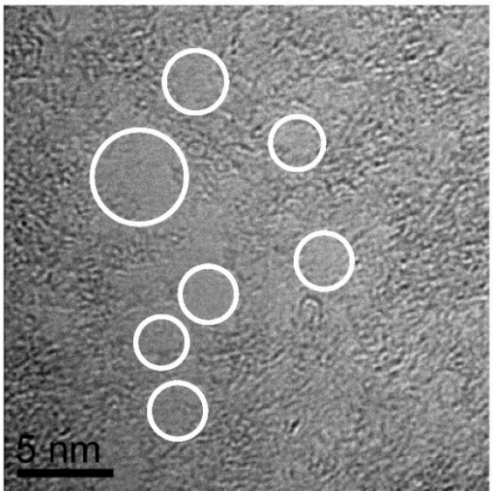

Figure 2-5 High-resolution TEM (HRTEM) image of fl-P-CN.

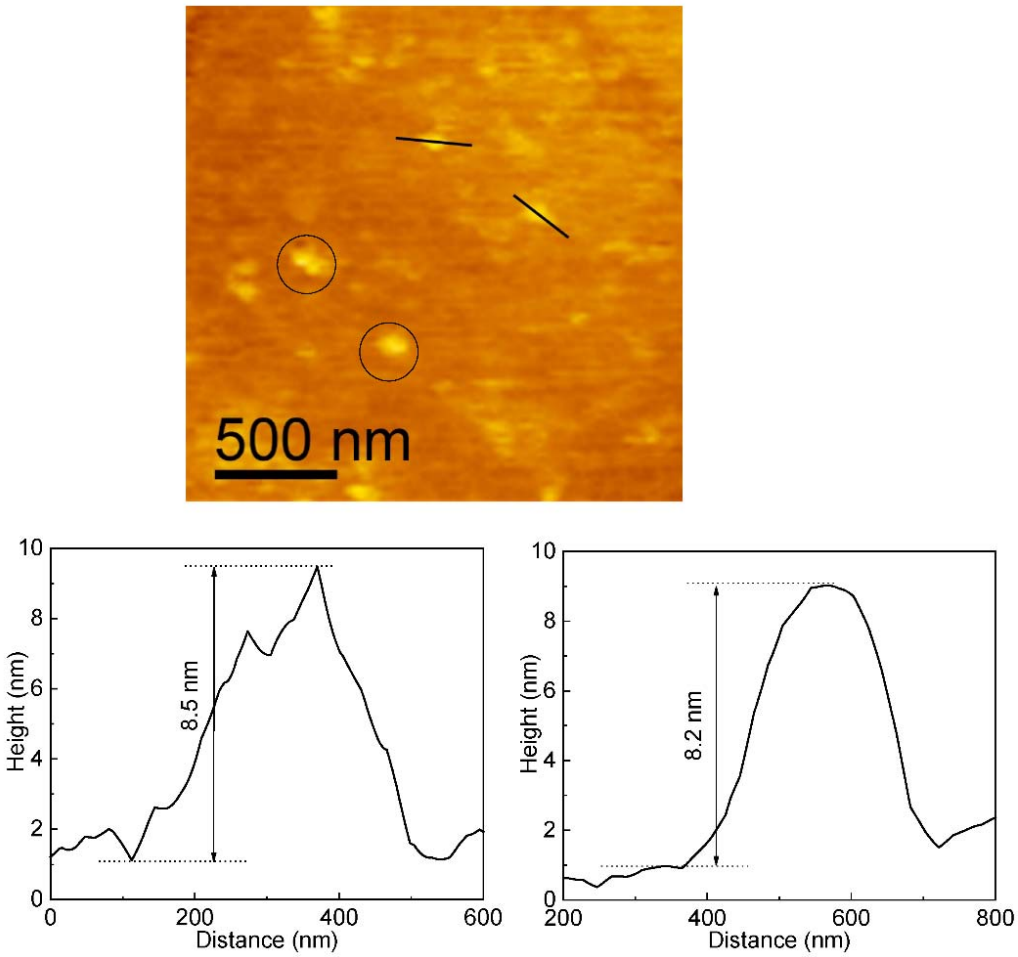

Figure 2-6 AFM image and the corresponding height profile (from left to right) of the fl-P-CN nanosheets.

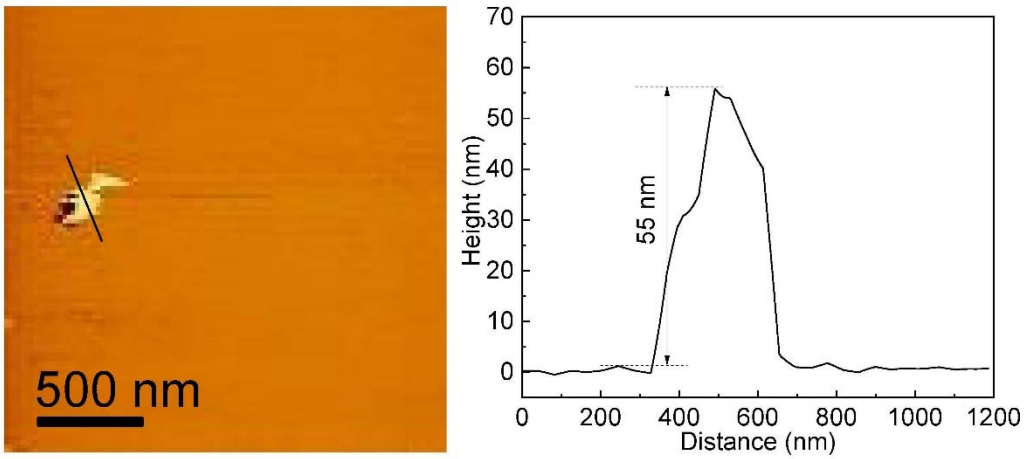

Figure 2-7 AFM image and the corresponding height profile of CN

First-principle density functional theory (DFT) calculations were performed to intuitively understand the mechanism of gas exfoliation of g-C_3N_4 (Figure 2-8). The optimized gallery height of the g-C_3N_4 is found to be 3.5 Å. In contrast, after the N_2 insertion, the optimized structure of the g-C_3N_4 layer becomes expanded and the height of the interlayer gallery is widened to 7.9 Å, which outperforms that of the initial g-C_3N_4 by 2 times. Moreover, the morphology of the optimized g-C_3N_4 presents a bending and crumpling feature, which is consistent with of the TEM graphs. The larger interlayer distance benefits to the insertion of liquid N_2 and also indicates the weaker van der Waals forces between the layers, making it easier to be overcome during the subsequent gasification of liquid N_2 process.

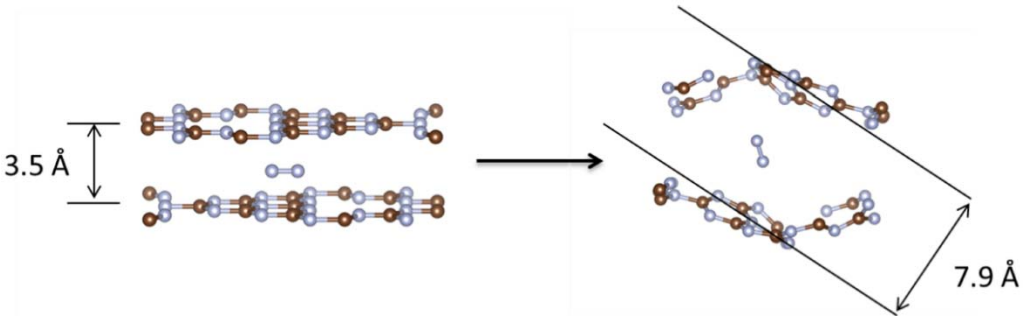

Figure 2-8 Optimized crystal structure of two-layered g-C_3N_4 and N_2-inserted interlayer of g-C_3N_4 based on density functional theory

Figure 2-9 illustrated the N_2 adsorption–desorption isotherms and the relevant pore size distribution plots of the samples and both of them exhibited the type IV isotherm [33,34]. The isotherms both show high adsorption at high-pressure part (P/P_0: 0.8-1), indicating the presence of mesoporous structure [35]. The specific surface area of fl-P-CN reached 70.2 $m^2\ g^{-1}$, which exceeded that of CN (≈6.75 $m^2\ g^{-1}$) by around 12 folds. With respect to CN, the total pore volume also increased obviously for fl-P-CN (0.4 $cm^3\ g^{-1}$ vs. 0.068 $cm^3\ g^{-1}$)). The pore size distribution (PSD) in the inset of Figure 2-9 exhibited that the fl-P-CN possessed wide pore sizes in the 10~200 nm range, which are ascribed to the interlayer galleries and vacancies in the structure of fl-P-CN. Thanks to the enlarged surface area and pore volume, more reactive sites were created for adsorbing more reactants, which is preferred for the mass and charge transfer during the photocatalytic reactions [36].

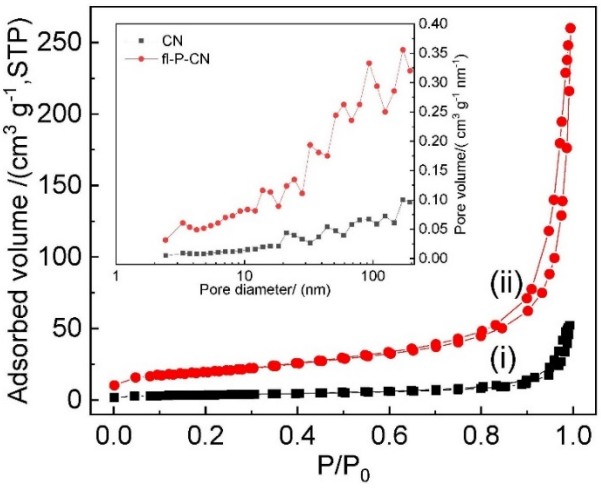

Figure 2-9 N_2 adsorption-desorption isotherms of the as-fabricated (i) CN and (ii) fl-P-CN. The inset is the relevant PSD plots.

Figure 2-10a illustrated the UV–vis DRS spectra of the samples. With respect to the pristine CN, the absorption edge of the fl-P-CN exhibited an remarkable blue shift, which was caused by the quantum confinement effect induced by the few-layered structure [35,37].The band gap of fl-P-CN also increased to 2.77 eV from 2.53 eV for CN. With respect to the bulk CN, the intensity of the absorption tails in the 440~700 nm range increased obviously for fl-P-CN, which was possibly ascribed to the increased inner incident light reflections due to the wrinkled and porous structure [38-40]. Figure 2-10b illustrates the PL spectra of the samples. CN owned PL emission with a broad peak in the 400~700nm range, while the fl-P-CN exhibited remarkable decreased PL intensity, revealing a significant suppression of the charge recombination because of the faster charge transfer at the buckled sites [8,41,42]. Furthermore, Figure 2-10c illustrated the ESR spectra of the samples, both of which exhibited the symmetrical signals with a g value of 2.0036, which is induced by the lone electron pair in the π conjugated aromatic

rings of carbon nitrides [43]. With respect to the CN, fl-P-CN exhibited much stronger ESR intensity, proving the generation of more unpaired electrons in fl-P-CN.

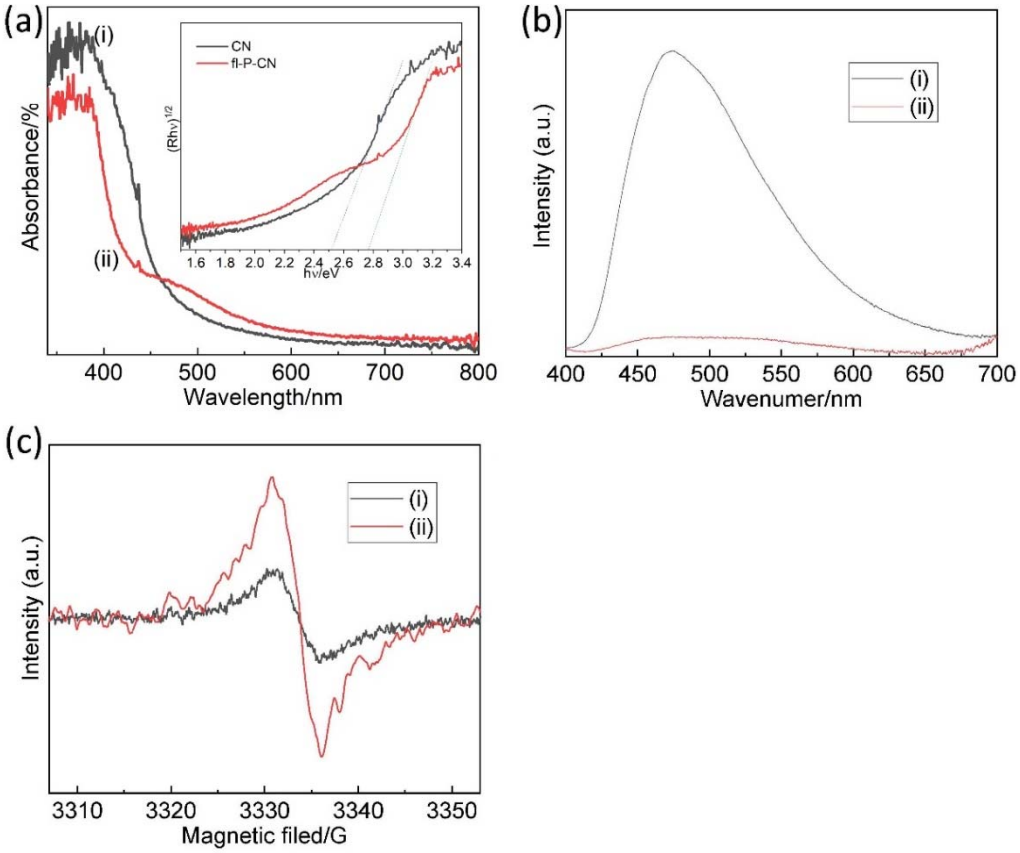

Figure 2-10 (a) UV-vis absorption spectra, (b) PL emission spectra and (c) ESR spectra of the as-fabricated (i) CN and (ii) fl-P-CN.

Figure 2-11a illustrated the transient photocurrent responses of the samples. The photocurrent of fl-P-CN exceeds around 3 times than that of CN, revealing the porous structure of fl-P-CN favor the improvement of the charge separation and transfer [44]. Meanwhile, the Nyquist plots (Figure 2-11b) exhibited that fl-P-CN owned a smaller radius with respect to the pristine CN, further indicating its few-layered porous architecture facilitates the reduction of the charge transfer resistance and thus gave rise to the more efficient charge separation and mobility.

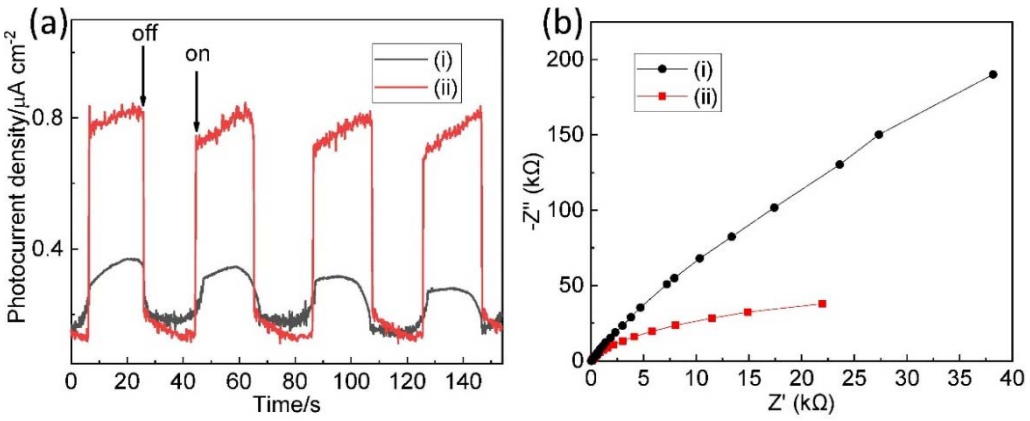

Figure 2-11 (a) transient photocurrent spectra and (b) Nyquist plots of EIS of the as-fabricated (i) CN and (ii) fl-P-CN.

The band structures of the samples are analyzed by the valence-band XPS. Figure 2-12a exhibited that the valence band maximum (VBM) of fl-P-CN is of 1.91 eV and is 0.1 eV smaller than that of the bulk CN (2.01 eV). Figure 2-12b illustrated the schematic band structure of the samples by the combination with the DRS result. The conduction band minimum (CBM) of fl-P-CN exhibited 0.34 eV smaller than that of the bulk CN. It is noted that the higher CB position is in favor of the generation and migration of the photoinduced electrons to the reagents, thus improving the photoactivity effectively [10,37,45].

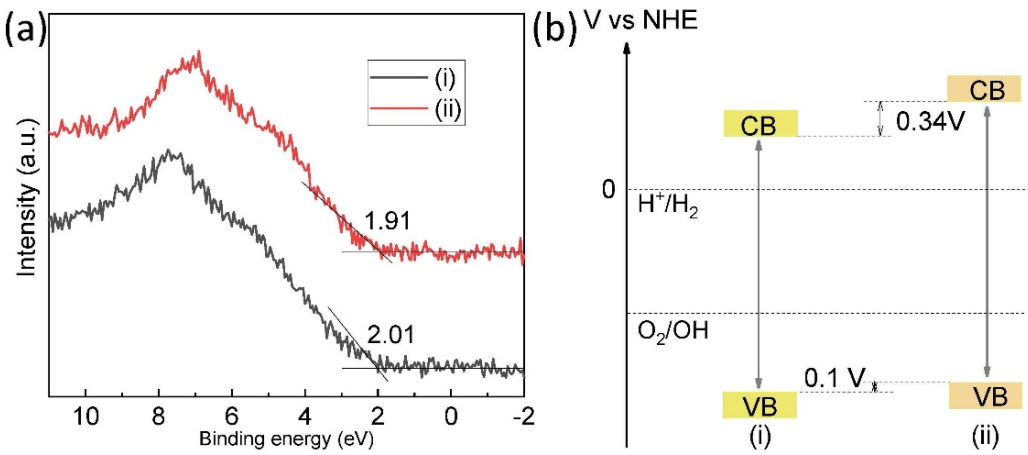

Figure 2-12 (a) XPS valence band spectra and (b) electronic band illustration of the as-fabricated (i) CN and (ii) fl-P-CN.

2.3.2 Photocatalytic Performance.

Figure 2-13a-b illustrated the photoactivities of the samples in hydrogen evolution under visible-light irradiation ($\lambda > 400$ nm). As shown in Figure 2-13a, fl-P-CN exhibited the hydrogen evolution rate around 9 times as high as CN (304 μmol h^{-1} g^{-1} vs. 35 μmol h^{-1} g^{-1}). This significantly improved photoactivity can be explained as the following reasons. Firstly, the removal of graphitic carbon is beneficial for the suppression of the charge recombination in favor of the photocatalytic hydrogen production. Based on the FTIR and Raman results, the more noticeable structure with an improved π-conjugated system also favors the hydrogen reactions. The quantum confinement effect induced by 2D structure speeds up the electron mobility and causes the up-shifted conduction band, giving rise to stronger reducibility during the photoreaction [46]. Secondly, the enlarged surface area endowed the fl-P-CN more surface active sites and accommodation sites for the photoreaction. The high porosity of the fl-P-CN also gives rise to the shorter geometrical diffusion distance for the mass and charge transport to the surface, thus in

favor of the hydrogen production. Figure 2-13b revealed that the fl-P-CN also exhibited robust photostability proved by the minor hydrogen reduction after 4 reaction cycles.

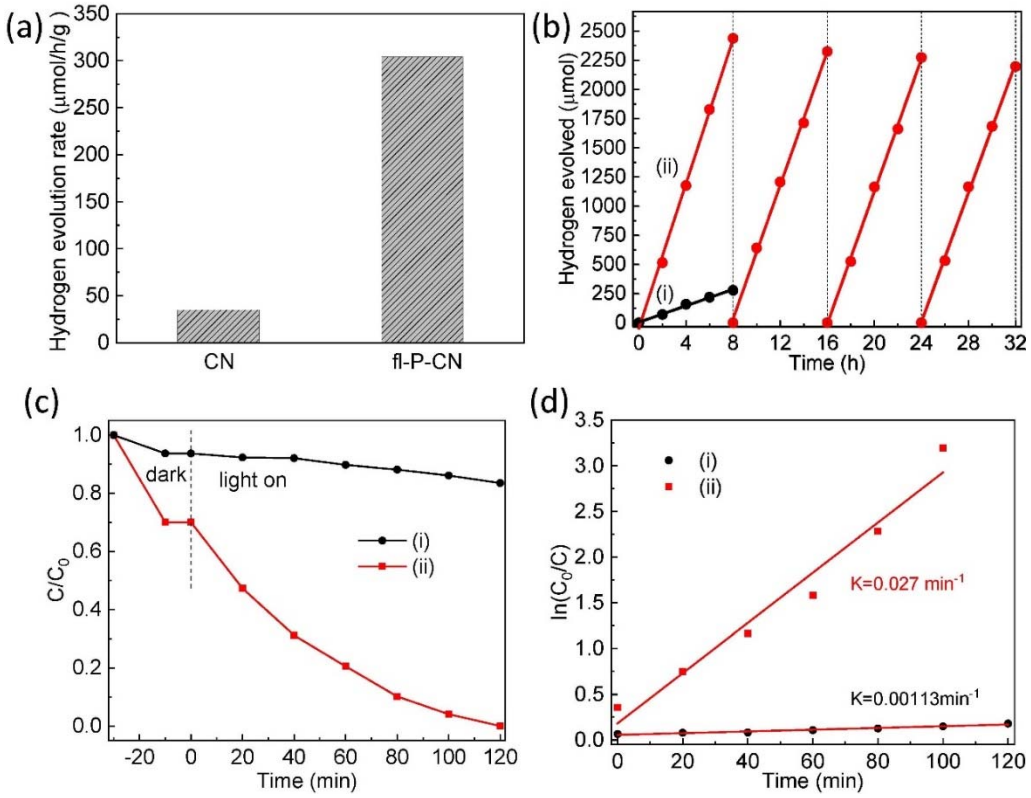

Figure 2-13 (a) Hydrogen evolution rate and (b) test for the stability of hydrogen evolution over the as-fabricated (i) CN and (ii) fl-P-CN nanoplatests. (c) Photodegradation of RhB for CN and fl-P-CN nanoplatests and (d) the relevant kinetic rate constants (K) calculation.

Figure 2-13c-d illustrated RhB degradation performance of the samples under visible-light irradication (λ > 400 nm). fl-P-CN owned competitive degradation efficiency for RhB and most of the RhB is degraded within 120 min. The degradation efficiency of fl-P-CN exhibited about 6 times as high as that of CN, which showed 17% RhB degradation under the same conditions. Figure 2-13d exhibited the calculated apparent degradation rate constants (K) for the RhB degradation. As a result, the K value of fl-P-CN (0.027

min^{-1}) reached about 24 times higher than that of CN (0.0011 min^{-1}). The above results evidenced that the fl-P-CN exhibited remarkably improved degradation efficiency with respect to the pristine CN.

For reference, I prepared CN750 by thermal treatment on the pristine CN at 750 ºC for 10 minutes without l-N_2 immersion. Figure 2-14 exhibited that CN750 owned much lower photocatalytic performance regarding the hydrogen evolution and RhB degradation with respect to the fl-P-CN under visible light irradiation. Meanwhile, as displayed in Figure 2-15a, the N_2 physical absorption-desorption experiment revealed that CN750 has a much smaller surface area than that of the fl-P-CN (25.4 $m^2 g^{-1}$ vs. 70.4 $m^2 g^{-1}$). However, Figure 2-15b exhibited that CN750 has better optical absorbance compared with fl-P-CN probably due to the existence of N defects [24]. As mentioned above, the porous 2D structure can generate more active sites for the photoreaction and also result in faster mass and charge shuttling, thus playing a crucial role in the improvement of photoactivity.

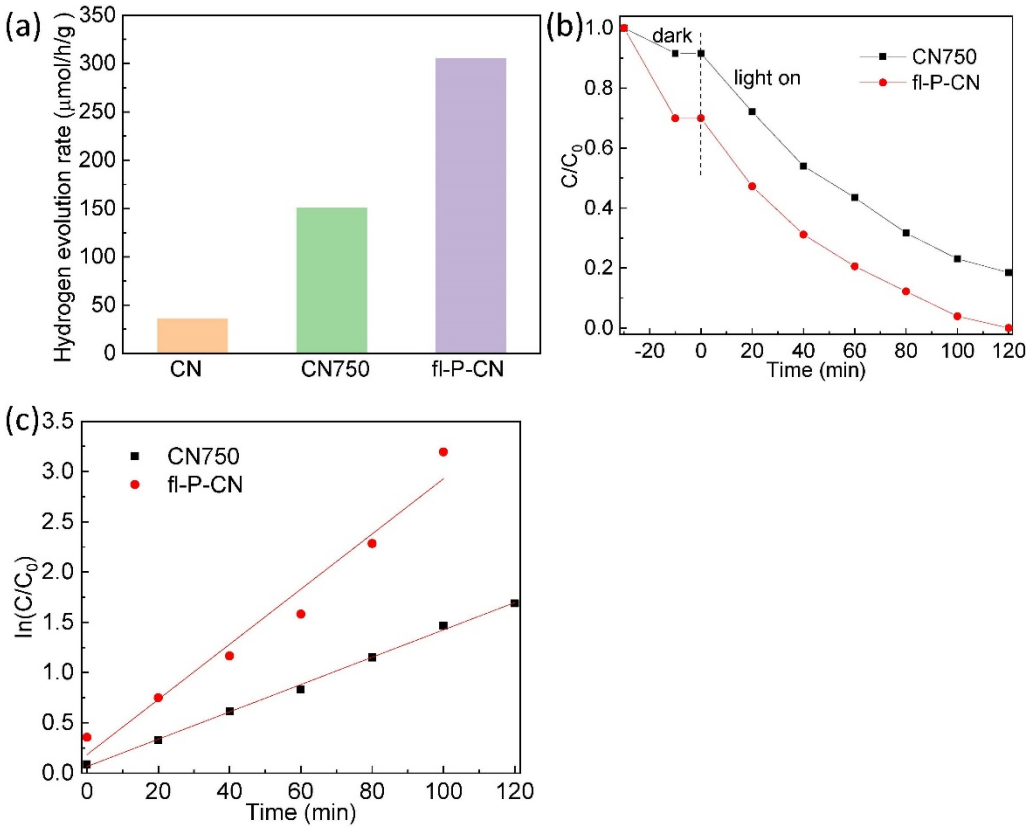

Figure 2-14 (a) Hydrogen evolution rate of the as-fabricated CN, CN750 and fl-P-CN nanoplates. (b) Photodegradation of RhB for CN750 and fl-P-CN nanoplates and (c) the relevant kinetic rate constants (K) calculation

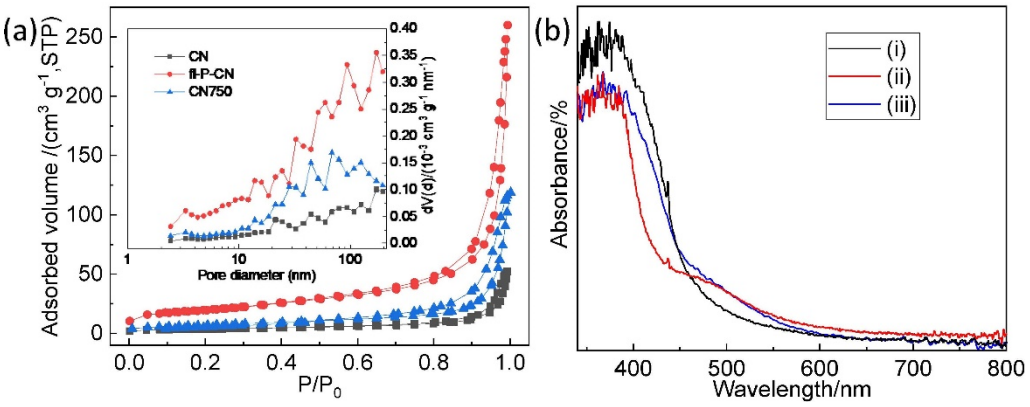

Figure 2-15 (a) N_2 adsorption-desorption isotherms of the as-fabricated CN, fl-P-CN and CN750. The inset is the relevant PSD plots. (b) UV-vis absorption spectra of the as-fabricated (i)CN, (ii)fl-P-CN and (iii)CN750

2.3.3 Mechanism for Photocatalysis

Through introducing triethanolamine (TEOA), isopropyl alcohol (IPA), p-benzoquinone (BQ), and as the scavengers for photo-generated holes (h+), hydroxyl radical (•OH), and superoxide radical ($•O_2^-$), the reactive specie were determined to explain the mechanism of the photoreactions, [47,48]. Figure 2-16a exhibited that the degradation is suppressed with the rate decrease of TEOA > BQ > IPA after adding the scavengers, revealing that the photoinduced holes (h+) have a major role in the photoreaction followed by $•O_2^-$ and •OH, respectively. Figure 2-16b exhibited the possible photoreaction mechanism combined with the above results. When fl-P-CN was subjected to visible light irradiation, it was excited and generated electrons and holes at CB and VB. During the degradation reaction, Electrons can combine with O_2 to produce $•O_2^-$. $•O_2^-$ can accept electron and combine with H+ to produce •OH ($O_2 + e^- \rightarrow •O_2^-$, $•O_2^- + e^- + 2H^+ \rightarrow H_2O_2$, $H_2O_2 + e^- \rightarrow •OH + OH^-$) [49-51]. It is noted that RhB can be oxidized by the $•O_2^-$ and •OH directly. During the hydrogen evolution reactions, TEOA as the sacrificial reagents can be oxidized by the holes and H_2 are generated with the participation of Pt as a cocatalyst when there transferred excited electrons. Therefore, the 2D porous architecture is conducive to the photoreactions which can offer more active sites, promote the electrons mobility and generate more photoexcited carriers due to the expanded bandgap.

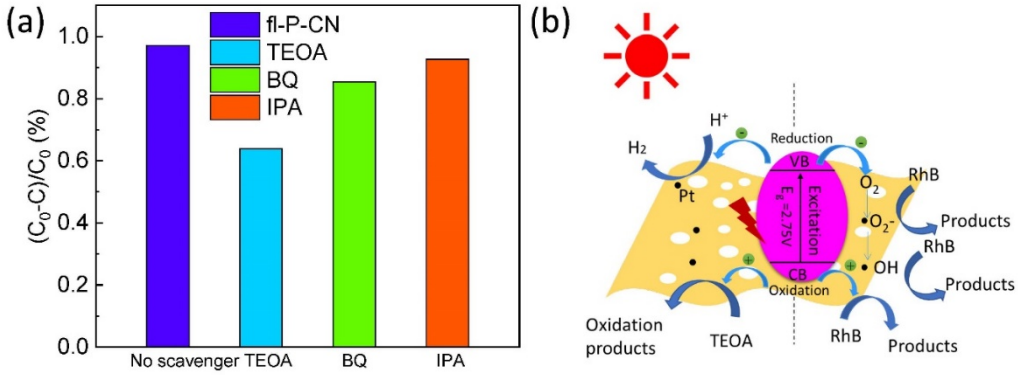

Figure 2-16 (a) The influence of reactive species on the photodegradation of RhB solution by fl-P-CN. (b) Schematic illustration for the photocatalytic activities by fl-P-CN.

2.4. Conclusion

In conclusion, porous g-C_3N_4 nanoplates were successfully obtained by the introduction of a combined fast thermal etching and gas-driven exfoliation strategy. The obtained samples exhibited tailored specific surface area, morphological, electronical and optical structures. With respect to the pristine CN, the fl-P-CN sample exhibited significantly improved photoactivities regarding the hydrogen evolution and RhB degradation under visible light irradiation, which results from its high surface area, modified band energy and promoted charge separation and transfer. This work paves the way for the preparation of the 2D porous g-C_3N_4 with high photoactivity for the solar energy conversion.

References:

1. Y. Qu and X. Duan, *Chem. Soc. Rev.*, 2013, **42**, 2568-2580.
2. X. Chen, S. Shen, L. Guo and S. S. Mao, *Chem. Rev.*, 2010, **110**, 6503-6570.
3. K. Maeda, *J. Photochem. Photobiol. C: Photochem. Rev.*, 2011, **12**, 237-268.
4. X. Wang, K. Maeda, A. Thomas, K. Takanabe, G. Xin, J. M. Carlsson, K. Domen and M. Antonietti, *Nat. Mater.*, 2009, **8**, 76.
5. A. Thomas, A. Fischer, F. Goettmann, M. Antonietti, J.-O. Müller, R. Schlögl and J. M. Carlsson, *J Mat. Chem.*, 2008, **18**, 4893-4908.
6. S. Cao, J. Low, J. Yu and M. Jaroniec, *Adv. Mater.*, 2015, **27**, 2150-2176.
7. W.-J. Ong, L.-L. Tan, Y. H. Ng, S.-T. Yong and S.-P. Chai, *Chem. Rev.*, 2016, **116**, 7159-7329.
8. Q. Liang, Z. Li, Z. H. Huang, F. Kang and Q. H. Yang, *Adv. Funct. Mater.*, 2015, **25**, 6885-6892.
9. J. Zhang, Y. Chen and X. Wang, *Energy Environ. Sci.*, 2015, **8**, 3092-3108.
10. Y. Hong, C. Li, D. Li, Z. Fang, B. Luo, X. Yan, H. Shen, B. Mao and W. Shi, *Nanoscale*, 2017, **9**, 14103-14110.
11. C. Chang, L. Zhu, S. Wang, X. Chu and L. Yue, *ACS Appl. Mater. Interfaces*, 2014, **6**, 5083-5093.
12. Z. Lin and X. Wang, *Angew. Chem.*, 2013, **125**, 1779-1782.
13. P. Niu, L. C. Yin, Y. Q. Yang, G. Liu and H. M. Cheng, *Advanced Materials*, 2014, **26**, 8046-8052.
14. Q. Liang, Z. Li, X. Yu, Z. H. Huang, F. Kang and Q. H. Yang, *Adv. Mater.*, 2015, **27**,

4634-4639.

15. J. Liu, J. Huang, H. Zhou and M. Antonietti, *ACS Appl. Mater. Interfaces*, 2014, **6**, 8434-8440.

16. S. Yang, Y. Gong, J. Zhang, L. Zhan, L. Ma, Z. Fang, R. Vajtai, X. Wang and P. M. Ajayan, *Adv. Mater.*, 2013, **25**, 2452-2456.

17. P. Niu, L. Zhang, G. Liu and H. M. Cheng, *Adv. Funct. Mater.*, 2012, **22**, 4763-4770.

18. M. J. Bojdys, N. Severin, J. P. Rabe, A. I. Cooper, A. Thomas and M. Antonietti, *Macromol. Rapid Commun.*, 2013, **34**, 850-854.

19. X. She, H. Xu, Y. Xu, J. Yan, J. Xia, L. Xu, Y. Song, Y. Jiang, Q. Zhang and H. Li, *J. Mater. Chem. A*, 2014, **2**, 2563-2570.

20. Y. Yang, L. Geng, Y. Guo, J. Meng and Y. Guo, *Appl. Surf. Sci.*, 2017, **425**, 535-546.

21. W. Ding, S. Liu and Z. He, *Chin. J. Catal.*, 2017, **38**, 1711-1718.

22. P. Niu, M. Qiao, Y. Li, L. Huang and T. Zhai, *Nano Energy*, 2018, **44**, 73-81.

23. J. Wen, J. Xie, X. Chen and X. Li, *Appl. Surf. Sci.*, 2017, **391**, 72-123.

24. J. Fu, B. Zhu, C. Jiang, B. Cheng, W. You and J. Yu, *Small*, 2017, **13**, 1603938.

25. J. Zhang, M. Zhang, C. Yang and X. Wang, *Adv. Mater.*, 2014, **26**, 4121-4126.

26. Q. Han, B. Wang, Y. Zhao, C. Hu and L. Qu, *Angew. Chem.*, 2015, **127**, 11595-11599.

27. X. Ji, X. Yuan, J. Wu, L. Yu, H. Guo, H. Wang, H. Zhang, D. Yu and Y. Zhao, *ACS Appl. Mater. Interfaces*, 2017, **9**, 24616-24624.

28. A. B. Jorge, D. J. Martin, M. T. Dhanoa, A. S. Rahman, N. Makwana, J. Tang, A. Sella, F. Corà, S. Firth and J. A. Darr, *J. Phys. Chem. C*, 2013, **117**, 7178-7185.

29. B. Long, J. Lin and X. Wang, *J. Mater. Chem. A*, 2014, **2**, 2942-2951.

30. G. Zhang, M. Zhang, X. Ye, X. Qiu, S. Lin and X. Wang, *Adv. Mater.*, 2014, **26**, 805-809.

31. D. J. Martin, K. Qiu, S. A. Shevlin, A. D. Handoko, X. Chen, Z. Guo and J. Tang, *Angew. Chem. Int. Ed.*, 2014, **53**, 9240-9245.

32. T. Y. Ma, Y. Tang, S. Dai and S. Z. Qiao, *Small*, 2014, **10**, 2382-2389.

33. J. Yuan, J. Wen, Y. Zhong, X. Li, Y. Fang, S. Zhang and W. Liu, *J. Mater. Chem. A*, 2015, **3**, 18244-18255.

34. M. Kruk and M. Jaroniec, *Chem. Mater.*, 2001, **13**, 3169-3183.

35. Y. Li, R. Jin, Y. Xing, J. Li, S. Song, X. Liu, M. Li and R. Jin, *Adv. Energy Mater.*, 2016, **6**, 1601273.

36. Y. Ye, Z. Zang, T. Zhou, F. Dong, S. Lu, X. Tang, W. Wei and Y. Zhang, *J. Catal.*, 2018, **357**, 100-107.

37. P. Yang, H. Ou, Y. Fang and X. Wang, *Angew. Chem. Int. Ed.*, 2017, **56**, 3992-3996.

38. Z. Zhao, X. Wang, Z. Shu, J. Zhou, T. Li, W. Wang and Y. Tan, *Applied Surface Science*, 2018, **455**, 591-598.

39. Q. Liu, X. Wang, Q. Yang, Z. Zhang and X. Fang, *Appl. Surf. Sci.*, 2018, **450**, 46-56.

40. P. Xia, B. Zhu, J. Yu, S. Cao and M. Jaroniec, *J. Mater. Chem. A*, 2017, **5**, 3230-3238.

41. Y. Kang, Y. Yang, L. C. Yin, X. Kang, G. Liu and H. M. Cheng, *Adv. Mater.*, 2015, **27**, 4572-4577.

42. M. R. Gholipour, F. Béland and T.-O. Do, *ACS Sustainable Chem. Eng.*, 2016, **5**, 213-220.

43. Y. Chen, B. Wang, S. Lin, Y. Zhang and X. Wang, *J. Phys. Chem. C*, 2014, **118**,

29981-29989.

44. H. Xu, J. Yan, X. She, L. Xu, J. Xia, Y. Xu, Y. Song, L. Huang and H. Li, *Nanoscale*, 2014, **6**, 1406-1415.

45. W. Iqbal, B. Qiu, J. Lei, L. Wang, J. Zhang and M. Anpo, *Dalton Trans.*, 2017, **46**, 10678-10684.

46. L. Yang, J. Huang, L. Shi, L. Cao, Q. Yu, Y. Jie, J. Fei, H. Ouyang and J. Ye, *Appl. Catal. B: Environ.*, 2017, **204**, 335-345.

47. J. Shu, Z. Wang, G. Xia, Y. Zheng, L. Yang and W. Zhang, *Chem. Eng. J.*, 2014, **252**, 374-381.

48. N. Huang, J. Shu, Z. Wang, M. Chen, C. Ren and W. Zhang, *J. Alloys Compd.*, 2015, **648**, 919-929.

49. M. R. Hoffmann, S. T. Martin, W. Choi and D. W. Bahnemann, *Chem. Rev.*, 1995, **95**, 69-96.

50. Y. Cui, J. Huang, X. Fu and X. Wang, *Catal. Sci. Technol.*, 2012, **2**, 1396-1402.

51. S. Yan, Z. Li and Z. Zou, *Langmuir*, 2010, **26**, 3894-3901.

Chapter 3 Sugar-assisted Mechanochemical Exfoliation of Graphitic Carbon Nitride for Enhanced Visible-light Photocatalytic Performance

3.1 Introduction

The metal-free graphitic carbon nitride (g-C_3N_4) has become a popular photocatalyst since Wang and his coworkers unveiled its capability of the photocatalytic hydrogen production in 2009 [1-5]. As revealed by the following reports, g-C_3N_4 owned the merits of versatility, low price, environmental benign and high physicochemical stability. However, its wide application in photocatalysis is curbed by its low photoactivity as a result of high charge recombination and low surface area [6-12]. So far, numerous attempts have been made to tune the performance of g-C_3N_4, such as the morphological modification, heteroatoms introduction, copolymerization design, and the heterostructures formation [13-22]. Particularly, the nano-sized morphological modulation is regarded as a promising candidate to tailor its photoactivity. Due to their appealing two-dimensional (2D) nanostructure, g-C_3N_4 nanoplates exhibited several novel properties including the high surface area, abundant active sites and rapid charge mobility, which endows them with promising future in photocatalysis [23-29].

To date, there have developed various methods to obtain the 2D g-C_3N_4 such as thermal etching exfoliation, chemical exfoliation, mechanical exfoliation and ultrasonic-assisted exfoliation [26,28,30-33]. Unfortunately, the chemical and ultrasonic-assisted exfoliation strategies usually use corrosive acids/alkalis and/or organic chemicals (IPA and DMF) as

the solvents [26,31-33], which is detrimental to the environment. Besides, during the thermal etching process, large amount of hazardous gas will be released upon resolving of the carbon nitride [28]. Furthermore, reports on the green exfoliation only remain a few such as the ultrasonic-assisted exfoliation in water [34-36]. This sonication method also has the shortcomings of the long-time operation and unfavorable production (~0.5 mg ml^{-1}). Recently, mechanochemistry has emerged as an efficient and sustainable approach for the synthesis and modification of g-C_3N_4 nanoplates [37-39]. For example, Ji and his coworkers adopted the mechanical method for the exfoliation and modification of the pristine g-C_3N_4 with aromatic molecules via π-π stacking interactions [39]. But the use of the harmful and/or expensive reagents is unfavorable for the scale-up and the ball-milling method also requires high-priced laboratory machine. Therefore, the proposal for the preparation of g-C_3N_4 nanoplates in a sustainable routine is in demand.

In this work, a co-grinding strategy was raised for the preparation of ultrathin g-C_3N_4 nanoplates in a sustainable way. With the assistance of fructose, the efficient exfoliation of the pristine g-C_3N_4 can be achieved with the ultrathin g-C_3N_4 nanoplates concentration of 2.3 mg mL^{-1}. In comparation of the bulk g-C_3N_4, the g-C_3N_4 nanoplates exhibited several novel features such as 2D structure, high surface area, abundant exposed active sites and promoted charge transfer rate. As a result, the water-soluble g-C_3N_4 nanoplates exhibited a remarkably improved photoactivity and exceeds that of the bulk g-C_3N_4 3 times toward the hydrogen evolution and 6 times toward RhB degradation, respectively.

3.2. Experimental details

3.2.1 Sample preparation

The pristine g-C_3N_4 was obtained after the melamine was subjected to heating to 550 ^oC for 4 h with a heating rate of 2.3 ^oC min^{-1}. Followed by cooled naturally and ground into powder, the resultant products was denoted as GCN.

Afterwards, the bulk GCN were mixed with fructose at the mass ratio of 1:5 and ground for 2.5h at about 160 rpm with a mortar and pestle. The mixture was then dissolved and sonicated in water for 1h. After removing the thick sheets via centrifugation, the supernatant was collected and washed with 200 ml water, then followed by filtration through a polytetrafluoroethylene (PTFE) membrane. After dried in a freeze-dryer, the final products were gained with the production rate of 37.5% and labeled as f-CNNP. The sample synthesized under the assistance of sucrose were named as s-CNNP with the production of 40%.

3.2.2 Photocatalyst characterization

XRD was performed on an X-ray diffractometer (Rigaku Miniflex 600). Raman was conducted on a Raman microscope (Renishaw inVia reflex). FTIR spectra were recorded by JASCO FT/IR-4600 spectrometer. XPS spectra were recorded by a JEOL JPS-9200. The morphologies were explored by SEM (JEOL JSV-6510LA) and TEM (JEOL JEM-2010 TEM). The PL spectra were recorded on a JASCO FP-8000. The DRS were carried out on a UV-visible spectrometer (JASCO V-750). BET N_2-adsorption measurement were performed on a Quantachrome Autosorb-iQ2. ESR spectra were recorded by an ESR spectrometer (JEOL JES-FA 200). EIS were measured using solartron 1260/1287. The transient photocurrent of the samples loaded on an ITO sheet were measured using a

three-electrode cell with Ag/AgCl vs. an aqueous electrolyte of a 0.5 M Na_2SO_4 solution.

3.2.3 Photocatalytic Hydrogen Production Test

The Photocatalytic hydrogen evolution from water was performed in a closed glass container under visible light excitation using TEOA as electron donor. First, 30 mg photocatalyst was dissolved in a 28ml of 10% TEOA aqueous solution. 3 wt% Pt was served as the co-catalyst and loaded via the *in situ* photodeposition method. Before illumination, N_2 was introduced for 30 minutes to expel the air followed. The light source is provided by a 150 W xenon lamp with an optical cut-off filter ($\lambda > 400$ nm). The evolved H_2 was detected using a gas chromatograph within a thermal conductivity detector.

3.2.4 Photocatalytic RhB Degradation Test

In a typical evaluation of the RhB degradation performance, 25 mg of the sample was added to 50 mL RhB solution (10 mg/L). The suspension was then ultrasonicated for 10 min followed by stirring for 20 min in the dark to achieve the adsorption equilibrium. 3 mL of the solution was sampled every 20 minutes and analyzed using a UV-visible spectrometer. The reactive oxidation species were investigated by additionally adding benzoquinone (BQ), isopropanol (IPA), and triethanolamine (TEOA) to the RhB dispersion to trap the superoxide radicals ($\bullet O_2^-$), hydroxyl radicals (•OH) and superoxide holes (h+), respectively.

3.3. Results and discussion

Figure 3-1 displayed the major exfoliation process. When the mixture of the g-C_3N_4

and sugar crystals were subjected to grinding, there produced shearing and compressive forces between them, giving rise to the small-sized g-C_3N_4 with fewer layers. Meanwhile, more sugar crystals with abundant hydroxyl groups (–OH) are able to attach on the more exposed surfaces of the g-C_3N_4, thus giving rise to the enhanced interactions between them. As g-C_3N_4 analogous to graphite, it is imaged that the –OH groups play an important role in the interactions between the sugars and g-C_3N_4, also a similar role in the exfoliation of the graphite [40]. The obtained f-CNNP via a freeze-drying treatment could be easily dispersed in water and remained stable up to 3 days. For reference, NaCl is used as the assistance in the co-grinding process under the same conditions, which could efficiently disintegrate the nanodiamond aggregates [41]. However, CNNP with very low concentration (Figure 3-2) was gained. Furthermore, similar results were obtained when melamine and boric acid acted as the exfoliation agent under the identical conditions (Figure 3-2). Additionally, raffinose crystals also served as the exfoliation assistance and the obtained g-C_3N_4 nanoplates concentration reached as high as 2mg ml^{-1}. The above results proved the existence of interactions between sugar molecules and g-C_3N_4, leading to the g-C_3N_4 nanoplates highly soluble in water.

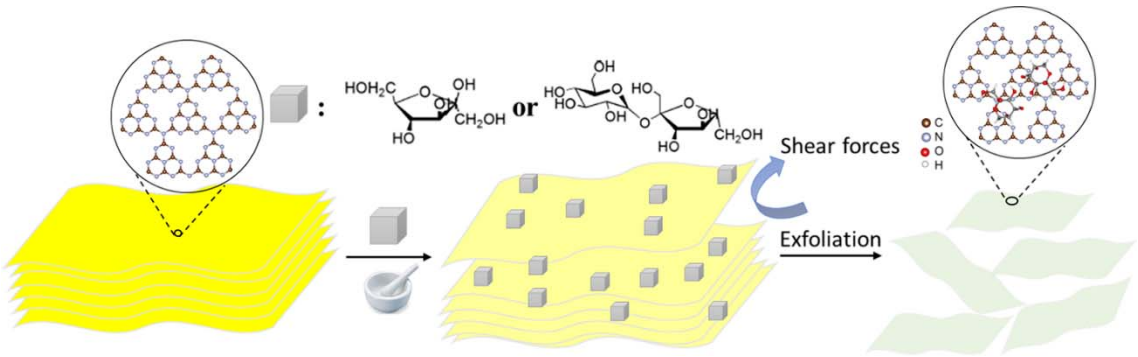

Figure 3-1 Illustration of the exfoliation procedure

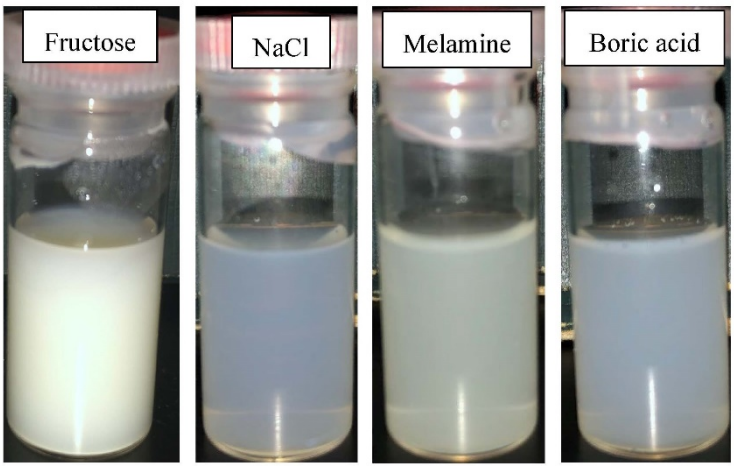

Figure 3-2 Photographs of f-CNNP dispersed solutions in water after co-grinding with fructose, NaCl, melamine, and boric acid

Figure 3-3A illustrated the XRD patterns of the samples. The XRD pattern of GCN exhibited two main diffraction peaks at 27.4° (002) and 13.1° (100), ascribed to the interlayer packing and the in-plane stacking structure, respectively [42,43]. The diffraction peaks of f-CNNP and s-CNNP exhibited locations close to those of the GCN, revealing their retained carbon nitride framework upon the grinding process. However, the peak intensities of f-CNNP and s-CNNP become smaller in comparison with GCN, suggesting the their highly reducd planar size as well as lessened thickness as a result of the milling-induced delamination [23,28]. Figure 3-3B illustrated the Raman spectra of the samples. For GCN sample, the wide peak in the 1200–1700 cm^{-1} range is attributable to the C–N stretching vibrations and the two obvious peaks at 708 and 978 cm^{-1} are due to the breathing modes of the heptazine rings [44,45]. The Raman spectra of f-CNNP and s-CNNP exhibited similar profiles with weakened peak intensities compared to the GCN, indicating their unaltered structure upon the milling treatment.

Figure. 3-3C illustrated the FTIR spectra of GCN, fructose and f-CNNP. The FTIR

spectra of the bulk GCN and f-CNNP exhibited similar absorption profiles, indicating the maintained chemical structure of the f-CNNP. The peaks in the 1200-1650 cm^{-1} range are caused by the stretching vibrations of the C-N heterocycles. The broad peaks around 3300 cm^{-1} are typical stretching vibration modes of the N-H and O-H stretches and the peaks at 811 cm^{-1} originate from the breathing modes of the heptazine rings [46-48]. The extra peaks at 1073 cm^{-1} and in the 2800~3000 cm^{-1} range for f-CNNP (Figure 3-3C) originate from the C-O and C−H vibrations of fructose, confirming the absorption of fructose on the surface of f-CNNP [49]. Additionally, a blue-shift of the absorption peaks for f-CNNP were observed, probably caused by the quantum confinement effect (Figure 3-3D) [37]. Figure 3-4 illustrated the FTIR spectrum of GCN, sucrose and s-CNNP. The appearance of C−OH stretching vibration for s-CNNP revealed the absorption of sucrose.

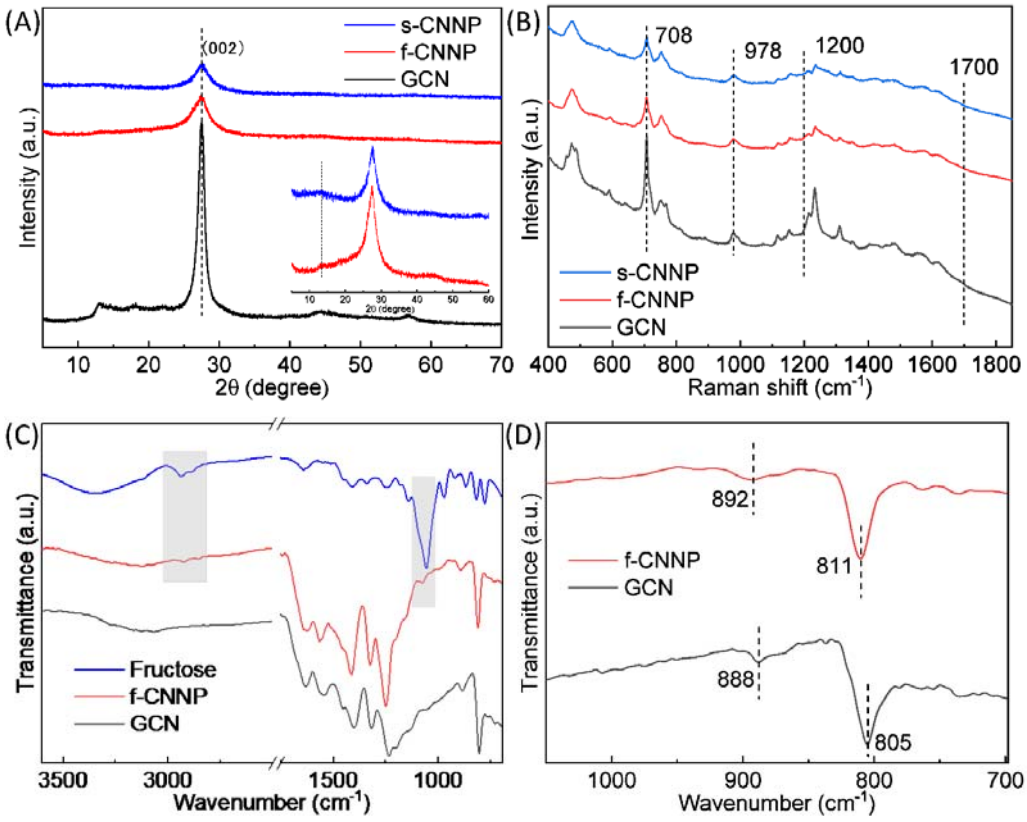

Figure 3-3 (A) XRD patterns (B) Raman spectra, (C,D) FT-IR spectra of the as-prepared

GCN and f-CNNP

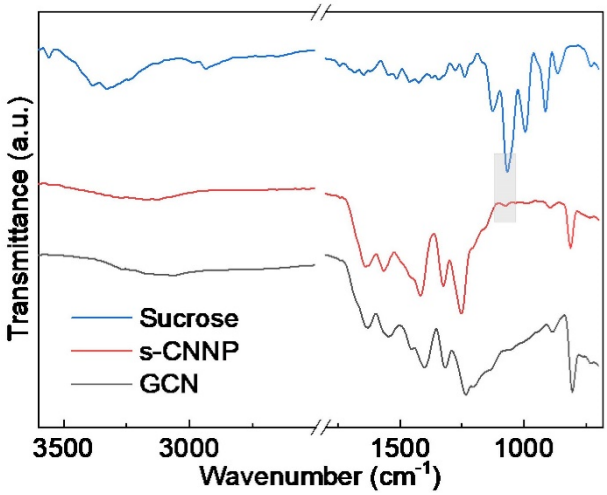

Figure 3-4 FTIR spectra of GCN, sucrose and s-CNNP

XPS was conducted to probe the chemical details of the samples. The XPS quantitative analysis exhibited that the C/N atomic ratio of f-CNNP (0.78) slightly raised with respect to that of GCN (0.76), indicating the existence of fructose absorbed on the f-CNNP. Figure 3-5A illustrated that two typical peaks at 287.9 eV and 285.0 eV are obtained after resolving the high resolution C1s XPS spectrum of the bulk GCN, originating from the C=N–C and sp^2 C=C bonds in the aromatic rings, respectively. In addition, an extra peak at 286.1 eV can be obtained for f-CNNP, corresponding to the sp^3 C ($C\text{-}(N)_3$) in the carbon nitride structure [9,23,50]. What's more, the peak of C=C for f-CNNP exhibited small shift to a smaller binding energy with respect to that of GCN, indicating the slightly changed distribution of carbon atoms. Figure 3-5B illustrated that separating the high resolution N 1s spectra can obtain four typical peaks at 404.2 eV, 400.8 eV, 399.4 eV and 398.4 eV, stemming from the π excitation, N–H, $N\text{–}(C)_3$, and C=N–C bonds, respectively [9,23,51]. The f-CNNP and GCN shared the same nitrogen species, while the peak area ratio of the $C\text{–}N\text{=}C/N\text{–}(C)_3$ of f-CNNP raised from 2.83 (GCN) to 3.30. The smaller N–

$(C)_3$ ratio for f-CNNP is probably caused by breaking the sp^3 N–$(C)_3$ bonds during the grinding exfoliation. The XPS of s-CNNP was also performed, which is presented in Figure 3-6.

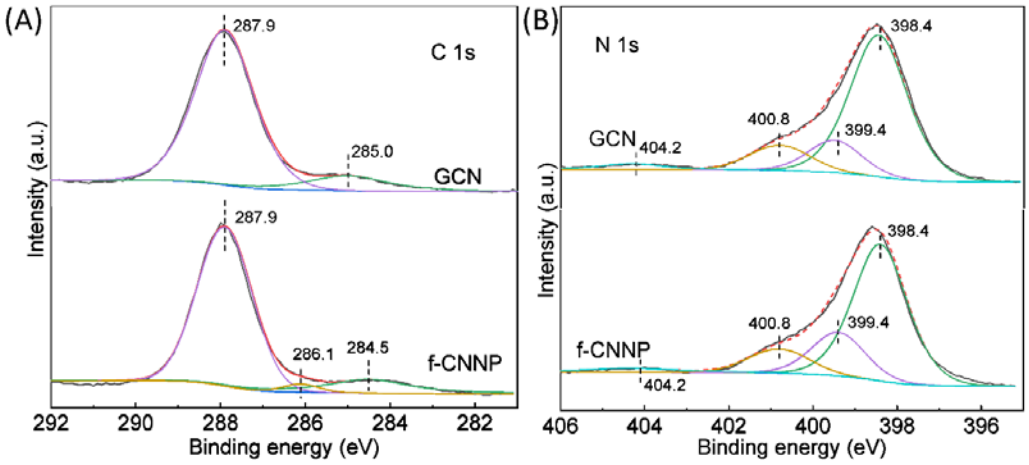

Figure 3-5 High-resolution (A) C1s and (B) N1s XPS spectra of the as-synthesized (a) GCN and (b)f-CNNP

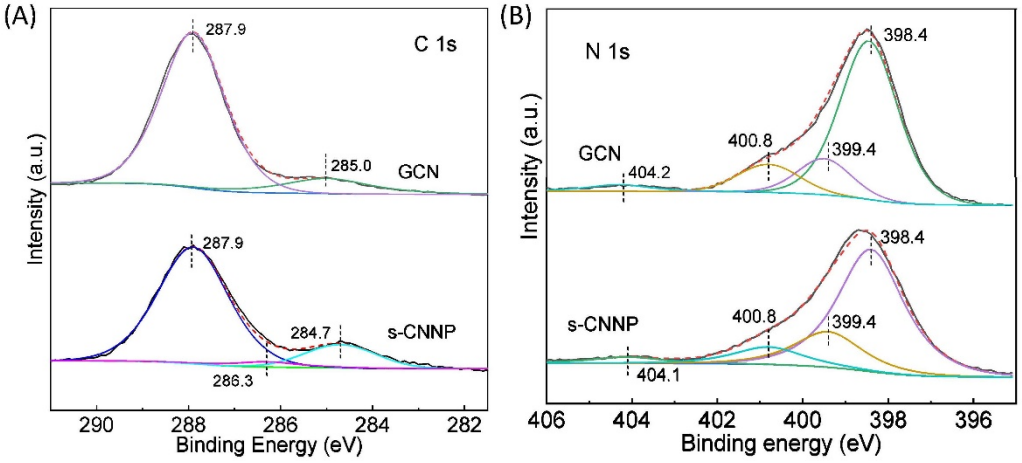

Figure 3-6 High-resolution (A) C1s and (B) N1s XPS spectra of the as-synthesized (a) GCN and (b)s-CNNP

SEM and TEM were carried out to explore the morphologies of the samples. Compared with the bulk GCN with aggregated layers, Figure 3-7A exhibited that the f-CNNP sample was broken and peeled with remarkably reduced lateral size (~200 nm) and thickness (<3

nm) after the grinding exfoliation. The similar phenomenon was also observed for s-CNNP, the size of which even became smaller (~100 nm) upon the milling process (Figure 3-7B). TEM images in Figure 3-7C-D further confirmed the effect of the milling exfoliation and exhibited the laminar morphology of f-CNNP, which are almost transparent due to their ultrathin thickness [52]. AFM images also revealed that the f-CNNP was around 3 nm thick (Figure 3-8). For reference, sonication treatment of the bulk GCN in the fructose solution was performed. Compared with the milky-like CNNP solution, the obtained dispersion after centrifugation in Figure 3-9A was clear and transparent, indicating the importance of grinding for the exfoliation process. Meanwhile, the grinding treatment of GCN without adding fructose was also conducted. The solution after centrifugation is also transparent (Figure 3-9B), reflecting that the fructose as the exfoliation agent plays a key role in the efficient delamination of carbon nitride.

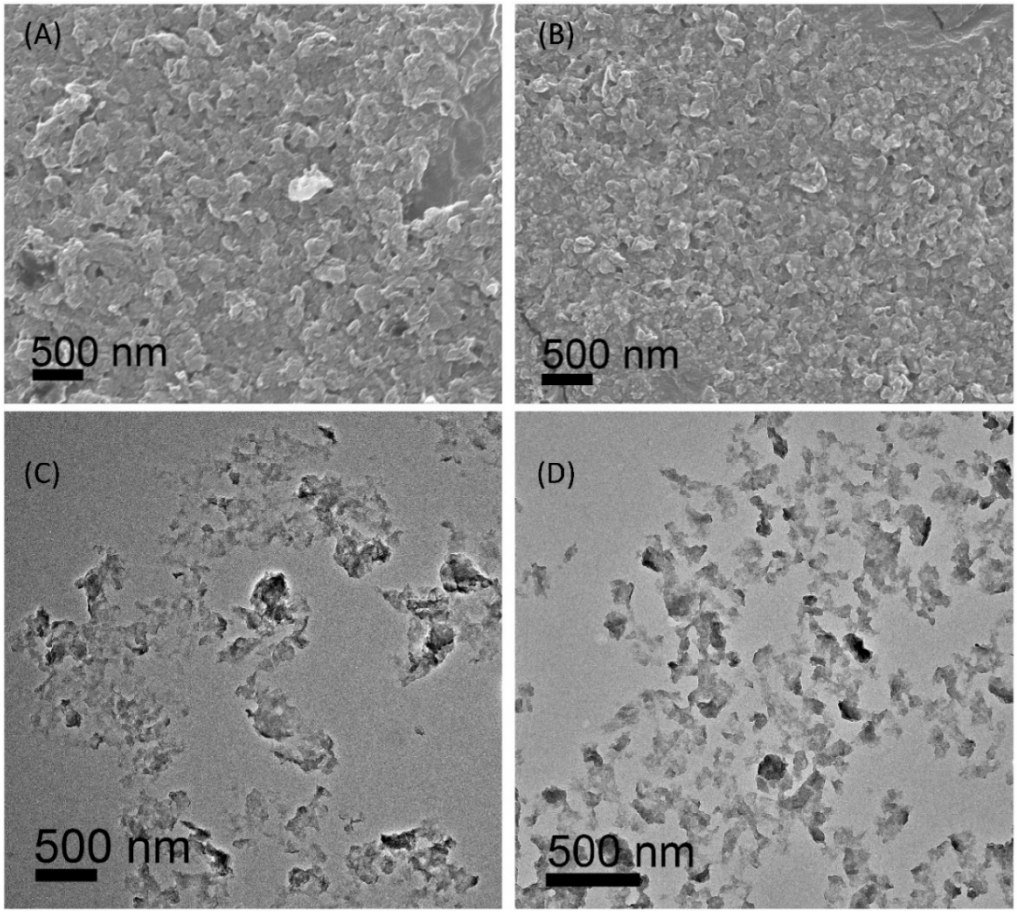

Figure 3-7 Typical SEM of the as-synthesized (A) f-CNNP and (B) s-CNNP. TEM images of as-synthesized (C) f-CNNP and (D) s-CNNP.

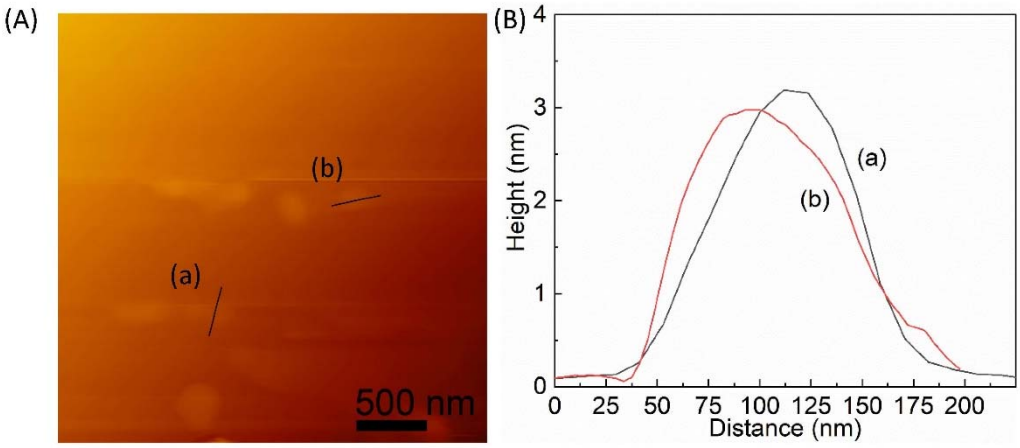

Figure 3-8 (A) AFM image of f-CNNP on the Si substrate (B) Height profile along the line in (A)

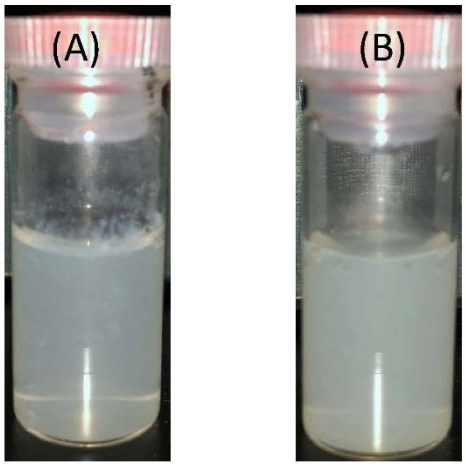

Figure 3-9 Images of (A) sonicated g-C_3N_4 in fructose solution for 1h after concentration and (B) suspensions of milled g-C_3N_4 in water followed by sonication for 1h without fructose after concentration.

Figure 3-10 illustrated the nitrogen adsorption-desorption isotherms of the samples and their pore size distribution curves. All the samples exhibited the type *IV* isotherms with H3 hysteresis, especially for f-CNNP and s-CNNP, which mostly originated from the mesopores [53-55]. The surface area of the f-CNNP and s-CNNP were estimated around 57.4 $m^2\ g^{-1}$ and 81.3 $m^2\ g^{-1}$, which exceeds that of GCN (10.1 $m^2\ g^{-1}$) by 6 and 8 times, respectively. A wide pore size distribution in the 10-200 nm range for f-CNNP were observed based on the Barret–Joyner–Halenda (BJH) analysis, which probably arose from the slit-like pores existed between the nanoplates. The pore volumes of f-CNNP (0.2676 $cm^3\ g^{-1}$) and s-CNNP (0.3020 $cm^3\ g^{-1}$) were also much higher than that of the bulk GCN (0.064 $cm^3\ g^{-1}$). The enlarged surface area of the photocatalysts is beneficial to create more active sites for accommodating more reactant molecules, while the novel 2D structure facilitated the mass and charge transfer to the surface reaction sites in favor of the photocatalysis.

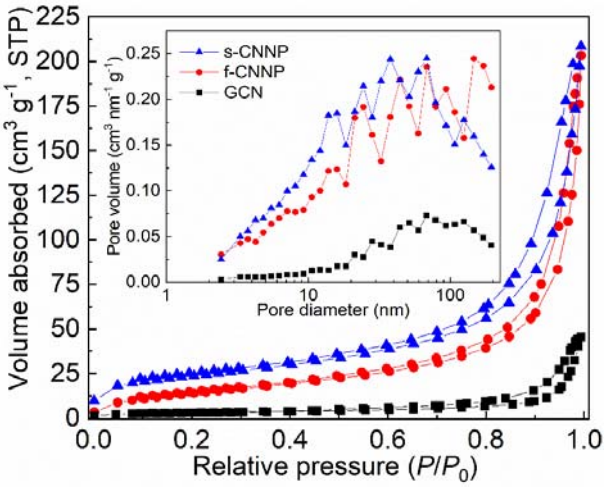

Figure 3-10 N_2 adsorption/desorption isotherms of the as-synthesized GCN, f-CNNP and s-CNNP. The inset is the corresponding pore size distribution plots

UV-vis diffuse reflectance and photoluminescence (PL) spectra were analyzed to explore the optical information of the samples in details. Figure 3-11A illustrated that there is an obvious blue shift of the absorption edge from 480 nm for GCN to 450 nm for f-CNNP and s-CNNP. Accordingly, the bandgaps for the GCN, f-CNNP and s-CNNP were estimated around 2.75, 3.0 and 3.0 eV, respectively, by inferring the linear region of the Tauc plots in Figure 3-11A. The expanded bandgaps of f-CNNP and s-CNNP are caused by the quantum confinement effect induced by the reduced size and thickness [55,56]. Figure 3-11B illustrated the PL spectra of the samples, the wide emission peak of which is caused by the charge radiative recombination [57]. The PL peak of the f-CNNP and s-CNNP also exhibited an obvious blue-shift from 474 nm for GCN to 455 nm, which is in consistent with the UV-Vis absorption edge alteration. ESR spectroscopy was further carried out to identify unpaired electrons existed in the photocatalysts. Figure 3-11C illustrated that one single Lorentzian line with a g value around 2.0035 can be the observed for all the samples, which is associated with the unpaired electrons in the

conduction band [58]. The stronger signal for f-CNNP and s-CNNP revealed the existence of more unpaired electrons than GCN, which can act as the active radical pairs during the photoreactions [51].

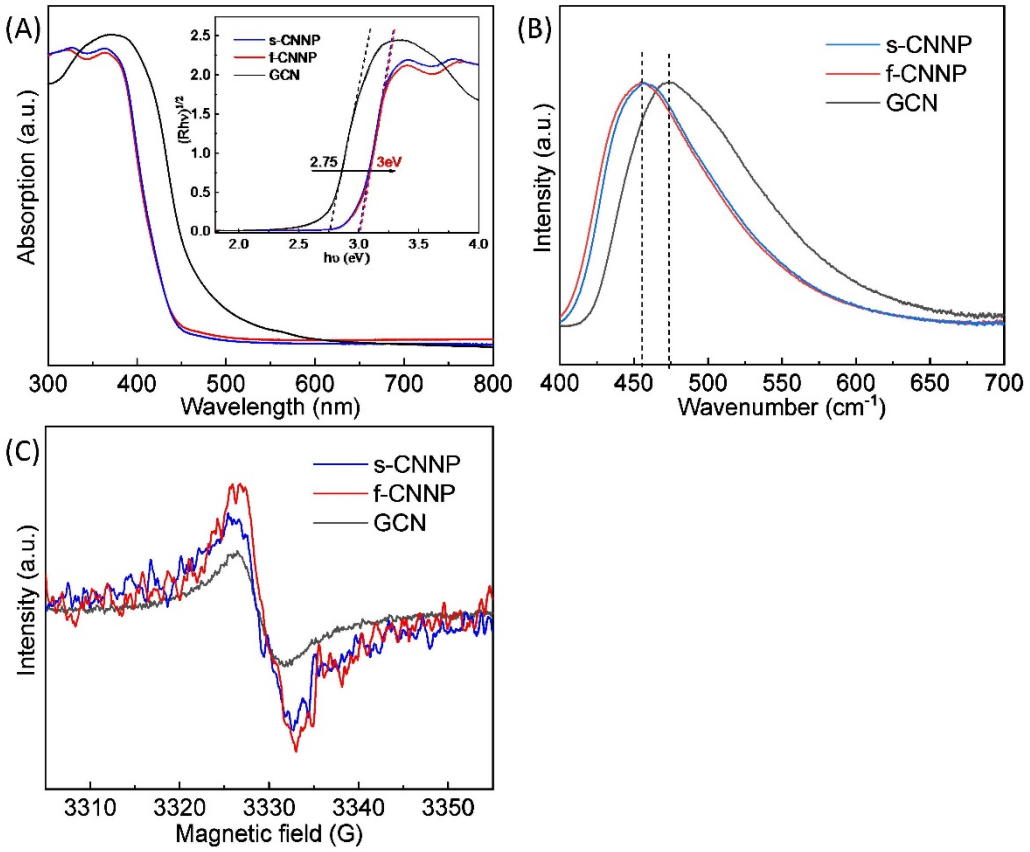

Figure 3-11 (A) UV-vis absorption spectra, (B) PL emission spectra and (C) ESR spectra of the as-synthesized GCN, f-CNNP and s-CNNP

Figure 3-12A illustrated the transient photocurrent of the samples for three one-off cycles. The higher photocurrent value means the more efficient charge generation and transfer, indicating the suppressed charge recombination. A prompt and reproducible photocurrent signal was observed for every illumination. Similar photocurrents but larger than GCN are revealed for f-CNNP and s-CNNP upon illumination, suggesting that the 2D structure gives rise to inhibited charge recombination and improved charge carrier separation. EIS was further carried out to explore the interfacial charge transfer of the

catalysts. Figure 3-12B illustrated that the EIS semicircle arc radius of f-CNNP is the smallest followed by s-CNNP and GCN, implying its smallest charge transfer resistance thus best charge mobility rate due to its 2D structure in favor of the charge transfer.

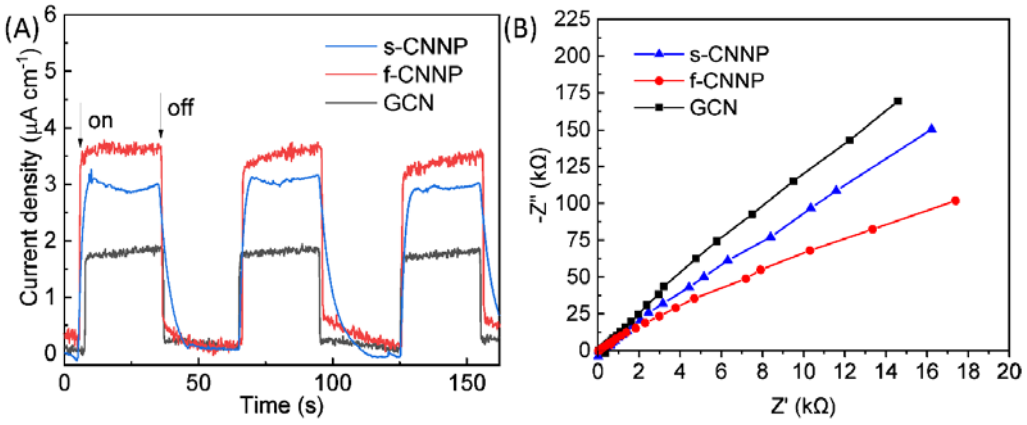

Figure 3-12 (A) transient photocurrent results and (B) Nyquist plots of EIS of the as-synthesized GCN, f-CNNP and s-CNNP

Valence-band (VB) XPS was carried out to identify the impact of delamination on the VBM and CBM of the samples. Figure 3-13A exhibited that GCN, f-CNNP and s-CNNP has the VBM of 1.99, 1.94 and 1.99 eV, respectively. Based on the the bandgap energies derived from the DRS results, the CBM were calculated around -0.76, -1.06 and -1.01 eV for GCN, f-CNNP and s-CNNP, respectively, implying that f-CNNP and s-CNNP have a negative shift of 0.3 and 0.25 eV compared to GCN, respectively. Figure 3-13B illustrated the electronic structures of photocatalysts on the basis of their VB, CB potential and band gap. The CBM of f-CNNP and s-CNNP exhibited upshift compared to that of GCN, implying their better reducibility in the photoreactions [56,59].

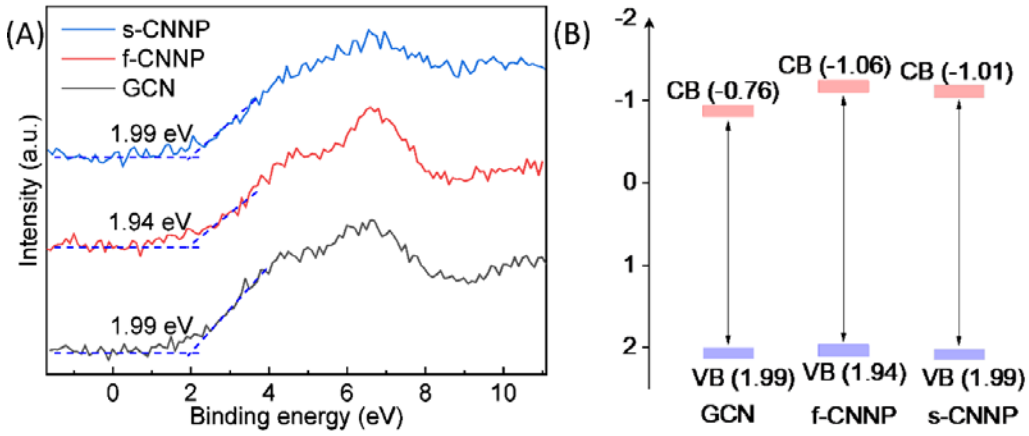

Figure 3-13 (A) XPS valence band spectra and (B) electronic band structures of the as-synthesized GCN, f-CNNP and s-CNNP

Figure 3-14A illustrated the photoactivities of the samples for H_2 production under visible light illumination (>400 nm). Among the three samples, f-CNNP exhibited the best H_2 production efficiency and its evolution rate reached 103.7 μmol h^{-1} g^{-1}, compared to that of 66.7 μmol h^{-1} g^{-1} for s-CNNP and 37.7 μmol h^{-1} g^{-1} for GCN, respectively. The H_2-evolution efficiency of f-CNNP exceeds that of GCN by three times, and s-CNNP also exhibited the evolution rate about two-fold higher than that of GCN, revealing their unique 2D structures are favorable for the water splitting reactions. Moreover, the stability test of f-CNNP reveals a continuous H_2 evolution after reacting for three cycles, proving its excellent stability (Figure 3-14B). The XRD pattern of the f-CNNP after three cycles of photocatalytic H_2 production was also collected, which further verified its impressive stability (Figure 3-15). In addition, f-CNNP also exhibited a superior H_2 evolution rate of 690 μmol h^{-1} g^{-1} than that of 309 μmol h^{-1} g^{-1} for s-CNNP and 181 μmol h^{-1} g^{-1} for GCN under the full spectrum irradiation of the Xe lamp (Figure 3-14C). The effect of variations in weight ratio (1:3, 1:4, 1:5, 1:6 and 1:7) of GCN:fructose on the photocatalytic performance were also explored with a mechanochemical treatment time of 2.5 h. In this

study, the weight ratio of GCN:fructose was fixed at 1:5 to obtain f-CNNP with suitable hydrogen production rate at low cost. The much higher photoactivity of f-CNNP for H_2 generation can be explained by its modified textural, structural and electronic properties. First, this water-soluble 2D f-CNNP endows a largest exposure of the catalytic species with the photocatalysts due to its good dispersibility and abundant active sites due to the enlarged surface area. Furthermore, because of the quantum confinement induced by the small-sized and thinner f-CNNP, the charge migration and separation are enhanced for better redox reactions [60]. It is noted that s-CNNP exhibited obviously larger surface area but lower photoactivity than the f-CNNP, because, the crystallinity influences more for uphill reaction of water splitting than the surface area which plays an important role in the organic pollutants degradation [61].

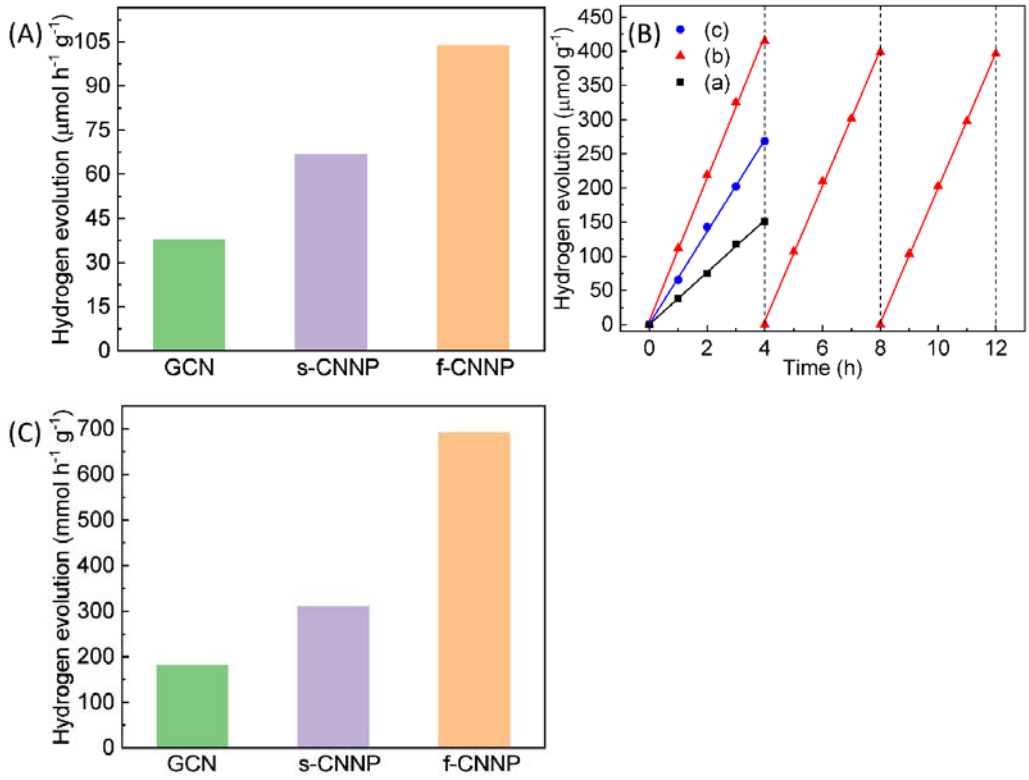

Figure 3-14 (A) Visible-light hydrogen evolution rate, (B) stability test of hydrogen production and (C) hydrogen production rate under full spectrum illumination over the as-synthesized (a) GCN, (b) f-CNNP and (c) s-CNNP.

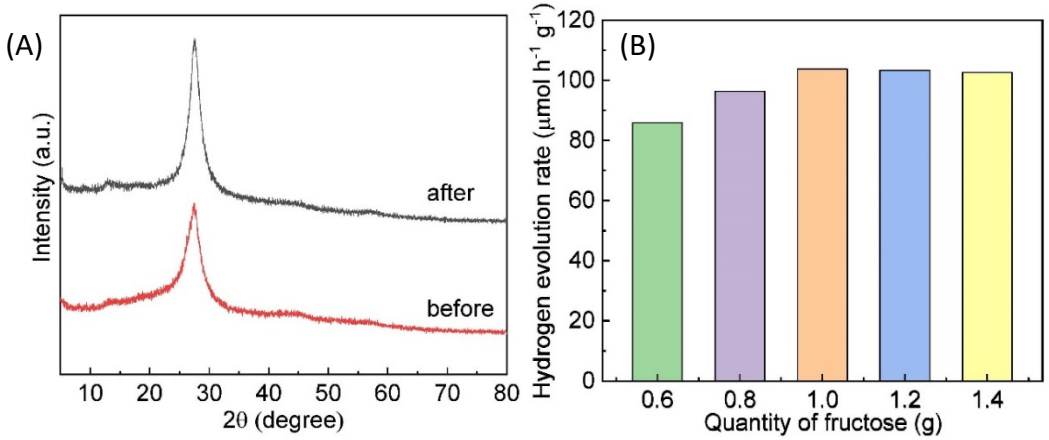

Figure 3-15 (A) XRD spectra of f-CNNP sample before and after photocatalytic H_2 evolution. (B) Hydrogen evolution rate for f-CNNP prepared with different fructose ratios

Figure 3-16A illustrated the photoactivities of the samples for RhB degradation under visible light irradiation ($\lambda > 400$ nm). The f-CNNP and s-CNNP exhibited similar

degradation efficiency but superior than that of GCN. f-CNNP could degrade around 98% of RhB after 120 min irradiation, while about 17% of RhB was removed for GCN under the same conditions. The stability test of RhB degradation for f-CNNP after four cycles confirmed its the good photocatalytic stability (Figure 3-17). Figure 3-16B illustrated the curves for the calculated the apparent reaction constants (*k*), which was obtained by fitting the experimental data with the pseudo-first-order correlation. Accordingly, f-CNNP exhibited the largest *k* value of 0.0182 min^{-1} for the RhB degradation. The *k* value of s-CNNP was 0.0171 min^{-1}, exceeding that of the GCN (0.00113 min^{-1}) around 16-fold.

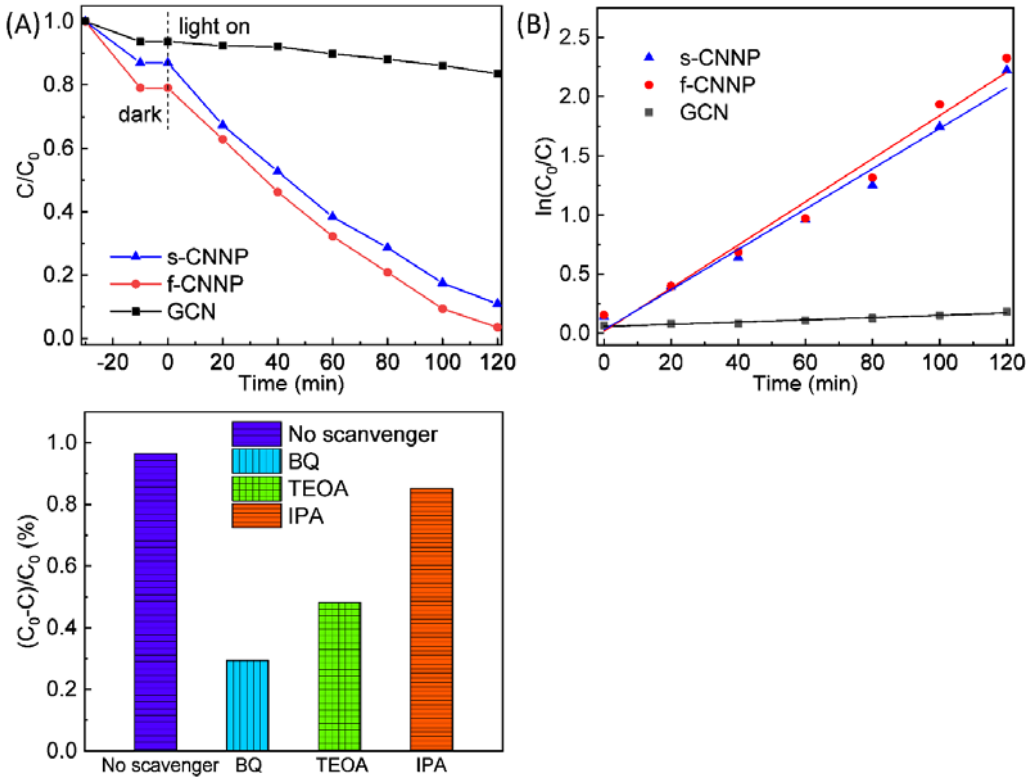

Figure 3-16 (A) Photocatalytic oxidation of RhB for GCN, f-CNNP and s-CNNP and (B) the corresponding apparent reaction constants (*k*) calculation plots under the visible light irradiation. (C) The effect of reactive species on the photocatalytic degradation of RhB solution by f-CNNP.

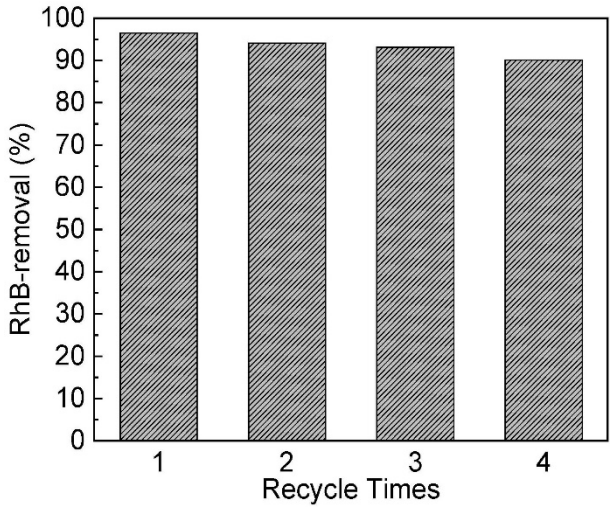

Figure 3-17 RhB photodegradation cycle runs of the f-CNNP

The photocatalytic mechanism was explored by performing the active species trapping experiments for the RhB degradation over the photocatalysts [62,63]. Figure 3-16C illustrated the degradation efficiency is inhibited with the rate decrease of BQ >TEOA > IPA after introducing the scavengers, implying that $\bullet O_2^-$ makes the major contributions to the photodegradation and •OH makes little contribution to enhancing the degradation. As illustrated in Figure 3-18, the e^-/h^+ pairs are formed in CB and VB after the excitation of the photocatalyst by the visible light illumination. Afterwards, the electrons can react with the dissolved O_2 to generate $\bullet O_2^-$ ($E^0(O_2/\bullet O_2^-)$ =−0.33 V vs NHE) [64], combine the produced $\bullet O_2^-$ and H^+ to produce H_2O_2 ($E^0(O_2/H_2O_2)$ = +0.695 eV vs NHE), or react with the generated H_2O_2 to create •OH radicals ($O_2 + e^- \rightarrow \bullet O_2^-$, $\bullet O_2^- + e^- + 2H^+ \rightarrow H_2O_2$, $H_2O_2 + e^- \rightarrow \bullet OH + OH^-$). However, •OH radicals can't be generated effectively in the holes by oxidizing OH^- ($E^0(OH^-/\bullet OH)$ =+1.90 eV vs NHE) [64]. The holes afford to directly oxidize the RhB molecules. For the hydrogen evolution, the sacrificial reagents (TEOA) were firstly subjected to oxidation by holes. The generated electrons then transferred to the cocatalyst Pt on the surface and react with water to evolve H_2. Obviously,

the 2D ultrathin structure play an important part in the photoactivity.

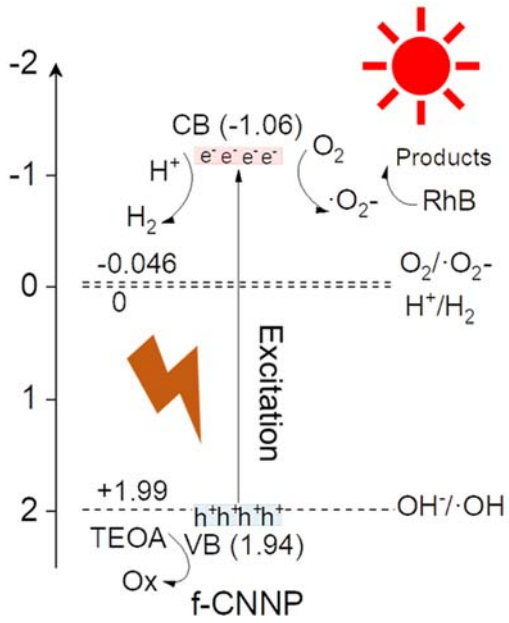

Figure 3-18 The mechanism for photocatalytic activity over f-CNNP photocatalyst.

3.4. Conclusion

In conclusion, a simple, sustainable and efficient method was proposed to prepare the ultrathin g-C_3N_4 nanoplates by the sugar-assisted mechanical milling. The ultrathin g-C_3N_4 nanoplates mainly remained the basic structure and photoelectrical features of the carbon nitride. Furthermore, this ultrathin g-C_3N_4 nanoplates exhibited improved dispersion, enlarged surface area and promoted charge separation and transfer. This ultrathin g-C_3N_4 nanoplates exhibited a superior visible-light-driven photoactivity towards H_2 evolution and RhB degradation than GCN. I envision that this work can inspire the fabrication of ultrathin g-C_3N_4 nanoplates with an enhanced visible-light-driven photoactivity through a sustainable way.

References:

1. X. Wang, K. Maeda, A. Thomas, K. Takanabe, G. Xin, J. M. Carlsson, K. Domen and M. Antonietti, *Nat. Mater.*, 2009, **8**, 76.
2. M. Shekofteh-Gohari, A. Habibi-Yangjeh, M. Abitorabi and A. Rouhi, *Crit. Rev. Environ. Sci. Technol.*, 2018, **48**, 806-857.
3. M. Pirhashemi, A. Habibi-Yangjeh and S. R. Pouran, *J. Ind. Eng. Chem.*, 2018, **62**, 1-25.
4. A. Akhundi, A. Habibi-Yangjeh, M. Abitorabi and S. Rahim Pouran, *Catal. Rev.*, 2019, **61**, 595-628.
5. M. Mousavi, A. Habibi-Yangjeh and S. R. Pouran, *J. Mater. Sci.: Mater. Electron.*, 2018, **29**, 1719-1747.
6. A. Thomas, A. Fischer, F. Goettmann, M. Antonietti, J.-O. Müller, R. Schlögl and J. M. Carlsson, *J. Mater. Chem.*, 2008, **18**, 4893-4908.
7. S. Cao, J. Low, J. Yu and M. Jaroniec, *Adv. Mater.*, 2015, **27**, 2150-2176.
8. W.-J. Ong, L.-L. Tan, Y. H. Ng, S.-T. Yong and S.-P. Chai, *Chem. Rev.*, 2016, **116**, 7159-7329.
9. Q. Liang, Z. Li, Z. H. Huang, F. Kang and Q. H. Yang, *Adv. Funct. Mater.*, 2015, **25**, 6885-6892.
10 J. Zhang, Y. Chen and X. Wang, *Energy Environ. Sci.*, 2015, **8**, 3092-3108.
11. Y. Hong, C. Li, D. Li, Z. Fang, B. Luo, X. Yan, H. Shen, B. Mao and W. Shi, *Nanoscale*, 2017, **9**, 14103-14110.
12. S. Patnaik, S. Martha, S. Acharya and K. Parida, *Inorg. Chem. Front.*, 2016, **3**, 336-

347.

13. C. Chang, L. Zhu, S. Wang, X. Chu and L. Yue, *ACS Appl. Mater. Interfaces*, 2014, **6**, 5083-5093.
14. Z. Lin and X. Wang, *Angew. Chem.*, 2013, **125**, 1779-1782.
15. P. Niu, L. C. Yin, Y. Q. Yang, G. Liu and H. M. Cheng, *Adv. Mater.*, 2014, **26**, 8046-8052.
16. Q. Liang, Z. Li, X. Yu, Z. H. Huang, F. Kang and Q. H. Yang, *Adv. Mater.*, 2015, **27**, 4634-4639.
17. J. Liu, J. Huang, H. Zhou and M. Antonietti, *ACS Appl. Mater. Interfaces*, 2014, **6**, 8434-8440.
18. S. Nayak, L. Mohapatra and K. Parida, *J. Mater. Chem. A*, 2015, **3**, 18622-18635.
19. A. Habibi-Yangjeh and M. Mousavi, *Adv. Powder Technol.*, 2018, **29**, 1379-1392.
20. M. Mousavi and A. Habibi-Yangjeh, *Adv. Powder Technol.*, 2018, **29**, 94-105.
21. S. Asadzadeh-Khaneghah, A. Habibi-Yangjeh and D. Seifzadeh, *J. Taiwan Inst. Chem. Eng.*, 2018, **87**, 98-111.
22. A. Habibi-Yangjeh, M. Mousavi and K. Nakata, *J. Photochem. Photobiol. A: Chem.*, 2019, **368**, 120-136.
23. S. Yang, Y. Gong, J. Zhang, L. Zhan, L. Ma, Z. Fang, R. Vajtai, X. Wang and P. M. Ajayan, *Adv. Mater.*, 2013, **25**, 2452-2456.
24. X. She, H. Xu, Y. Xu, J. Yan, J. Xia, L. Xu, Y. Song, Y. Jiang, Q. Zhang and H. Li, *J. Mater. Chem. A*, 2014, **2**, 2563-2570.
25. W. Liu, N. Iwasa, S. Fujita, H. Koizumi, M. Yamaguchi and T. Shimada, *Appl. Surf.*

Sci., 2020, **499**, 143901.

26. Q. Lin, L. Li, S. Liang, M. Liu, J. Bi and L. Wu, *Appl. Catal. B: Environ.*, 2015, **163**, 135-142.
27. J. Xu, L. Zhang, R. Shi and Y. Zhu, *J. Mater. Chem. A*, 2013, **1**, 14766-14772.
28. P. Niu, L. Zhang, G. Liu and H. M. Cheng, *Adv. Funct. Mater.*, 2012, **22**, 4763-4770.
29. H. Xu, J. Yan, X. She, L. Xu, J. Xia, Y. Xu, Y. Song, L. Huang and H. Li, *Nanoscale*, 2014, **6**, 1406-1415.
30. M. J. Bojdys, N. Severin, J. P. Rabe, A. I. Cooper, A. Thomas and M. Antonietti, *Macromol. Rapid Commun.*, 2013, **34**, 850-854.
31. T. Sano, S. Tsutsui, K. Koike, T. Hirakawa, Y. Teramoto, N. Negishi and K. Takeuchi, *J. Mater. Chem. A*, 2013, **1**, 6489-6496.
32. F. Zhao, H. Cheng, Y. Hu, L. Song, Z. Zhang, L. Jiang and L. Qu, *Sci. rep.*, 2014, **4**, 5882.
33. X. Du, G. Zou, Z. Wang and X. Wang, *Nanoscale*, 2015, **7**, 8701-8706.
34. X. Zhang, X. Xie, H. Wang, J. Zhang, B. Pan and Y. Xie, *J. Am. Chem. Soc.*, 2012, **135**, 18-21.
35. S. P. Pattnaik, A. Behera, R. Acharya and K. Parida, *J. Environ. Chem. Eng.*, 2019, **7**, 103456.
36. S. P. Pattnaik, A. Behera, S. Martha, R. Acharya and K. Parida, J. Mater. Sci., 2019, **54**, 5726-5742.
37. J. S. Kim, J. W. Oh and S. I. Woo, *Int. J. Hydrogen Energy*, 2017, **42**, 5485-5495.
38. Q. Han, C. Hu, F. Zhao, Z. Zhang, N. Chen and L. Qu, *J. Mater. Chem. A*, 2015, **3**,

4612-4619.

39. J. Ji, J. Wen, Y. Shen, Y. Lv, Y. Chen, S. Liu, H. Ma and Y. Zhang, *J. Am. Chem. Soc.*, 2017, **139**, 11698-11701.

40. V. J. González, A. M. Rodríguez, V. León, J. Frontiñán-Rubio, J. L. G. Fierro, M. Durán-Prado, A. B. Muñoz-García, M. Pavone and E. Vázquez, *Green Chem.*, 2018, **20**, 3581-3592.

41. A. Pentecost, S. Gour, V. Mochalin, I. Knoke and Y. Gogotsi, *ACS Appl. Mater. Interfaces*, 2010, **2**, 3289-3294.

42. L. Ge, F. Zuo, J. Liu, Q. Ma, C. Wang, D. Sun, L. Bartels and P. Feng, *J Phys. Chem. C*, 2012, **116**, 13708-13714.

43. Y. Wang, J. Hong, W. Zhang and R. Xu, *Catal. Sci. Technol.*, 2013, **3**, 1703-1711.

44. A. B. Jorge, D. J. Martin, M. T. Dhanoa, A. S. Rahman, N. Makwana, J. Tang, A. Sella, F. Corà, S. Firth and J. A. Darr, *J. Phys. Chem. C*, 2013, **117**, 7178-7185.

45. B. Long, J. Lin and X. Wang, *J. Mater. Chem. A*, 2014, **2**, 2942-2951.

46. F. Dong, L. Wu, Y. Sun, M. Fu, Z. Wu and S. Lee, *J. Mater. Chem.*, 2011, **21**, 15171-15174.

47. F. Dong, Y. Sun, L. Wu, M. Fu and Z. Wu, *Catal. Sci. Technol.*, 2012, **2**, 1332-1335.

48. F. Dong, Z. Wang, Y. Sun, W.-K. Ho and H. Zhang, *J. Colloid Interface Sci.*, 2013, **401**, 70-79.

49. S. Chen, R. Xu, J. Liu, X. Zou, L. Qiu, F. Kang, B. Liu and H. M. Cheng, *Adv. Mater.*, 2019, **31**, 1804810.

50. G. Zhang, M. Zhang, X. Ye, X. Qiu, S. Lin and X. Wang, *Adv. Mater.*, 2014, **26**, 805-

809.

51. D. J. Martin, K. Qiu, S. A. Shevlin, A. D. Handoko, X. Chen, Z. Guo and J. Tang, *Angew. Chem. Int. Ed.*, 2014, **53**, 9240-9245.

52. T. Y. Ma, Y. Tang, S. Dai and S. Z. Qiao, *Small*, 2014, **10**, 2382-2389.

53. J. Yuan, J. Wen, Y. Zhong, X. Li, Y. Fang, S. Zhang and W. Liu, *J. Mater. Chem. A*, 2015, **3**, 18244-18255.

54. M. Kruk and M. Jaroniec, *Chem. Mater.*, 2001, **13**, 3169-3183.

55. Y. Li, R. Jin, Y. Xing, J. Li, S. Song, X. Liu, M. Li and R. Jin, *Adv. Energy Mater.*, 2016, **6**, 1601273.

56. P. Yang, H. Ou, Y. Fang and X. Wang, *Angew. Chem. Int. Ed.*, 2017, **56**, 3992-3996.

57. J. Zhang, M. Zhang, R. Q. Sun and X. Wang, *Angew. Chem. Int. Ed.*, 2012, **51**, 10145-10149.

58. J. Fang, H. Fan, M. Li and C. Long, *J. Mater. Chem. A*, 2015, **3**, 13819-13826.

59. W. Iqbal, B. Qiu, J. Lei, L. Wang, J. Zhang and M. Anpo, *Dalton Trans.*, 2017, **46**, 10678-10684.

60. I. Y. Jeon, S. Zhang, L. Zhang, H. J. Choi, J. M. Seo, Z. Xia, L. Dai and J. B. Baek, *Adv. Mater.*, 2013, **25**, 6138-6145.

61. A. Kudo and Y. Miseki, *Chem. Soc. Rev.*, 2009, **38**, 253-278.

62. J. Shu, Z. Wang, G. Xia, Y. Zheng, L. Yang and W. Zhang, *Chem. Eng. J.*, 2014, **252**, 374-381.

63. N. Huang, J. Shu, Z. Wang, M. Chen, C. Ren and W. Zhang, *J. Alloys Compd.*, 2015, **648**, 919-929.

64. J. Wen, J. Xie, X. Chen and X. Li, *Appl. Surf. Sci.*, 2017, **391**, 72-123.

Chapter 4 Post-annealed graphite carbon nitride nanoplates obtained by sugar-assisted exfoliation with improved visible-light photocatalytic performance

4.1 Introduction

Since the graphitic carbon nitride (g-C_3N_4) as a metal-free photocatalyst is firstly applied to photocatalysis in 2009, it has attracted intense concern because of its appealing electronic band gap, inexpensiveness and high physicochemical stability [1,2]. In virtue of these outstanding merits, the g-C_3N_4 has exhibited promising potential in electrocatalysis, carbon dioxides reduction, photocatalysis, smart assemblies and organic synthesis [2-8]. Nevertheless, the bulk g-C_3N_4 suffers from easy charge recombination and small surface area because of its highly aggregated layers, which hinders its application in photocatalysis [9-14]. To date, several tactics have been applied to enhance the photoactivity of g-C_3N_4, including exotic atoms doping, nanostructure design, organic dyes sensitization, and surface heterojunctions creation [15-29]. Among these modification methods, it is highly challenging but constructive to design and prepare novel nanostructure of g-C_3N_4.

Recently, the two-dimensional (2D) g-C_3N_4 nanoplates has emerged as promising candidate in photocatalysts owing to their abundant active sites, large surface area, and small charge diffusion length. Generally, 2D g-C_3N_4 nanoplates can be fabricated through various methods, including mechanical exfoliation, ultrasonic exfoliation, chemical exfoliation and thermal etching exfoliation [18,30-32]. However, the electronic bandgap

of 2D g-C_3N_4 nanoplates is unavoidably expanded as a result of the strong quantum confinement effect, thus limiting their practical application. Therefore, enhancing its optical harvesting with the 2D structure maintained is highly recommended. Until now, the electronic band gap can be engineered through atomic doping (O, P, S, I, etc), introduction of nitrogen vacancies and cyano groups [33-38]. For example, Niu et al. explored the different effects of N defects on the optical absorption, which turned out to give rise to narrowed band gaps in favor of the photoactivity [39]. Currently, nitrogen defective g-C_3N_4 can be fabricated by various tactics including polymerization, hydrogen reduction, and hydrothermal method [37,40,41]. However, these approaches inevitably generate byproducts with safety issues or/and require tedious procedures, which limited their further applications. Therefore, the development of a sustainable and effective method to create N defects in the g-C_3N_4 nanoplates is highly desirable. Furthermore, the construction of the porous structure on the surface of g-C_3N_4 is also favorable for the photocatalysis because of the enhanced optical absorption by inner reflections together with the enlarged surface area and the decrescent charge transfer length [42,43]. So far, the porous g-C_3N_4 can be synthesized through several methods including thermal reaction in NH_3, lyophilization assisted treatment, template synthesis, and acid treatment [9,44-46].

In this work, a facile strategy was proposed to synthesis porous ultrathin g-C_3N_4 with N defects through mechanical exfoliation followed by rapid thermal treatment. The porous g-C_3N_4 nanoplates was obtained through a glucose-assisted grinding exfoliation followed by the quick thermal heating at 700 ^oC for 2 minutes. This two-step process

exhibited the advantages of a low price, environment benignness and easy handling. As a consequence, the porous g-C_3N_4 nanoplates with repolymerized heptazine units exhibited remarkably improved visible-light photoactivities towards hydrogen (H_2) generation and rhodamine B (RhB) degradation.

4.2. Experimental details

4.2.1. Sample preparation

The pristine g-C_3N_4 was obtained by the pyrolysis of dicyandiamide at 550 ^oC for 4 h under the heating rate of 2.3 °C/min. The yellow aggregates were ground after cooled naturally and labelled as GCN.

To synthesize the ultrathin g-C_3N_4 nanoplates, GCN was mixed with glucose with the mass ration of 1:5 and ground for 2.5 h with a mortar and pestle at rate of 150 rpm. The ground mixture was then put into 40ml of water and sonicated for 1h. After centrifugated at 3000 rpm for 10 minutes, the resultant powder was filtered followed by washing with 200 ml deionized water. The resulting sample was dried in a freeze-dryer and denoted as m-CNNP.

The porous g-C_3N_4 nanoplates was synthesized by a quick annealing of the as-obtained m-CNNP. In detail, m-CNNP in a crucible was transferred to a furnace preheated at 700 ^oC and held at 700 ^oC for 2 minutes in air. The final product after cooling naturally was named as m-CNNP700 with the whole yield of 20%.

4.2.2. Characterization

Crystal structures were obtained by XRD on a Rigaku Miniflex diffractometer. XPS

was carried out using a JEOL JPS-9200. FTIR spectra were recorded by using a JASCO FT/IR-4600 spectrometer. Solid-state ^{1}H and ^{13}C cross-polarisation magic angle spinning nuclear magnetic resonance (CP-MAS-NMR) spectra were recorded on an Avance III HD NMR spectrometer. SEM images were taken with a JEOL JSV-6510LA. TEM was conducted on FEI Titan3 G2 60-300. The PL emission spectra were collected using a JASCO FP-8000 fluorescence spectrophotometer. N_2 adsorption was measured on a Quantachrome Autosorb-iQ2. UV–vis DRS were collected on a JASCO V-750 UV-visible spectrometer. EIS results were collected on a 1260/1287, Solartron Analytical electrochemical workstation. The Mott-Schottky plots were carried out in 0.5 M Na_2SO_4 solution at the frequency of 1000 Hz. The transient photocurrent of the catalysts deposited on an ITO slice were peromed in a three-electrode cell with an aqueous electrolyte of a 0.5 M Na_2SO_4 solution vs Ag/AgCl.

4.2.3. Photocatalytic Hydrogen Generation Test

The photocatalytic H_2 production reactions were conducted in a closed glass reactor. 30 mg samples were suspended in 28 ml of an aqueous solution containing TEOA (10 vol%) as sacrificial agent the and 3 wt% Pt as cocatalyst which was loaded through *in situ* photodeposition using $H_2PtCl_6 \cdot 6H_2O$. Before the reaction, air was removed by introducing nitrogen into the reactor for 30 min. The photocatalytic reaction is triggered by a 150-W Xe lamp with a 400-nm cutoff filter. A gas chromatograph within a thermal conductivity detector (TCD) was used to analyze the generated H_2. The apparent quantum efficiency (AQE) during the irradiation of monochromatic light (425, 475, 500, 550 and 600 nm) was measured using five different band-pass filters as the light source. The AQE

was calculated as follows:

$$\text{QE (\%)} = \frac{\text{number of reacted electrons}}{\text{number of incident photons}} \times 100$$
$$= \frac{\text{number of evolved } H_2 \text{ molecules} \times 2}{\text{number of incident photons}} \times 100$$

4.2.4. Photocatalytic RhB Degradation Test

The photoactivity was further evaluated by Rhodamine B (RhB) degradation. A 25mg of samples was added into 50 mL RhB solution (10 mg/L). Prior to photoreaction, the suspension was sonicated for 15 min and stirred for 15 min in the dark to reach the adsorption equilibrium. 3 mL of the solution was sampled every 20-minute and then centrifuged to remove the photocatalysts. The concentration of RhB was identified by detecting the variations of the absorbance at 554 nm.

4.3. Results and discussion

Figure 4-1 illustrated the preparation of m-CNNP700 through the rapid thermal treatment of the g-C_3N_4 nanoplates obtained by mechanochemistry exfoliation approach. First, the pristine g-C_3N_4 was peeled off through the glucose-assisted co-grinding method followed by sonication and gave rise to the breaking and delamination of the pristine GCN aggregations into size-reduced ultrathin m-CNNP as confirmed by SEM (Figure 4-2A) and TEM images (Figure 4-2C). Then porous m-CNNP700 can be achieved after the quick thermal annealing of m-CNNP, which brought about fragments repolymerization and the porosity creation on the surface (Figure 4-2B). Figure 4-2D illustrated that m-CNNP700 owned a porous few-layered architecture with pores of 50–200 nm on the surface. The SAED pattern of m-CNNP700 with two obvious diffraction rings,

corresponding to the (100) and (002) planes, indicated its highly crystallized nature. As displayed in Figure 4-3, the thickness of m-CNNP700 was estimated to be about ~5 nm versus that of ~3nm for m-CNNP (Figure 4-4). The porous few-layered network of m-CNNP700 afforded to create more active sites for accommodating more reactant molecules and gave rise to a more rapid charge diffusion to the surface for a better photoreaction.

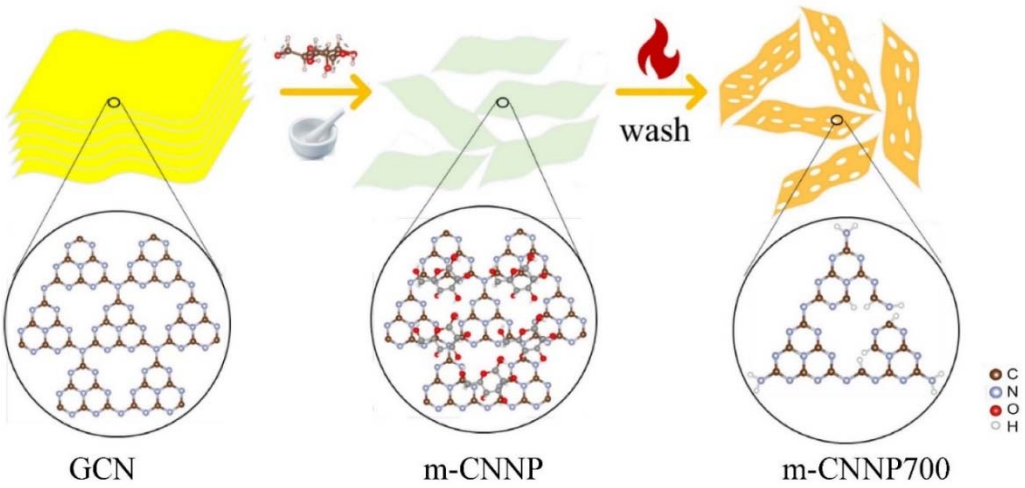

Figure 4-1 Illustration of the exfoliation procedure

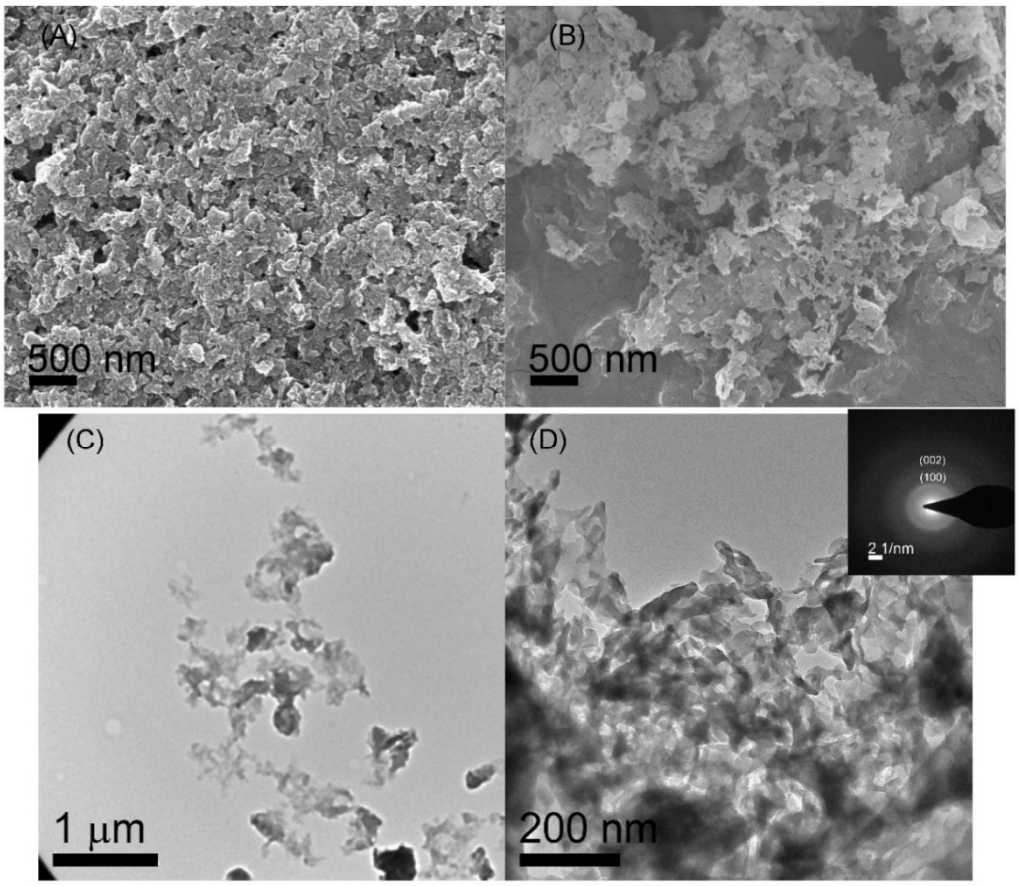

Figure 4-2 Typical SEM of the as-synthesized (A) m-CNNP and (B) m-CNNP700. TEM images of as-synthesized (C) m-CNNP and (D) m-CNNP700. Inset shows the SEAD pattern of m-CNNP700.

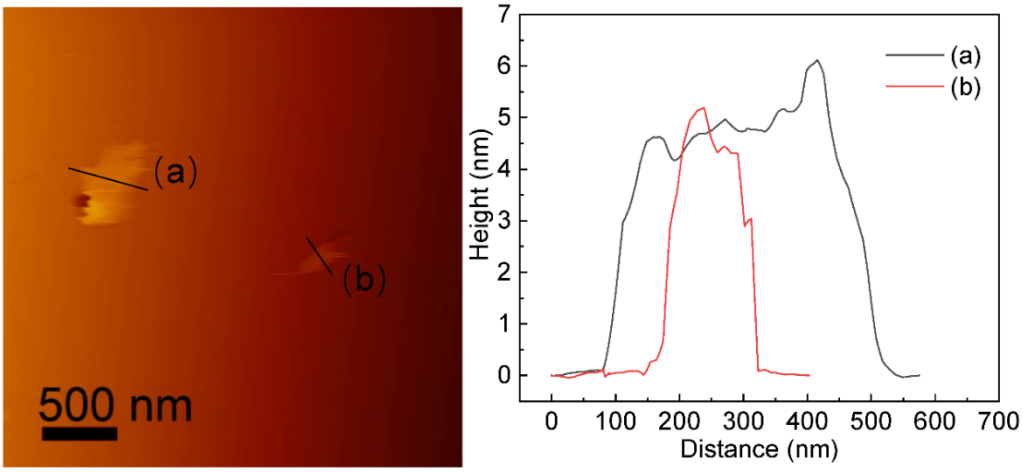

Figure 4-3 (A) AFM image of m-CNNP700 on the Si substrate (B) Height profile along the line in (A)

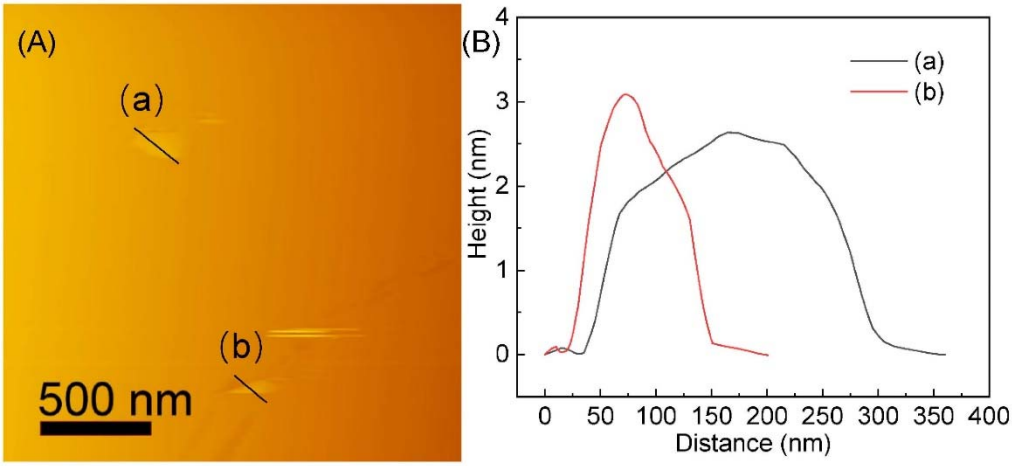

Figure 4-4 (A) AFM image of m-CNNP on the Si substrate (B) Height profile along the line in (A)

Figure 4-5A displayed the XRD spectra of the samples. For the bulk GCN, two typical diffraction peaks could be observed at 13.1° (100) and 27.4° (002), which are indications of the in-planar structural packing and interlayer-stacking of the heptazine motif, respectively [2]. The XRD patterns of m-CNNP and m-CNNP700 exhibited resemblance to that of GCN, indicating their basically maintained crystal structures. With respect to GCN, the decreased intensity peaks of m-CNNP were caused by the efficient exfoliation and decreased particle size [47]. While the slightly increased intensity of m-CNNP700 in comparison with m-CNNP reflected its enhanced conjugated aromatic system due to the quick annealing treatment. Figure 4-5B illustrated the FT-IR spectra of the samples. For all the samples, one can observe the existence of the typical breathing modes of the CN motif at 810 cm^{-1}, the stretching modes of the heptazine rings between 1200 and 1700 cm^{-1} and the O-H or N-H groups between 3000 and 3700 cm^{-1} [48]. The similar diffraction peaks reflected that the hexagonal framework of the three samples are mostly unchanged in accordance with the XRD results. Moreover, an extra absorption band at 2178 cm^{-1} for the m-CNNP700, arising from the stretching vibration

of the cyano groups, probably resulted from destroying the in-plane C-N bonds [38]. In addition, the reduced intensity of the N–H peak for m-CNNP700 between 3000 and 3300 cm^{-1} can be found in other publications [38,48].

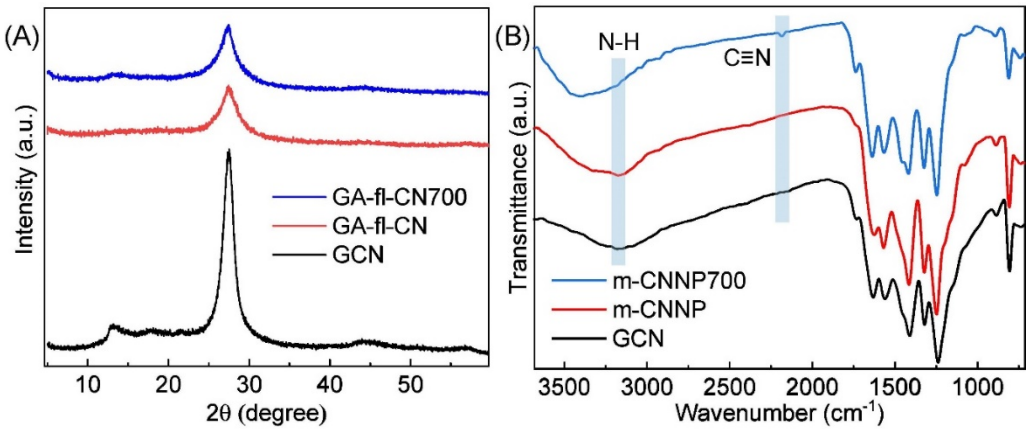

Figure 4-5 (A) XRD patterns and (B) FT-IR of the as-prepared GCN, m-CNNP and m-CNNP700

Figure 4-6 illustrated the XPS spectra of the samples to which were used to explore their surface chemical states. The high-resolution C1s spectrum in Figure 4-6A confirmed the presence of three different peaks at 285.1, 288.2 eV, and 286.2 eV, assigned to the graphitic C=C, $N=C(-N)_2$, and the $C-NH_2$, respectively [38,39]. In comparison, the bonding energies for m-CNNP700 exhibited a small shift due to the electron redistribution. The high-resolution N1s spectrum in Figure 4-6B can be separated into four peaks at 398.4, 399.4, 400.7 eV and 404.2 eV, originating from the sp^2 C–N=C, $N–(C)_3$, N-H groups and the charging effects (π excitation), respectively [38,49]. The peak area percentage of the C–N=C to $N–(C)_3$ for m-CNNP increased from 3.18 (GCN) to 3.75 (m-CNNP), possibly owing to the destroy of the sp^3 $N–(C)_3$ bonds during the grinding treatment (Table 4-1) [50]. Comparatively, the peak area ratio of C–N=C to $N–(C)_3$ for m-CNNP700 exhibited reduction from 3.75 (m-CNNP) to 2.86 (m-CNNP700), indicating

the increased two-coordinated N vacancies in m-CNNP700 [39]. EA also identified the presence of N vacancy and the C/N atomic percentage for m-CNNP700 increase to 0.685 from 0.684 for m-CNNP (Table 4-2). As displayed in the high-resolution O1s spectra (Figure 4-7), two main peaks at 533.6 eV and 531.9 eV are observed for the samples, ascribed to the surface adsorbed O_2 and the C–O species, respectively [40]. With respect to the bulk g-C_3N_4, m-CNNP700 showed slightly increased intensity of the C–O peak, which is probably originates from the thermal oxidation in air. The introduction of O atoms in the framework of g-C_3N_4 is beneficial to the extension of light absorption range and the suppression of the charge recombination, thus in favor of the enhancement of photoactivity [51].

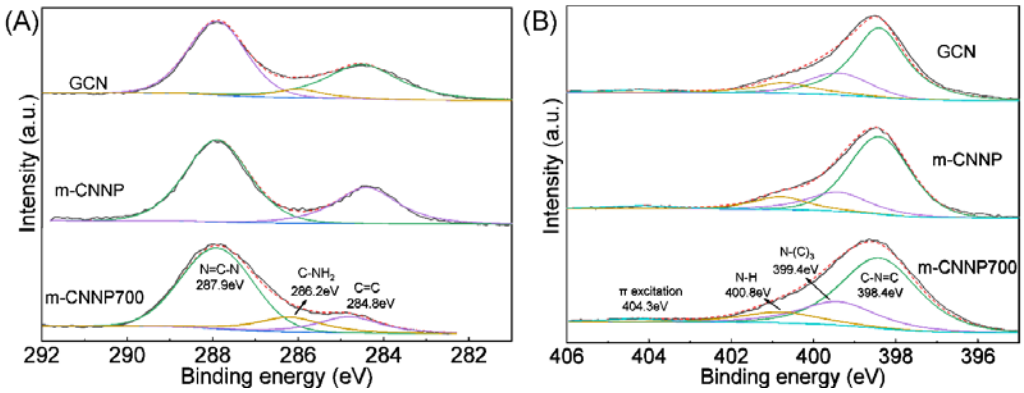

Figure 4-6 High-resolution (A) C1s and (B) N1s XPS spectra of the as-synthesized GCN, m-CNNP and m-CNNP700

Table 4-1. Binding energies of C 1s, N 1s and O 1s for GCN and m-CNNP and m-CNNP700

Sample		GCN	m-CNNP	m-CNNP700
C 1s	C=C	284.5	284.4	284.8
	C-NH_2	286	-	286.2
	N=C-N	287.9	287.9	287.9
Content percent[a]	C=C/ C-NH_2 / N=C-N	26.9/5.8/67.3	31.6/0/68.4	15.9/13.2/70.9
N 1s	C-N=C	398.4	398.4	398.4
	N-$(C)_3$	399.4	399.4	399.4
	N-H	400.8	400.9	400.8
	π excitation	404.3	404.3	404.3
Content percent[b]	C-N=C/ N-$(C)_3$/ N-H/π excitation	0.668/0.210/0.122	0.702/0.187/0.111	0.661/0.231/0.108
O 1s	C-O	531.9	531.9	531.9
	O_2	533.6	533.6	533.6
Content percent[c]	C-O/O_2	84.6/15.4	71.2/28.8	73.4/26.6

a)(content percent% among C species; b)(content percent% among N species; c)(content percent% among O species.

Table 4-2. Elemental analysis of CN samples

Sample	C (wt%)	N (wt%)	H (wt%)	O (wt%)	C/N (wt%)	C/N(atom%)
GCN	34.24	59.86	1.57	4.33	0.572	0.667
m-CNNP	33.10	56.48	2.27	8.15	0.586	0.684
m-CNNP700	33.66	57.34	1.63	7.37	0.587	0.685

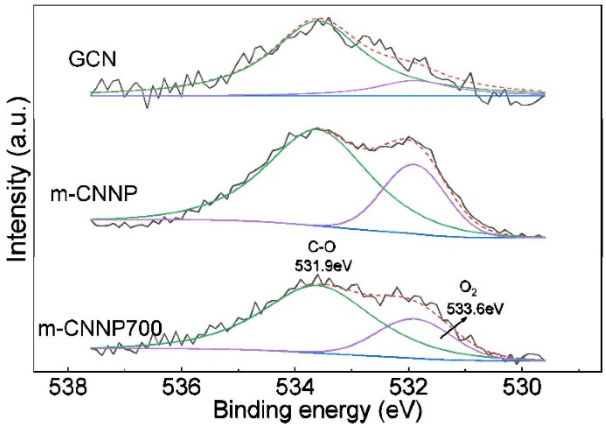

Figure 4-7 High-resolution O1s XPS spectra of the as-synthesized GCN, m-CNNP and m-CNNP700

Figure 4-8 illustrated the solid-state ^{13}C and ^{1}H CP-MAS-NMR of the samples which disclosed their molecular-level structures. The ^{13}C NMR spectra in Figure 4-8A exhibited two major peaks at 156.7 and 164.6 ppm, arising from the N=C–N_2 and N=C–N(NH_x) in the heptazine rings, respectively [52]. The ^{1}H NMR spectra of m-CNNP in Figure 4-8B exhibited two peaks at 0.97 and 4.30 ppm, originating from the C-NH/-NH_2 and HC=N, respectively [53,54]. The presence of C-NH/-NH_2 in m-CNNP reflected its less crystalized property, caused by the destroying the sp^3 N–C bonds during the grinding treatment. While the C-NH/-NH_2 peak disappeared for m-CNNP700, indicating the occurrence of repolymerizing the broken portion upon the quick annealing treatment. Moreover, the content of HC=N for m-CNNP700 increased obviously compared to that of m-CNNP, arising from breaking the in-plane C-N bonds. These results reflected the more disordered structure of m-CNNP700 with increased two-coordinated N vacancies in accordance with the XPS analysis.

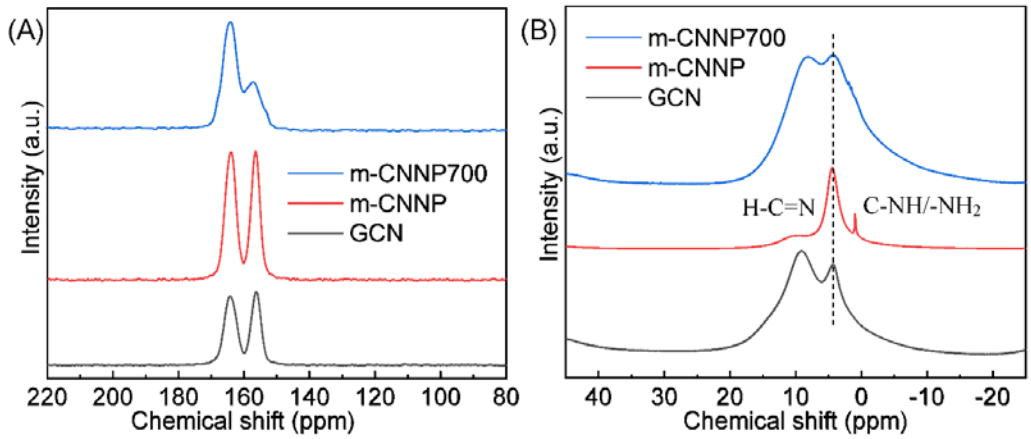

Figure 4-8 Solid-state (A) ^{13}C and (B) ^{1}H cross-polarization nuclear magnetic resonance of GCN, m-CNNP and m-CNNP700

Figure 4-9 illustrated N_2 adsorption–desorption isotherms of the samples which revealed their textural properties. The isotherm of the GCN is identified as a type IV isotherm with largest N_2 adsorption at high pressure regions (P/P_0), implying its mesoporous features [55]. m-CNNP exhibited a much larger surface area (68 $m^2\ g^{-1}$) than the pristine GCN (6.25 $m^2\ g^{-1}$). While the surface area of m-CNNP700 exhibited a small decrease to 59 $m^2\ g^{-1}$ after the annealing treatment, implying its mostly maintained mesoporous structure. For m-CNNP, a wide distribution between 10 and 200 nm can be observed from the pore size distribution curves obtained by the Barrett-Joyner-Halenda (BJH) method. These pores possibly arose from the lamellar structure. Additionally, m-CNNP700 exhibited higher porosity than that of m-CNNP between 70 and 200 nm in accordance with the SEM results. The porous few-layered structure of m-CNNP700 is conductive to the photoreactions, because of its increased accommodating sites and shortened charge diffusion length.

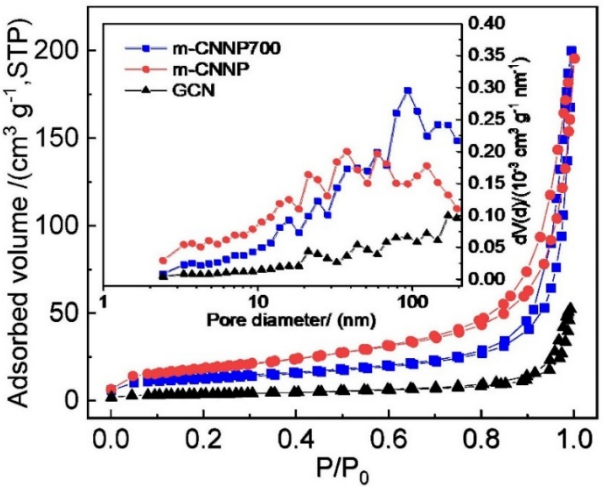

Figure 4-9 N_2 adsorption/desorption isotherms of the as-synthesized GCN, m-CNNP and m-CNNP700. The inset is the corresponding pore size distribution plots

Figure 4-10 illustrated the DRS and PL spectra of the samples which uncovered their optical properties. There appears to be an apparent blue shift of the absorption edge from 450 nm for GCN to 420 nm for m-CNNP (Figure 4-10A). While the fast annealing treatment of the m-CNNP adjusted the optical properties the sample moderately and an obvious red shift in the absorption edge can be observed for m-CNNP700. The bandgap of m-CNNP deduced from the transformed Kubelka–Munk function is widened from 2.77 eV for GCN to 2.97 eV, which arose from the quantum confinement effect [49]. The blue-shifted m-CNNP gives rise to a smaller optical absorbance, which is unfavorable for the photoreactions. In contrast, the bandgap energy of m-CNNP700 is reduced to 2.80 eV, which is caused by the increased cyano groups in its framework [38,39]. Furthermore, its optical absorbance between 450 and 700 nm obviously increased, probably arising from introducing the interband defect states caused by the N vacancy [16]. Therefore, the introduction of N defects (cyano groups and N vacancy) endowed m-CNNP700 with better optical harvesting capability and reduced band energy. Figure 4-10B illustrated the

PL spectra of the samples which reveal their charge separation efficiency. There appears to be a distinct blue shift of the emission PL peak of m-CNNP from 475 nm for GCN to 450 nm in accordance with the absorption spectra. While the emission PL peak of m-CNNP700 exhibited a remarkably decreased intensity with a red shift, implying its significantly suppressed charge recombination. The reduced intensity of the PL peak arose from the electron relocalization on the surface terminal sites in favor of the photoperformance [56].

Figure 4-10C exhibited the photoelectrochemical results of the samples which indirectly reflected their charge separation and migration rate. There appears to be rapid and continuous photocurrent signals during four on–off illumination tests. Upon the illumination, m-CNNP700 exhibits the highest intensity among the three samples, implying its efficient charge separation. Furthermore, Figure 4-10D exhibited the Nyquist plot of the samples. The semicircle diameter of m-CNNP700 is smaller than the other two samples, which indicated its lowest charge transfer resistance and thus fastest charge transfer rate at the solid/liquid interface [57]. The superior charge behavior of m-CNNP700 between the three samples evidenced the important effects of N defects and the porous few-layered structure on its charge separation and transfer.

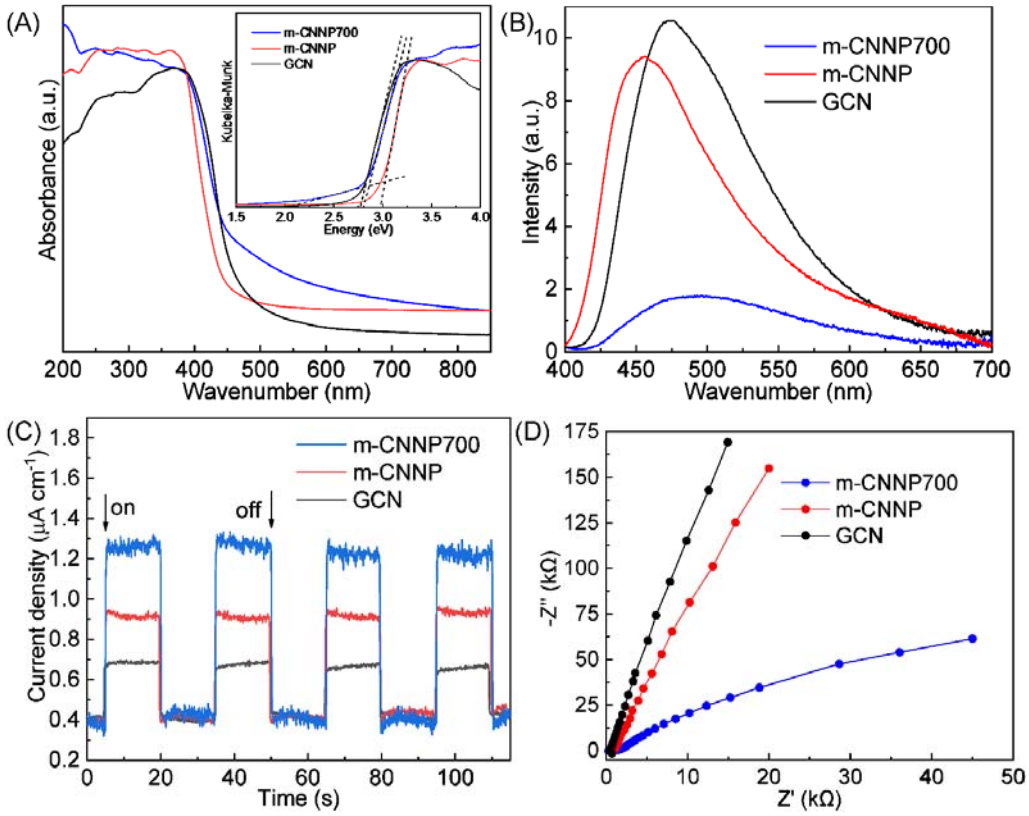

Figure 4-10 (A) UV-vis absorption spectra, (B) PL emission spectra, (C) transient photocurrent spectra and (D) Nyquist plots of EIS of the as-synthesized GCN, m-CNNP and m-CNNP700

Figure 4-11 exhibited the valence band (VB) XPS spectra and Mott–Schottky plots of the samples. All the samples are identified as n-type semiconductors as disclosed by the Mott–Schottky curves in Figure 4-12. The flat-band potentials of the GCN, m-CNNP and m-CNNP700 are -0.75, -0.99 and -0.90 eV (vs. NHE, pH = 7), respectively. The VBM are estimated to be 1.99, 1.99 and 1.90 eV for GCN, m-CNNP and m-CNNP750, respectively (Figure 4-11A). There appears to be a vacancy-related state (−0.11 eV) below the CBM of the m-CNNP700. Because the presence of N vacancies, the extra electrons were subjected to redistribution to their nearest carbon atoms and redelocalization within their π bonds [16,38]. The band structures among the GCN, m-CNNP and m-CNNP700 were

illustrated in Figure 4-11B illustrated on the basis of the above-mentioned analysis.

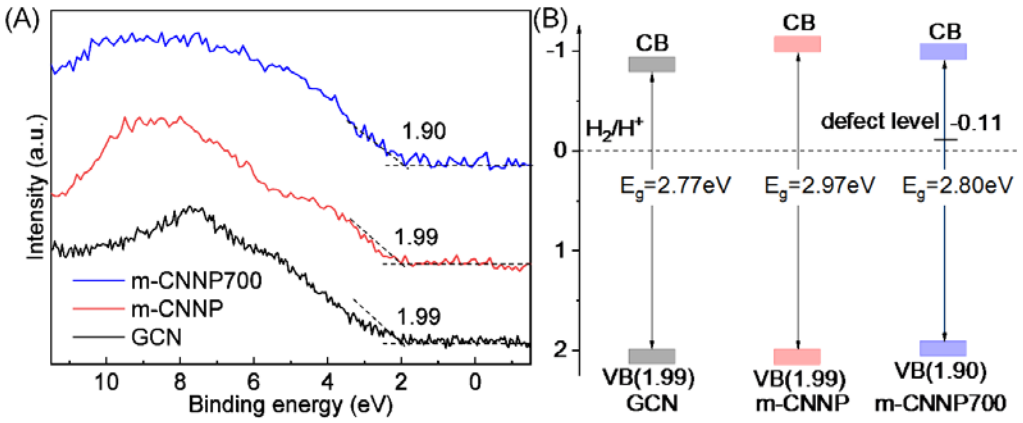

Figure 4-11 (A) XPS valence band spectra and (B) electronic band illustration of the as-fabricated GCN, m-CNNP and m-CNNP700.

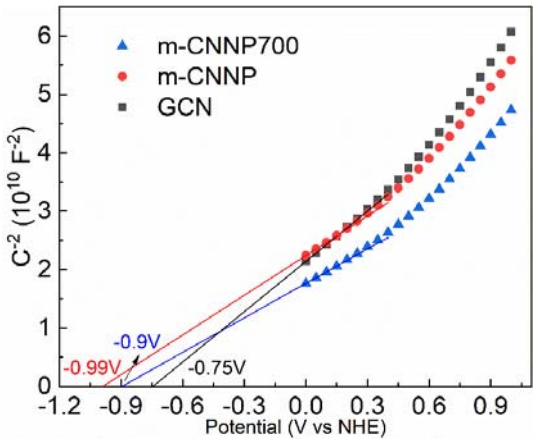

Figure 4-12 Mott-Schottky curves of GCN, m-CNNP and m-CNNP700

The photoperformances of the samples were explored for water splitting by visible-light excitation (>400 nm). Figure 4-13A illustrated the GCN owned the smallest H_2-generation rate of 37.7 μmol h^{-1} g^{-1}, while the H_2-evolution rate of m-CNNP and m-CNNP700 achieved 96.7 and 264.3 μmol h^{-1} g^{-1}. The H_2-generation efficiency of m-CNNP700 exceeded that of the GCN and m-CNNP by about 7-fold and 3-fold, respectively, evidencing the exfoliation and the following post annealing as an impactful tactic to improve the photoactivity. Furthermore, the stability tests of m-CNNP700 in

Figure 4-13B exhibited a persistent H_2 evolution without obvious decrease upon four cycles, confirming its good photostability. Figure 4-13C illustrated the AQE of m-CNNP which were employed to investigate the wavelength dependence of the photoactivity in the visible region. The AQE of m-CNNP700 exhibited a shape similar to the optical absorbance between 400 and 600 nm and the value of AQE at 425 nm reached 1.0%. The results disclosed that the water splitting reaction is driven by photon absorption. The XRD pattern and FTIR spectra further showed that the structure of m-CNNP700 was largely preserved after several reaction cycles (Figure 4-14).

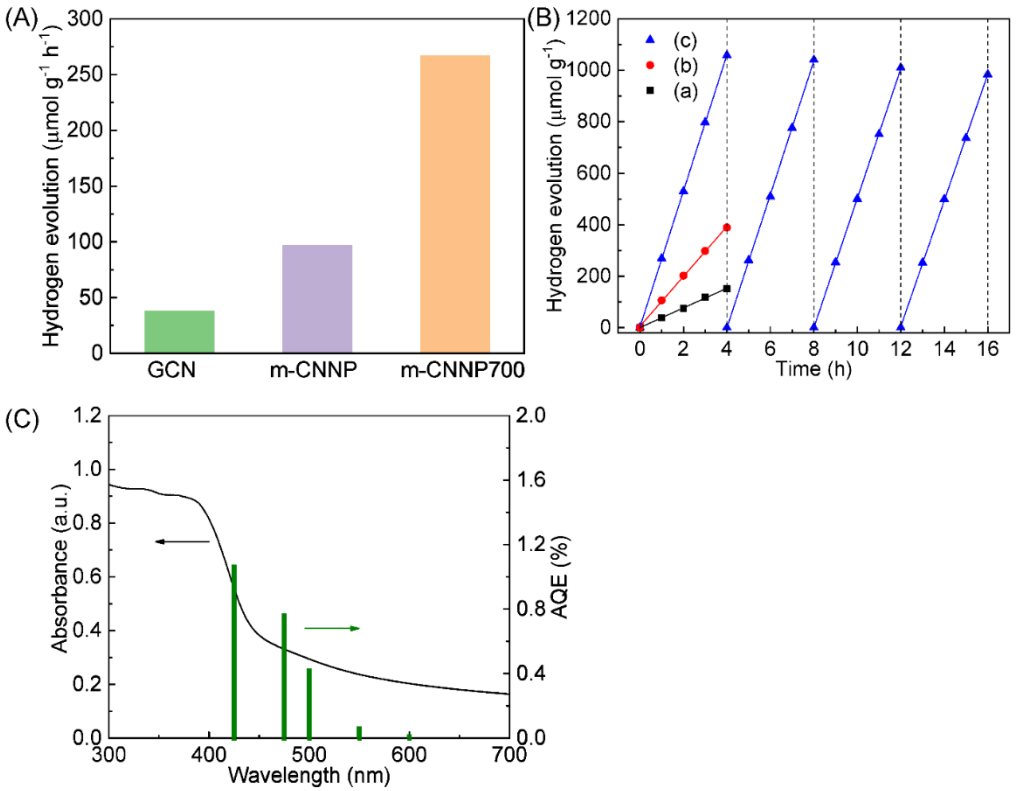

Figure 4-13 (A) Hydrogen evolution rate, (B) test for the stability of hydrogen evolution over the as-fabricated (a) GCN, (b) m-CNNP and (c) m-CNNP700. (C) AQE of m-CNNP700 at 425 nm, 475 nm, 500 nm, 550 nm and 600 nm.

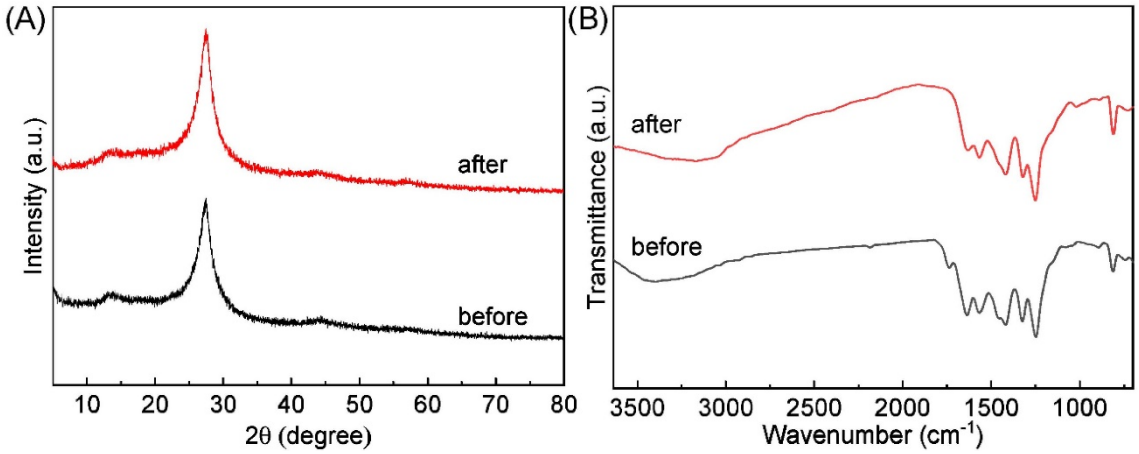

Figure 4-14 (A) XRD patterns and (B) FTIR spectra of m-CNNP700 sample before and after photocatalytic H_2 evolution.

The photoperformance of the samples was further assessed by RhB degradation under visible light excitation (>400 nm). Figure 4-15A exhibited that only 17% of the RhB can be removed by GCN after a 120-minute irradiation. While the few-layered m-CNNP exhibited an impressively increased degradation rate and 92% of the RhB can be degraded under the similar conditions. The porous few-layered m-CNNP700 perserved a good degradation rate and 82% of the RhB was removed. Furthermore, the photocatalytic data was fitted using the pseudo-first-order mode to investigate the photodegradation kinetics. Figure 4-15B exhibited that the m-CNNP700 owned the rate constant of 0.0120 min^{-1}, which exceeded that of GCN (0.0011 min^{-1}) by 11 folds and was of the same order with m-CNNP (0.0185 min^{-1}).

The significantly enhancement in the photoactivities of m-CNNP700 can be explained by several rationales. As illustrated in Figure 4-15C, first, the porous few-layered structure endowed m-CNNP700 an enlarged specific surface area to create more active sites for the H^+/TEOA reactants and accelerated transport of photoinduced charge carriers and H^+/TEOA through the porous architecture. Second, introducing the N defects into m-

CNNP700 brought about the red-shift of the absorbance and thus enhanced photons trapping capacity in favor of the photoactivity according to the DRS results (Figure 4-10A). Moreover, the inner optical reflection in the porous structure of m-CNNP gave rise to an improved optical harvesting capacity, thus beneficial to the photoactivities. Third, the separation of photoinduced charge carriers is accelerated because the defect states served as separation centers to harvest more electrons. Furthermore, a higher degree of crystallinity for m-CNNP700 results in fewer recombination centers and thus facilitated the uphill reactions of water splitting [58]. While the high surface area turns the major factors during the organic degradation because the critical process is the organic adsorption. Therefore, m-CNNP possessed the superior degradation efficiency among the three samples [59,60]. Consequently, because of the tailored crystal, textural, optical and electronic structures, m-CNNP700 exhibited a remarkably improved photoperformance especially towards H_2 production than the bulk GCN and m-CNNP.

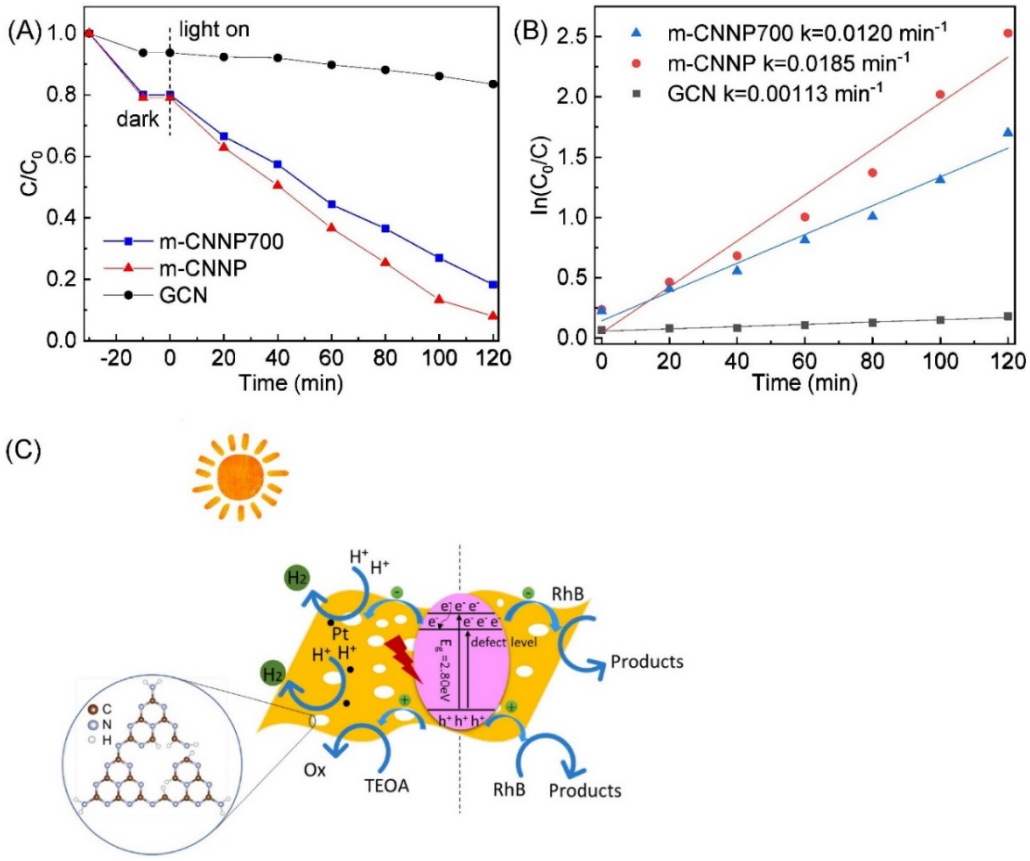

Figure 4-15 (A) Photodegradation of RhB and (B) the relevant kinetic rate constants (K) calculation for GCN, m-CNNP and m-CNNP700. (C) Schematic illustration for the photocatalytic activities by m-CNNP700.

4.4. Conclusion

In conclusion, a facile and scalable method was developed to fabricate the porous few-layered g-C_3N_4 with N defects after the mechanical delamination followed by fast annealing treatment of the pristine GCN. The porous few-layered m-CNNP700 exhibited an enhanced visible-light absorbance, enlarged surface area, shortened charge migration length and accelerated charge mobility. As a consequence, the m-CNNP700 materials exhibited a 7-fold enhancement in the water splitting than the pristine g-C_3N_4 and 3-fold higher than that of m-CNNP under visible light irradiation. Considering the relative

sustainable and scalable fabrication without tedious process, our work is believed to be more promising for efficient solar conversion application.

References:

1. Y. Wang, X. Wang and M. Antonietti, *Angew. Chem. Int. Ed.*, 2012, **51**, 68-89.
2. X. Wang, K. Maeda, A. Thomas, K. Takanabe, G. Xin, J. M. Carlsson, K. Domen and M. Antonietti, *Nat. Mater.*, 2009, **8**, 76.
3. J. Xu, T. J. Brenner, L. Chabanne, D. Neher, M. Antonietti and M. Shalom, *J. Am. Chem. Soc.*, 2014, **136**, 13486-13489.
4. J. Liu, Y. Liu, N. Liu, Y. Han, X. Zhang, H. Huang, Y. Lifshitz, S.-T. Lee, J. Zhong and Z. Kang, *Science*, 2015, **347**, 970-974.
5. Z. Pei, J. Gu, Y. Wang, Z. Tang, Z. Liu, Y. Huang, Y. Huang, J. Zhao, Z. Chen and C. Zhi, *ACS Nano*, 2017, **11**, 6004-6014.
6. Y. Zhang, Z. Zhou, Y. Shen, Q. Zhou, J. Wang, A. Liu, S. Liu and Y. Zhang, *ACS Nano*, 2016, **10**, 9036-9043.
7. X. Zhang, X. Xie, H. Wang, J. Zhang, B. Pan and Y. Xie, *J. Am. Chem. Soc.*, 2012, **135**, 18-21.
8. Q. Wang, W. Wang, J. Lei, N. Xu, F. Gao and H. Ju, *Anal. Chem.*, 2013, **85**, 12182-12188.
9. Q. Liang, Z. Li, Z. H. Huang, F. Kang and Q. H. Yang, *Adv. Funct. Mater.*, 2015, **25**, 6885-6892.
10. J. Zhang, Y. Chen and X. Wang, *Energy Environ. Sci.*, 2015, **8**, 3092-3108.

11. A. Akhundi, A. Habibi-Yangjeh, M. Abitorabi and S. Rahim Pouran, *Catal. Rev.*, 2019, **61**, 595-628.

12. M. Shekofteh-Gohari, A. Habibi-Yangjeh, M. Abitorabi and A. Rouhi, *Crit. Rev. Env. Sci. Tec.*, 2018, **48**, 806-857.

13. M. Pirhashemi, A. Habibi-Yangjeh and S. R. Pouran, *J. Ind. Eng. Chem.*, 2018, **62**, 1-25.

14. M. Mousavi, A. Habibi-Yangjeh and S. R. Pouran, *J. Mater. Sci.: Mater Electron.*, 2018, **29**, 1719-1747.

15. Z. Zhao, G. Ge and D. Zhang, *ChemCatChem*, 2018, **10**, 62-123.

16. J. Ran, T. Y. Ma, G. Gao, X.-W. Du and S. Z. Qiao, *Energy Environ. Sci.*, 2015, **8**, 3708-3717.

17. W. Liu, N. Iwasa, S. Fujita, H. Koizumi, M. Yamaguchi and T. Shimada, *Appl. Surf. Sci.*, 2019, 143901.

18. P. Niu, L. Zhang, G. Liu and H. M. Cheng, *Adv. Funct. Mater.*, 2012, **22**, 4763-4770.

19. D. Chen, K. Wang, W. Hong, R. Zong, W. Yao and Y. Zhu, *Appl. Catal. B: Environ.*, 2015, **166**, 366-373.

20. L. Yao, D. Wei, Y. Ni, D. Yan and C. Hu, *Nano Energy*, 2016, **26**, 248-256.

21. A. Habibi-Yangjeh and M. Mousavi, *Adv. Powder Technol.*, 2018, **29**, 1379-1392.

22. S. Asadzadeh-Khaneghah, A. Habibi-Yangjeh and D. Seifzadeh, *J. Taiwan Inst. Chem. Eng.*, 2018, **87**, 98-111.

23. M. Mousavi and A. Habibi-Yangjeh, *Adv. Powder Technol.*, 2018, **29**, 94-105.

24. E. Vesali-Kermani, A. Habibi-Yangjeh, H. Diarmand-Khalilabad and S. Ghosh, *J.*

Colloid Interface Sci., 2019.

25. A. Habibi-Yangjeh, M. Mousavi and K. Nakata, *J Photochem. Photobiol. A: Chem.*, 2019, **368**, 120-136.
26. E. Liu, J. Chen, Y. Ma, J. Feng, J. Jia, J. Fan and X. Hu, *J. Colloid Interface Sci.*, 2018, **524**, 313-324.
27. Y. Tian, L. Zhou, Q. Zhu, J. Lei, L. Wang, J. Zhang and Y. Liu, *Nanoscale*, 2019, **11**, 20638-20647.
28. H. Dong, M. Xiao, S. Yu, H. Wu, Y. Wang, J. Sun, G. Chen and C. Li, *ACS Catal.*, 2019.
29. Y. Xu, F. Ge, Z. Chen, S. Huang, W. Wei, M. Xie, H. Xu and H. Li, *Appl. Surf. Sci.*, 2019, **469**, 739-746.
30. M. J. Bojdys, N. Severin, J. P. Rabe, A. I. Cooper, A. Thomas and M. Antonietti, *Macromol. Rapid Commun.*, 2013, **34**, 850-854.
31. X. She, H. Xu, Y. Xu, J. Yan, J. Xia, L. Xu, Y. Song, Y. Jiang, Q. Zhang and H. Li, *J. Mater. Chem. A*, 2014, **2**, 2563-2570.
32. Y. Yang, L. Geng, Y. Guo, J. Meng and Y. Guo, *Appl. Surf. Sci.*, 2017, **425**, 535-546.
33. J. Fang, H. Fan, M. Li and C. Long, *J. Mater. Chem. A*, 2015, **3**, 13819-13826.
34. G. Liu, P. Niu, C. Sun, S. C. Smith, Z. Chen, G. Q. Lu and H.-M. Cheng, *J. Am. Chem. Soc.*, 2010, **132**, 11642-11648.
35. Z.-A. Lan, G. Zhang and X. Wang, *Appl. Catal. B: Environ.*, 2016, **192**, 116-125.
36. J. Li, B. Shen, Z. Hong, B. Lin, B. Gao and Y. Chen, *Chem. Commun.*, 2012, **48**, 12017-12019.

37. P. Niu, G. Liu and H.-M. Cheng, *J. Phys. Chem. C*, 2012, **116**, 11013-11018.

38. H. Yu, R. Shi, Y. Zhao, T. Bian, Y. Zhao, C. Zhou, G. I. Waterhouse, L. Z. Wu, C. H. Tung and T. Zhang, *Adv. Mater.*, 2017, **29**, 1605148.

39. P. Niu, M. Qiao, Y. Li, L. Huang and T. Zhai, *Nano Energy*, 2018, **44**, 73-81.

40. Z. Hong, B. Shen, Y. Chen, B. Lin and B. Gao, *J. Mater. Chem. A*, 2013, **1**, 11754-11761.

41. P. Niu, L. C. Yin, Y. Q. Yang, G. Liu and H. M. Cheng, *Adv. Mater.*, 2014, **26**, 8046-8052.

42. J. Fu, B. Zhu, C. Jiang, B. Cheng, W. You and J. Yu, *Small*, 2017, **13**, 1603938.

43. J. Wen, J. Xie, X. Chen and X. Li, *Appl. Surf. Sci.*, 2017, **391**, 72-123.

44. J. Zhang, F. Guo and X. Wang, *Adv. Funct. Mater.*, 2013, **23**, 3008-3014.

45. L. Shi, K. Chang, H. Zhang, X. Hai, L. Yang, T. Wang and J. Ye, *Small*, 2016, **12**, 4431-4439.

46. Q. Han, B. Wang, Y. Zhao, C. Hu and L. Qu, *Angew. Chem.*, 2015, **127**, 11595-11599.

47. Q. Han, C. Hu, F. Zhao, Z. Zhang, N. Chen and L. Qu, *J. Mater. Chem. A*, 2015, **3**, 4612-4619.

48. D. Zhang, Y. Guo and Z. Zhao, *Appl. Catal. B: Environ.*, 2018, **226**, 1-9.

49. S. Yang, Y. Gong, J. Zhang, L. Zhan, L. Ma, Z. Fang, R. Vajtai, X. Wang and P. M. Ajayan, *Adv. Mater.*, 2013, **25**, 2452-2456.

50. Q. Han, F. Zhao, C. Hu, L. Lv, Z. Zhang, N. Chen and L. Qu, *Nano Res.*, 2015, **8**, 1718-1728.

51. L. Yang, J. Huang, L. Shi, L. Cao, Q. Yu, Y. Jie, J. Fei, H. Ouyang and J. Ye, *Appl.*

Catal. B: Environ., 2017, **204**, 335-345.

52. G. Zhang, C. Huang and X. Wang, *Small*, 2015, **11**, 1215-1221.
53. K. Schwinghammer, M. B. Mesch, V. Duppel, C. Ziegler, J. r. Senker and B. V. Lotsch, *J. Am. Chem. Soc.*, 2014, **136**, 1730-1733.
54. D. Zhao, J. Chen, C.-L. Dong, W. Zhou, Y.-C. Huang, S. S. Mao, L. Guo and S. Shen, *J. Catal.*, 2017, **352**, 491-497.
55. J. Yuan, J. Wen, Y. Zhong, X. Li, Y. Fang, S. Zhang and W. Liu, *J. Mater. Chem. A*, 2015, **3**, 18244-18255.
56. B. Long, J. Lin and X. Wang, *J. Mater. Chem. A*, 2014, **2**, 2942-2951.
57. M. Z. Rahman, J. Ran, Y. Tang, M. Jaroniec and S. Z. Qiao, *J. Mater. Chem. A*, 2016, **4**, 2445-2452.
58. G. Liu, G. Zhao, W. Zhou, Y. Liu, H. Pang, H. Zhang, D. Hao, X. Meng, P. Li and T. Kako, *Adv. Funct. Mater.*, 2016, **26**, 6822-6829.
59. A. Kudo and Y. Miseki, *Chem. Soc. Rev.*, 2009, **38**, 253-278.
60. P. Niu, H. Li, Y. Ma and T. Zhai, *J Phys. Chem. C*, 2018, **122**, 20717-20726.

Chapter 5 General Conclusions

In this thesis, the main purpose is to explore the effect of structure modulations of g-C_3N_4 on photocatalysis and to improve the surface area, carrier separation and transfer as well as to facilitate the proton reduction kinetic towards high photocatalytic activity. The detailed results could be concluded in the following parts:

In Chapter 2, few-layered porous g-C_3N_4 (fl-P-CN) has been prepared by a novel combination of thermal etching and gas driven exfoliation of bulk g-C_3N_4. The high temperature treatment has an etching effect on g-C_3N_4, leading to the thermal exfoliation of g-C_3N_4. Later on, after immersing into l-N_2, the g-C_3N_4 is further peeled off with the immediate drastic gasification of l-N_2. As a result, due to the optimized aromatic π-conjugated system, the enlarged surface area, the increased porosity as well as the quantum confinement effect induced by nanoplates, fl-P-CN exhibited impressively improved photocatalytic performance. The findings deepen the understanding on the dimensional-related issues of g-C_3N_4-based materials.

In Chapter 3, using fructose as the assistance, few-layered g-C_3N_4 nanoplates were prepared via sugar-assisted mechanical exfoliation method. The few-layered structure rendered the as-prepared g-C_3N_4 much increased surface area and also accelerated charge separation and transfer efficiency. As a result, such material possessed hydrogen evolution rate of 103.7 μmol/h/g, which was about 3 times higher than that of the bulk g-C_3N_4. These findings emphasized the significance of 2D structure of g-C_3N_4 for the efficient carrier separation and transfer and subsequent photocatalysis, and also suggested

that the modulation of nanostructure in g-C_3N_4-related organic semiconductors in a sustainable way might open new avenues towards improved photocatalysis.

In Chapter 4, I demonstrated that post-annealing treatment of g-C_3N_4 nanoplates could lead to a significant enhancement in photocatalytic H_2 production over the bulk g-C_3N_4 under visible light irradiation. Upon the fast thermal etch on g-C_3N_4 nanoplates, a H_2 evolution rate as high as 264.3 μmol/ h/g was achieved for the N-deficient g-C_3N_4 nanoplates, which was about 7 times higher over that of bulk g-C_3N_4 and 3-fold greater than that of g-C_3N_4 nanoplates by visible light irradiation. It was confirmed that such improvement in activity relied on the tailored crystal, textural, optical and electronic structures. These discoveries would provide a facial approach for the designing of organic semiconductors with porous few-layered structure for efficient photocatalysis.

Acknowledgements

I would like to express my great gratitude to my supervisor, Prof. T. Shimada who deeply influenced me with his profound academic attainments, rigorous scientific attitude and keen insight.

I also extend my deep respect and sincere thanks to Professors H. Habazaki, C. Y. Zhu, M. Higuchi, Y. Masubuchi, K. Tadanaga, A. Miura, C. Rosero-Navaro, Takashi Yanase, Nobuhiro Iwasa, Hitoshi Koizumi, Shin Mukai, Shinichiro Iwamura, Taro Nagahama and Ms. N. Wang for their valuable discussions and experimental facilities.

I would like to thank the members of laboratory of the solid state chemistry for their helps and advice.

I would also like to extend my gratitude to my family for their support and understanding.